ELECTROSORPTION OF IONS FROM AQUEOUS SOLUTIONS BY MESOPOROUS CARBON MATERIALS

A Dissertation
Presented to
The Academic Faculty

by

Ketki Sharma

In Partial Fulfillment
of the Requirements for the Degree
Doctor of Philosophy in the
School of Civil and Environmental Engineering

Georgia Institute of Technology
May 2014

ELECTROSORPTION OF IONS FROM AQUEOUS SOLUTIONS BY MESOPOROUS CARBON MATERIALS

Approved by:

Dr. Sotira Yiacoumi, Advisor
School of Civil and Environmental Engineering
Georgia Institute of Technology

Dr. Costas Tsouris
School of Civil and Environmental Engineering
Georgia Institute of Technology

Dr. Spyros G. Pavlostathis
School of Civil and Environmental Engineering
Georgia Institute of Technology

Dr. Christine Payne
School of Chemistry and Biochemistry
Georgia Institute of Technology

Dr. Ching-Hua Huang
School of Civil and Environmental Engineering
Georgia Institute of Technology

Date Approved: 9 December, 2013

To my beloved family Shashi Bhushan Sharma, Savitri Sharma, Madhumita Sharma, and Manish Sharma

ACKNOWLEDGEMENTS

I would like to express my sincere gratitude to my Ph.D. advisor Dr. Sotira Z. Yiacoumi for her support, encouragement, and advice. I am grateful to her for her guidance, which made the time I spent at Georgia Tech, a valuable learning experience for me. I would also like to thank Dr. Costas Tsouris from Oak Ridge National Laboratory for his valuable advice and ideas on my research. I am truly grateful to have had the opportunity to work with them. I thank Dr. Spyros G. Pavlostathis, Dr. Ching-Hua Huang, and Dr. Christine Payne for their valuable time, suggestions, and feedback on my research. I would also like to thank Dr. Guangxuan Zhu for his assistance with the experimental equipment I used during my Ph.D. work. I am grateful to Oak Ridge National Laboratory (ORNL) for providing me with access to the research facilities and supporting my visit there. I feel fortunate to be given the opportunity to conduct my research at the High Flux Isotope Reactor (HFIR) and Spallation Neutron Source (SNS) facilities at ORNL. I am also thankful to all our collaborators from Oak Ridge National Laboratory, Dr. Hassina Z. Bilheux, Lakeisha M. H. Walker, Dr. Sophie Voisin, Dr. David DePaoli, Dr. Richard Mayes, Dr. Jim Kiggans, and Dr. Sheng Dai for their input and suggestions in my research. I would like to thank Dr. Jorge Gabitto from Prairie View A&M University for his help with the transport modeling which was essential for the completion of my research. I am also grateful to Richard Bedell from the School of Chemistry and Biochemistry at Georgia Tech for his help with the setup for the Blue Energy experiments.

The funding support by the National Science Foundation (Grant No. CBET-0651683), and Campbell Applied Physics, Inc. is greatly acknowledged. A part of this research was conducted at ORNL and supported by the U.S. DOE Office of Energy Efficiency and Renewable Energy (EERE), under Contract DE-AC05-0096OR22725 with ORNL.

I would like to thank my current and previous lab mates, Patricia, Eunhyea, Hyojin, Yong-Ha, and Austin for their friendship and help in my research. I would also like to thank all my friends at Georgia Tech who made my time in Atlanta enjoyable.

I am grateful to my family, their love and support is a constant source of motivation for me. I give my deepest appreciation to my parents and sister for always believing in me and encouraging me in anything I want to accomplish.

TABLE OF CONTENTS

LIST OF TABLES

LIST OF FIGURES

LIST OF SYMBOLS AND ABBREVIATIONS

a_v	Electrode specific surface area (m^2/m^3)
A_{eff}	Porous medium effective area (m^2/m^3)
c^*	Dimensionless ion concentration in the pore space at position x (C/C_∞)
C	Molar concentration of ions at position x (M)
C_∞	Molar concentration of ions in the bulk (M)
D_{eff}	Effective diffusion coefficient (m^2/s)
D	Bulk solution diffusion coefficient (m^2/s)
D^*_{eff}	Dimensionless effective diffusivity given by ratio of effective diffusivity and the bulk solution diffusion coefficient (D_{eff}/D)
D_+	Diffusion coefficient of cation (m^2/s)
D_-	Diffusion coefficient of anion (m^2/s)
e	Elementary charge (1.6×10^{-19} C)
F	Faraday's gas constant
h_p	Pore thickness ($h_p = \varepsilon_\alpha/a_v$) (m)
j^*_{charge}	Rate of charge removal ($mole/m^2s$)
j^*_{salt}	Rate of salt adsorption ($mole/m^2s$)
J^*_{charge}	Dimensionless rate of charge removal
J^*_{salt}	Dimensionless rate of salt adsorption
J_{lim}	Diffusion-limited current ($J_{lim} = 2\ D_{eff}C_\infty/L_{elec}$)
J	Flux of ions
k	Boltzmann constant (1.38×10^{-23} J K^{-1})
L_{elec}	Thickness of electrode (m)

L_{SDL}	Thickness of stagnant diffusion layer (m)
N	Number of ions per unit volume at position x
N_o	Number of ions per unit volume present in the bulk
N_{av}	Avogadro's Number (6.022×10^{-23} mol^{-1})
q^*	Dimensionless surface charge density
R	Universal gas constant
t^*	Dimensionless time
T	Temperature (K)
w^*	Dimensionless excess salt adsorption
x	Dimensionless position
z_+	Valence of cation
z_-	Valence of anion
z	Valence of ion

δ	λ_S/λ_D (ratio of thickness of stern layer to debye screening length)
$\Delta\phi_D$	Potential difference across the diffuse layer
$\Delta\phi_S$	Potential difference across the stern layer
ε	Ratio of Debye length to pore thickness (λ_D / h_p)
ε_α	Electrode porosity
λ_B	Bjerrum length (0.72×10^{-9} m at room temperature)
λ_D	Debye screening length ($\lambda_D = 1/\sqrt{8\pi\lambda_B N_{AV} C_\infty}$)
λ_S	Effective thickness of the stern layer (m)
μ_I	Solution viscosity (kg m^{-1} s^{-1})

τ_d	Dimensional time (s)
ϕ	Dimensionless potential in the solution filling the pore space
ϕ_1	Equivalent solid phase potential
ψ	Dimensional electrical potential (V)

ACS	Activated Carbon Sheet
AC	Alternating Current
BET	Brunauer-Emmett-Teller
BJH	Barrett-Joyner-Halenda
CCD	Charge Coupled Device
CDI	Capacitive Deionization
CDLE	Capacitive Double Layer Expansion
DC	Direct Current
DMF	Dimyethyl Formamide
EDL	Electrical Double Layer
GCS	Gouy Chapman Stern
HFIR	High Flux Isotope Reactor
MC	Mesoporous Carbon
MED	Multi-effect Distillation
MSF	Multi-stage Flash
ORNL	Oak Ridge National Laboratory
PMCG	Phloroglucinol-based Mesoporous Carbon-coated Graphite
PRO	Pressure Retarded Osmosis

PVDF	Polyvinylidene fluoride
RED	Reverse Electrodialysis
RMCG	Resorcinol-based Mesoporous Carbon-coated Graphite
RO	Reverse Osmosis
SDL	Stagnant Diffusion Layer

SUMMARY

Electrosorption involves application of an electrical potential between porous carbon electrodes submerged in saline water, which results in the formation of an electrical double layer at the interface. The electrosorption phenomenon has applications in several environmental processes such as removal of heavy metals from aqueous solutions, sorption in groundwater remediation, and water desalination by capacitive deionization (CDI). Electrosorption also has applications in energy storage by supercapacitors. This research is focused on application of electrosorption in desalination of water by the CDI technology and in extraction of renewable energy based on capacitive double layer expansion. The aim of the study is to understand how the various system and operational parameters such as applied potential, solution temperature, and valence and size of ions influence the electrosorption mechanisms. Porous carbon materials are suitable electrodes for these applications as they have a high surface area and electrical conductivity. In the present study, self-assembled mesoporous carbon electrodes synthesized at the Oak Ridge National Laboratory (ORNL) were characterized to determine their sorption properties. Experimental results from CDI and neutron imaging experiments, and theoretical results from transport modeling have been obtained and compared to draw inferences on the sorption characteristics of mesoporous carbon electrodes.

The influence of temperature on sorption of ions by mesoporous carbon materials has been investigated by laboratory scale CDI experiments. Higher rates of sorption and regeneration were observed with solutions at higher temperature of around 40°C. The

experiments conducted with sodium chloride and Instant Ocean solutions at higher temperature revealed competition behavior between ions of various radii and valence. The cumulative mass of salt taken up by the electrodes was calculated by theoretical modeling and matched with the experimental data to obtain the diffusivity of ions.

In the next part of the thesis, neutron imaging has been applied to observe at a microscopic level, the ion transport phenomena occurring during electrosorption at the electrode-electrolyte interface. Neutron imaging of gadolinium ions was conducted to obtain the concentration profiles of ions across the electrodes as a function of time. Neutron imaging reveals interesting ion transport phenomena during the regeneration step in the CDI process. The information obtained on the ion transport behavior can aid in the optimization of the process. Fick's second law of diffusion was applied to estimate the effective diffusion coefficient of gadolinium ions. The effective diffusivity of gadolinium ions increased by about 7 times on application of 1.2 V (direct current) DC potential as compared to the case when no potential was applied. Information on the values of the effective diffusivity of ions can aid in theoretical modeling of the CDI process as well as guide strategies for design of advanced electrode materials.

In the continuation of the study, neutron imaging was applied to visualize the transport of lithium ions in mesoporous carbon materials. The first set of experiments was conducted at a high concentration of lithium chloride to gain insight into the behavior of capacitive deionization with solutions of high ionic strength. It was found that the electrodes become saturated with salt during the sorption phase which inhibits the regeneration of ions on removal of external potential. It is proposed that by designing a membrane capacitive deionization setup for desalination of solutions of high ionic

strength, the saturation of electrodes can be prevented. Moreover, the effective diffusivity of lithium ions was estimated by employing Fick's second law of diffusion. The study has applications in electrochemical energy storage devices such as lithium ion batteries and the results obtained can be utilized to improve the performance of these systems.

In the next part of the study, the effect of application of high-frequency and low-amplitude alternating current (AC) signal superimposed on the DC potential was studied on the electrosorption process. It was observed that application of AC signal resulted in higher rates of sorption and regeneration in the CDI process. Furthermore, neutron imaging was employed to validate the results obtained with the laboratory-scale CDI experiments. Neutron imaging experiments conducted with gadolinium ions demonstrated enhanced ion transport under the influence of AC potential.

In the final part of the thesis, blue energy experiments were conducted to evaluate the feasibility of energy production based on the capacitive double layer expansion principle. Neutron imaging of the blue energy cycle was conducted to investigate the direction and magnitude of ion transport during the various steps of the blue energy cycle. For experiments conducted at 1.2 V no increase in potential was observed. An increase of 0.061 V and 0.054 V was observed for experiments conducted at 0.6 V and 0.9 V respectively. Moreover from the sequences of neutron images obtained for each step of the blue energy cycle, information on the direction and magnitude of lithium ion transport was obtained.

The results obtained in this thesis provide insights into the fundamental ion transport mechanisms during electrosorption by mesoporous carbon materials. This

research has important implications for developing advanced systems for desalination of saline water and extraction of renewable energy based on salinity gradients.

CHAPTER 1

INTRODUCTION

1.1 Electrosorption of Ions from Aqueous Solutions

A layer of interaction between a solid and liquid electrolyte environment is commonly encountered in colloidal systems. The presence of a charged surface in an electrolyte solution results in the development of a potential gradient across the interface. This phenomenon results in the formation of a region with a high concentration of oppositely charged ions near the charged surface, called the electrical double layer (EDL). The study of EDL formation has significance in many processes such as filtration, coagulation, flocculation, sedimentation, energy storage, and purification of water by electrosorption. The electrosorption phenomenon involves the application of an electrical potential between electrode pairs submerged in brackish water, effectively "trapping" the ions in the EDL at the interface.

Electrosorption has significant applications in environmental engineering such as desalination of water by the capacitive deionization (CDI) technology. Capacitive deionization is an electrochemical method for water desalination based on the electrosorption of ions by electrically conductive electrodes of high surface area. The CDI technology has several advantages over conventional desalination methods including reversibility, operation at low voltages, low energy requirements, and reduction of secondary wastes. The potential for commercial application of CDI as an energy efficient technology for water treatment has been discussed in recent literature (Anderson et al., 2010; Oren, 2008; Porada et al., 2013). Nanostructured, porous carbon materials are

promising electrode materials for CDI application as they have a low electrical resistivity and a high surface area.

Besides water desalination, electrosorption of ions by carbon materials can be utilized in energy applications. Based on the electrical double layer capacitor technology, energy can be extracted by mixing salt water and fresh water. Energy obtained from mixing fluids of different salinities, referred to as the Blue Energy, is a promising renewable energy source (Brogioli, 2009; Norman, 1974; Pattle, 1954). The electrosorption phenomenon also has energy storage applications; an EDL capacitor or a supercapacitor stores energy at the electrode-electrolyte interface. Supercapacitors have good reversibility, a high power density, a low internal resistance, and no chemical reactions are involved (Bispo-Fonseca et al., 1999; Hrubesh, 1998).

The phenomenon of EDL formation plays an important role in determining ion sorption and transport characteristics inside the pores of the carbon electrodes. Various factors such as the concentration and temperature of the electrolyte solution, ion valence, ion radii, and the applied potential affect the electrosorption capacity of the carbon electrodes. The desired electrosorption efficiency can be achieved by manipulation of the EDL formation in the confined space of nanopores. Therefore, an in-depth understanding of how these factors influence the formation of EDL is critical for improving the desalination efficiency in the electrosorption process.

Most of the research conducted in the field of capacitive deionization has been experimental, aimed towards the synthesis of novel electrode materials or modifications to standard electrode materials to obtain enhanced electrosorption capacity. A wide range of carbon materials such as carbon aerogel (Farmer et al., 1997; Farmer et al., 1996;

Gabelich et al., 2002; Jung et al., 2007; Miller and Dunn, 1999; Pekala et al., 1998; Wang et al., 1993; Xu et al., 2008; Ying et al., 2002; Zhang et al., 1999), activated carbon (Oh et al., 2006; Ryoo et al., 2003), mesoporous carbon (Li et al., 2009; Mayes et al., 2010; Zou et al., 2008a), graphene (Li et al., 2010a, b), carbon nanotubes (Chen et al., 2010; Gao et al., 2009; Gao et al., 2007; Pan et al., 2009; Tsouris et al., 2011; Wang et al., 2006; Zhang et al., 2007), carbon fiber webs (Wang et al., 2010a), graphitized carbon material (Hou et al., 2006), and microporous carbon (Porada et al., 2012) have been utilized for application in the electrosorption of ions. Amongst all the forms of carbon investigated for application in CDI, carbon aerogels have been the most popular. Gabelich et al. (2002) investigated the influence of ion size and valence on the sorption of ions by carbon aerogels (Gabelich et al., 2002). Recently, mesoporous carbon materials have attracted interest because the presence of mesopores results in a greater access of ions to the pores. Zou et al. (2008) concluded that the presence of ordered structure in mesoporous carbon and control of micropores leads to a greater electrosorption capacity in mesoporous carbon (Zou et al., 2008a). Li et al. (2009) investigated a sol-gel process to synthesize ordered mesoporous carbon and deduced that mesoporous carbon obtained by addition of $NiSO_4.6H_2O$ exhibited highest electrosorption capacity (Li et al., 2009).

The laboratory-scale cyclic voltammetry and capacitive deionization experiments provide an insight into how the various system parameters influence the electrosorption capacity of the carbon electrodes. Since the experiments are on a macroscopic level, the understanding is limited as we cannot observe the ion transport phenomena behind these observations. Therefore, neutron imaging experiments have been employed to gain an understanding at nanoscale of ion transport phenomena occurring at the electrode-

electrolyte interface. Instead of focusing on the synthesis of novel materials, the aim of the study is to understand how the various system parameters affect the electrosorption capacity in the CDI process. In the current study, self-assembled mesoporous carbon (MC) electrodes synthesized at the Oak Ridge National Laboratory (ORNL) have been characterized to determine their properties, including specific capacitance and sorption characteristics under various operating conditions.

In the present study, a combination of experimental and modeling work is presented to understand how the factors such as properties of electrolyte, ion size, and applied potential influence the electrosorption behavior of mesoporous carbon materials.

1.2 Scope and Objectives

This research combines experimental and modeling studies to investigate the ion transport mechanisms at the interface during electrosorption by carbon electrodes. The research is relevant to the removal of ions by the CDI technology and the extraction of renewable energy from salinity difference.

The specific objectives of the present study are as follows:

1. Evaluate and compare the specific capacitance of carbon aerogels and mesoporous carbon materials through cyclic voltammetry experiments.
2. Investigate the influence of various system parameters such as ionic concentration, ion size and valence, temperature of the solution, and applied potential on the electrosorption characteristics in capacitive deionization experiments.
3. Examine the transport behavior of ions in mesoporous carbon materials by neutron imaging experiments and estimate the transport parameters such as the diffusion coefficient.

4. Assess the ability to extract energy by mixing fluids of different salinities, based on the contraction and expansion of electrical double layers inside the pores of carbon electrodes.

1.3 Organization of Thesis

Chapter 1 discusses the phenomenon of electrosorption, its applications in water purification and energy storage, and the motivation for this research. The scope and major objectives of the present work are discussed in this chapter. A literature review on the application of nanoporous carbon materials for electrosorption is described in Chapter 2. The specific application of the electrosorption phenomenon in water desalination and in extraction of energy from mixing fluids of different salinities has been discussed in detail. Neutron imaging is discussed as a novel technique to study the electrosorption of ions by mesoporous carbon electrodes at a nanoscopic scale.

Chapter 3 describes the influence of temperature on electrosorption of ions from saline solutions via capacitive deionization experiments. Results from transport modeling are also presented to predict the influence of temperature and match the model predictions with experimental data. In Chapter 4, neutron imaging is presented as a tool to investigate the ion transport mechanisms during electrosorption at nanoscale. Neutron imaging of gadolinium ions has been carried out to estimate the effective diffusivity of gadolinium ions under different conditions of applied potential. The Fick's second law of diffusion has been applied to match the modeling results with the experimental concentration profile of gadolinium ions in the carbon electrodes. In Chapter 5, neutron imaging of lithium ions is presented to study the behavior of electrosorption at high

concentrations of electrolyte. In addition, the effective diffusion coefficient of lithium ions is estimated by employing Fick's second law of diffusion.

In Chapter 6, the enhancement of ion electrosorption rates in capacitive deionization experiments is reported by application of low-amplitude high frequency electrical signal. The results are validated by neutron imaging experiments and the image sequences show an enhanced transport of gadolinium ions under the influence of AC voltage. Chapter 7 discusses the application of neutron imaging technique to observe the ion transport behavior during the blue energy recovery cycle. The thesis is completed with the overall findings and conclusions and the recommendations for future work stated in Chapter 8.

CHAPTER 2

BACKGROUND

2.1 Nanoporous Carbon Materials for Electrosorption

To achieve a high sorption capacity in the electrosorption process, electrode materials of high specific surface area, electrical conductivity, and stability are required. Porous, nanostructured carbon materials are suitable electrode materials for electrosorption as they have a high conductivity and high surface area per unit mass. The nanostructured carbon materials can be specified as mesoporous (20 Å < pore diameter < 500 Å) and microporous (< 20 Å) based on pore size. Most of the research done in 1990's on the capacitive deionization technology has focused on carbon aerogel as the electrosorption material (Gabelich et al., 2002; Yang et al., 2001). Carbon aerogel materials have a low electrical resistivity (<40 mΩ) and high surface area (~400 m^2/g) (Pekala et al., 1998; Wang et al., 1993; Zhang et al., 1999). The majority of surface area of this material is in pores of <10 Å, which do not contribute significantly to the electrosorption capacity (Hou et al., 2006). The presence of significant microporosity results in a greater surface area; however, micropores inhibit ion penetration, and the material is more susceptible to collapse at higher temperatures (Hou et al., 2006; Liang et al., 2008; Lin et al., 1999; Yoon et al., 2000). Ying et al. showed that a higher surface area associated with microporosity does not contribute to higher ion sorption capacity because of electrical double-layer overlapping (Ying et al., 2002).

Even though carbon aerogel has a relatively high surface area, its capacitance may not be as high as that of mesoporous carbon materials. Furthermore, as microporosity

limits mass transport rates, there may be some kinetic advantage in utilizing materials in which the surface area arises from mesopores. Therefore, in the recent years a wide range of carbon materials such as activated carbon cloth (Oh et al., 2006; Ryoo et al., 2003), ordered mesoporous carbon (Li et al., 2009; Zou et al., 2008a), graphene (Li et al., 2010a, b), carbon nanotubes (Chen et al., 2010; Gao et al., 2009; Gao et al., 2007; Li et al., 2011; Pan et al., 2009; Wang et al., 2006; Zhang et al., 2007), graphitized carbon (Hou et al., 2006), and microporous carbon (Porada et al., 2012) have been developed and utilized for application in the CDI process. Tsouris et al. (2011) have investigated self-assembled mesoporous carbon (MC) electrodes synthesized at the Oak Ridge National Laboratory (ORNL) which have been used in the present study for application in the electrosorption process (Tsouris et al., 2011). The following sections describe the method of synthesis and the standard characterization techniques for mesoporous carbon materials and their application for desalination and energy storage.

2.1.1 Materials Synthesis

The soft-template method for preparing mesoporous carbons has been discussed in detail in the following text. The phenolic precursors, i.e. resorcinol or phloroglucinol, are incorporated into the hydrophilic PEO arms of the structure-directing template, i.e. a copolymer such as Pluronic F127. This is followed by an aldehyde condensation involving formaldehyde or glyoxal, thus crosslinking the phenolics together while "locked" in place by the copolymer structure-directing template (Liang et al., 2008). During carbonization, the copolymer decomposes leaving void spaces in the phenolic carbon polymer, which become the pores. The narrow mesopore size distribution in soft-templated carbon materials is directly related to the use of the copolymer template, while

the pore size is related to the hydrophobic block length in the copolymer template. Carbon aerogel does not have this level of pore control and therefore does not have a narrow mesopore size distribution due to the mesoporosity being introduced through a solvent extraction step prior to curing. The narrow pore size distribution found in templated carbons has the benefit of producing a higher surface area with similar pore volumes found in aerogels, but with pores predominantly in the mesopore regime.

It has been shown that hierarchical structures are good for increased mass-transport throughout the carbon material (Mayes et al., 2010). A new ordered mesoporous carbon material was developed at ORNL using glyoxal, which exhibits a hierarchical structure arising from the cross linking reagent with pore sizes up to 200 nm. It was also shown that mesoporous carbon prepared by self-assembly of block copolymer and phloroglucinol-formaldehyde resin via the soft-template method can be activated by CO_2 and potassium hydroxide (Wang et al., 2010b). Activated mesoporous carbons exhibited high specific surface areas (up to 2000 $m^2 g^{-1}$) and large pore volumes (up to 1.6 $cm^3 g^{-1}$), while maintaining the mesoporous structure.

For gel-based electrodes, resorcinol (8.00 g) and Pluronic F-127 (8.00 g) (BASF) are dissolved in 34 mL ethanol (200 proof, Decon Labs, Inc.) and 34 mL of 3 M hydrochloric acid. After the addition of formaldehyde, the mixture is stirred for 50 minutes, with phase separation occurring at 20 minutes after formaldehyde addition. The mixture is allowed to set and the gel separated followed by the addition of chopped carbon fibers (Toho Tenax 344). The gel-fiber composite is spread onto the roughened surface of graphite current collector plates and covered with a carbon fiber sheet (Hollingsworth and Vose) which is subsequently pressed into the gel lightly. The

composite electrodes are allowed to dry and then cured at 353 K for 24 hours. The plates were carbonized at 1123 K under argon (Mayes et al., 2010; Wang et al., 2010b; Wang et al., 2008). Details about the templating mechanism can be found in Liang and Dai (2006) (Liang and Dai, 2006). The mesoporous carbon used to produce activated carbon (AC) is described in detail in literature (Wang et al., 2010b). Briefly, phloroglucinol (26 g) and Pluronic F127 (52 g) are refluxed in acidic ethanol (1.2 L 200 proof ethanol and 10 mL 12 M HCl) followed by addition of formaldehyde (26 g). The solution is allowed to reflux 3 hrs followed by filtration and carbonization in a nitrogen atmosphere at 1123K. The resulting mesoporous carbon is physically mixed with potassium hydroxide in a 1:4 ratio respectively and heated at 10 K/min to 1123 K for 2 hrs. The carbon is then rinsed with deionized water, stirred in warm dilute hydrochloric acid, and then washed to neutral pH with deionized water. The mesoporous carbon is incorporated into two types of CDI electrodes – activated carbon sheets (ACS), and mesoporous carbon coated graphite plates – as described below.

ACS preparation: Activation is performed by physically mixing the mesoporous carbon powder with solid potassium hydroxide (KOH) and heated in a nitrogen atmosphere at 10 K/min to 1123 K for 2 hours. After cooling, the activated carbon powder is treated with hydrochloric acid followed by washing in deionized water to a neutral pH. The activated carbon is ball milled with high-density zirconia media (Glenn Mills) in isopropanol to produce a carbon powder with an average particle size of 10 microns. Slurries of activated carbon powder are made in an organic solvent with various concentrations of PVDF binder (polyvinylidene fluoride) with dimethylformamide (DMF) as the solvent. The slurry is heated to decrease the viscosity of the solution, and

spread onto a mold for drying. Non-woven carbon fiber paper (Hollingsworth and Vose) and bonded carbon fiber paper, EC-TP2-030 (Toray Industries) are used as both a non-stick mold liner and as a nonporous layer for backing the carbon sheet. ACS samples are generated by drying the slurry under various conditions, including a final treatment at 100°C in a rough vacuum [Figure 2.1 (a)].

MC-coated graphite: The steps for generating MC-coated graphite plates are shown in Figure 2.1 (b). Prior to carbonization, the carbon polymer gel is cast onto graphite plates. The graphite plates must have a rough surface for good adhesion. The graphite plates with carbon polymer are then carbonized under nitrogen at 850°C to produce resorcinol-based (R-type) or phloroglucinol-based (P-type) MC-coated graphite planar CDI electrodes. The mesoporous carbon adheres well to the graphite and does not flake off during cutting with an abrasive disk. This strong adhesion suggests the mesoporous carbon may withstand exposure to liquid shear flows. The gel can be deposited on both sides of the graphite, enabling double-sided electrodes in CDI stacks.

2.1.2 Materials Characterization

2.1.2.1 PSD Measurements

Nitrogen sorption analysis of nanostructured carbon materials is performed using a Micromeritics Gemini Analyzer. Surface area is calculated using the Brunnauer-Emmet-Teller (BET) method or a comparative method (Kruk and Jaroniec, 2001). Pore size distributions are calculated in the 0.05 - 0.2 relative pressure region using the Barrett-Joyner-Halenda (BJH) method (Barrett et al.).

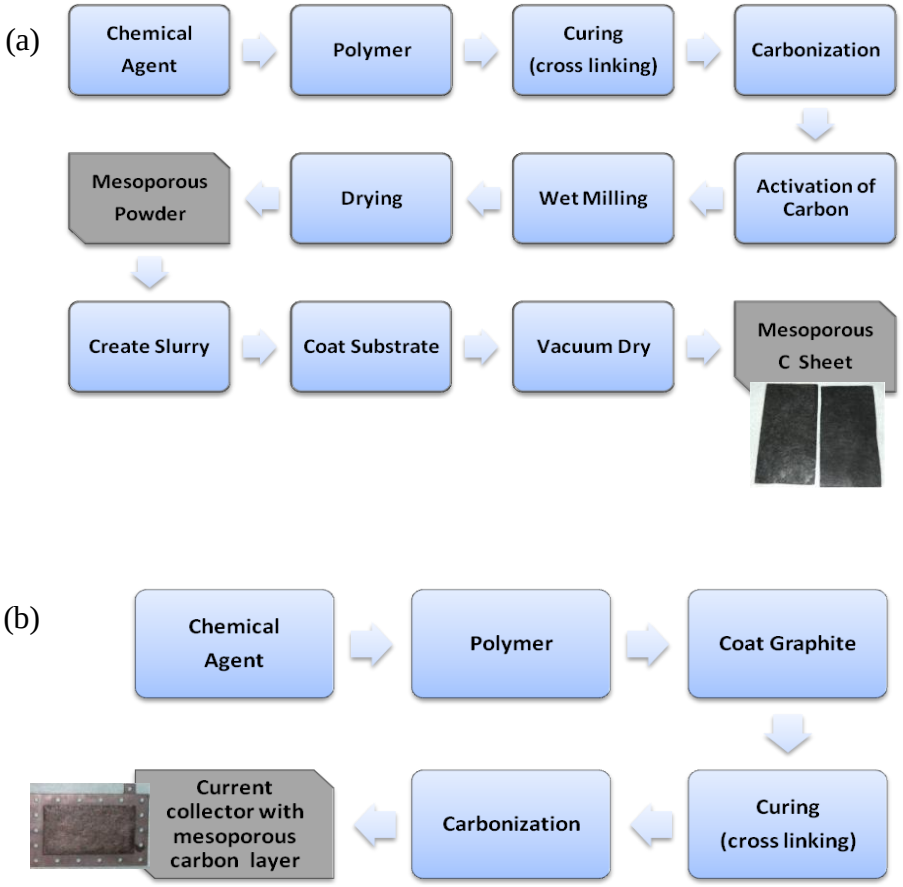

Figure 2.1 Schematics of the procedures for producing (a) sheets containing activated mesoporous carbon and (b) graphite plates coated with mesoporous carbon.

Figure 2.2 shows representative results for nitrogen adsorption isotherms and BJH pore size distributions of the RMCG-FS, PMCG-FS, and commercial carbon aerogel. The commercial carbon aerogel used in these tests is a high surface area material, 289 m^2/g, with a broad pore size distribution and a total pore volume of 0.70 cc/g. This is in contrast to the two templated carbon samples, where slightly lower specific pore volume is achieved with narrower pore size distributions. The surface areas for the RMCG-FS and PMCG-FS active materials on the graphite plates are 488 m^2/g and 610 m^2/g respectively. Both templated carbon materials have total pore volumes of ~0.54 cc/g. The difference in the surface areas for the templated carbons is a result of several parameters during synthesis, including reaction time and ambient humidity. Stopping the reaction early can result in a lower surface area as well as a less humid environment, which influences hydrogen bonding during self-assembly.

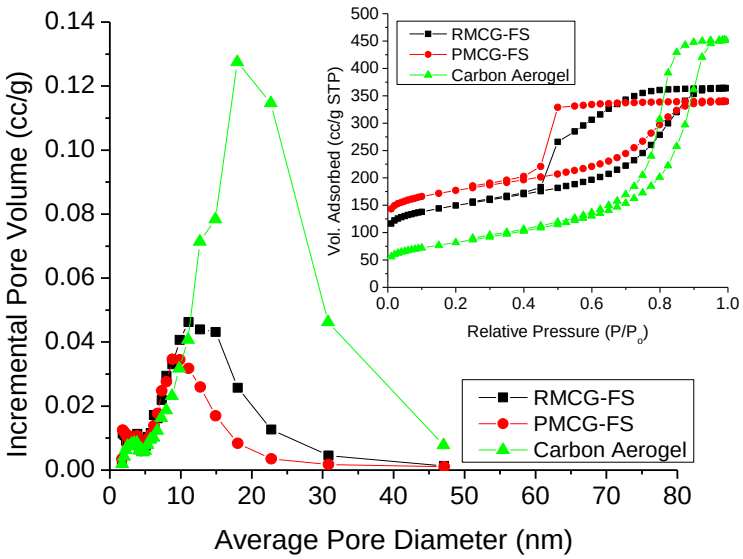

Figure 2.2 Nitrogen sorption isotherms and BJH pore size distributions for R-type, P-type MC carbon, and carbon aerogel materials.

The primary difference between the RMCG-FS and PMCG-FS is the hierarchical porosity found in the PMCG-FS material. The PMCG-FS material has ~8 nm mesopores within a macroporous carbon matrix where pores from 50 nm to 300 nm can be observed (Mayes et al., 2010). This hierarchical porosity is believed to enable higher active surface area and increased transport rates of ions through the material. Without the hierarchical structure, the RMCG-FS material is believed to have slower ion sorption kinetics than the PMCG-FS carbon. The ACS electrode suffers a dramatic loss if surface area is compared to the starting material due to the use of PVDF as a binder from pore blockage or partial pore filling. The starting surface area of 1700 m^2/g is reduced to 364 m^2/g upon generation of the ACS electrode. This negatively affects the sorption capacity, as the capacity is directly related to the surface area of the porous electrode material.

2.1.2.2 Cyclic Voltammetry

Cyclic voltammetry experiments are performed with a Bioanalytical Systems (BAS, West Lafayette, IN) voltammetric analyzer (CV-50W Version 2) connected to a BAS C2 cell stand. The experiments employ three types of electrodes: (1) the working electrode consists of a platinum wire with a small monolithic carbon sample clipped at the end; (2) the counter electrode is a platinum wire attached to a large piece of carbon aerogel, serving as a current collector; and (3) the BAS Model RE-1 (Ag/AgCl electrode immersed in a 3 M NaCl electrolyte solution) is used as the reference electrode. The carbon samples are immersed in the cell solution such that proper wetting conditions are maintained during the experiment. All experiments are carried out under a flow of nitrogen gas.

For the analysis of CV data, the measured electrical current is divided by the scan rate and weight of the sample to yield the specific capacitance. The specific capacitance of carbon aerogel in CV experiments has been reported in previous studies (Hou et al., 2006; Yang et al., 2003). Representative results in Figure 2.3 for a voltage range of ±0.5 V, a scan rate of 1 mV/s, with NaCl and $CaCl_2$ salt solutions show that the activated MC sheets have approximately 50% higher specific capacitance than commercial carbon aerogel sheets. The capacitance for the high ionic-strength solutions is slightly higher, because more ions participate in the electrical double layer formation in solutions of higher ionic-strength. The results obtained indicate that the MC material has higher capacitance than carbon aerogel sheets.

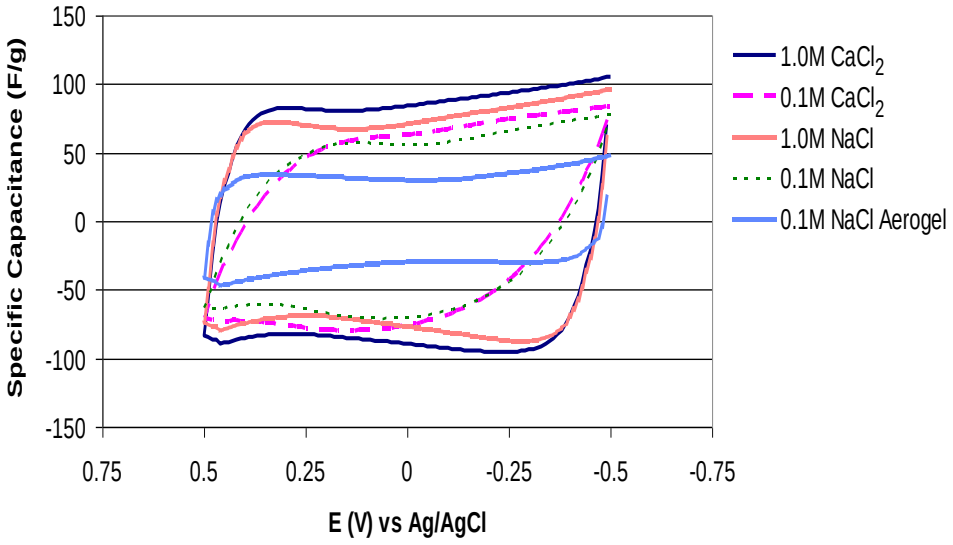

Figure 2.3 Cyclic voltammetry results with activated MC sheets (ACS) and commercial carbon aerogel using 10 mV/s scan rate.

2.2 Application of Electrosorption in Desalination and Energy Storage

The phenomenon of electrosorption of ions by porous carbon electrodes has applications in water treatment and energy storage by supercapacitors. Capacitive Deionization, a method for water desalination is based on the electrosorption of ions by charged carbon electrodes of high surface area. Moreover, during charging of carbon electrodes energy is stored which can be harvested during regeneration of electrodes. Electrical double layer (EDL) capacitors store energy by sorption of ions by porous carbon materials which are electrochemically stable and have a high surface area. The following sections discuss in detail the capacitive deionization technology and energy storage by the electrosorption phenomenon.

2.2.1 Capacitive Deionization Technology for Desalination of Water

The laboratory-scale CDI reactor consists of a single pair of carbon electrodes and a pair of current collectors (Figure 2.4). For carbon aerogel and activated MC sheets, the current collectors are made of titanium plates, and the carbon sheets are taped at the edge on the current collectors. For the MC-coated graphite, the graphite plates play the role of both supporting material and current collectors. The electrodes are held at a spacing of ~6 mm by a hollow piece of Plexiglas. The power is supplied to the cell by connecting the current collectors to a direct-current (dc) HP 3632A power supply (Hewlett Packard, Loveland, CO) with a voltage range of 0 to 15 V and a current range of 0 to 7 A. The conductivity is measured at the cell exit stream by using a conductivity meter (model 835 Multi Cell (Au) with Model 3082 EC Meter, Amber Science, Inc., Eugene, OR). The aqueous solution made from Instant Ocean (Aquarium Systems) is continuously recycled

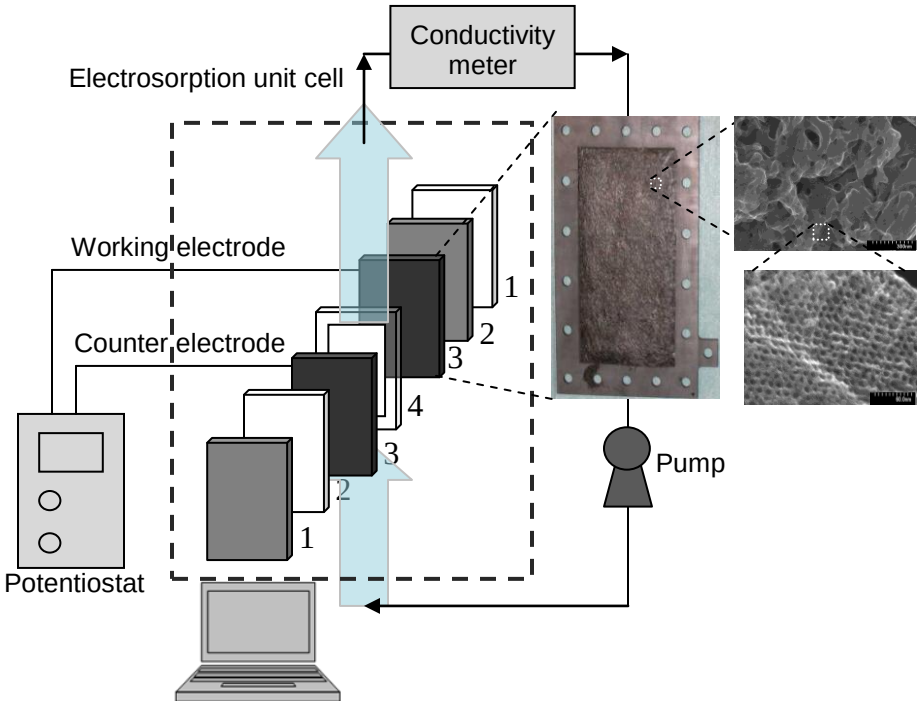

Figure 2.4 Single-cell capacitive deionization reactor with two half cells each of which containing (1) a Plexiglass cover, (2) a current collector, (3) a carbon electrode, and (4) a middle hollow plate. Right: STEM images of the P-type mesoporous carbon utilized to produce the MC-coated graphite electrode materials showing uniform pores of ~8 nm (bottom right) with a combined hierarchical meso- and macro-porosity (top right).

through the system using a micropump until steady state conditions are obtained. A solution volume of 100 ml was maintained in the system. Regeneration is carried out by shorting the electrodes and discharging the cell at 0 V.

Experiments have been conducted to compare the carbon aerogel and the newly synthesized activated MC sheets and MC-coated graphite plates (Tsouris et al., 2011). Mesoporous carbon performed much better than carbon aerogel under the conditions of the experiment. It was associated with 25% drop in conductivity as compared to 2% drop for carbon aerogel (Figure 2.5).

In a recent publication by Mayes et al. (Mayes et al., 2010), the R and P types of MC-coated graphite were compared for potential application in the CDI process. The main difference between these two materials is that the R-type has a narrow pore size distribution in the range of 6-10 nm whereas the P-type has the narrow mesopore size distribution with a maximum at 7.5 nm, coupled with macropores with sizes between 60 and 300 nm. Because of the relatively wide pore size distribution, the P-type MC-coated graphite showed a faster deionization rate than that of the R-type (Mayes et al., 2010). The results obtained in these studies suggest that mesoporous carbon materials are superior to carbon aerogel for application in capacitive deionization. MC-coated graphite materials exhibit a higher capacity at higher concentrations of salts. Thus, these materials are a more suitable choice for carrying out desalination of salt water by the CDI process. Among the MC-coated graphite materials, the P-type material is most suited for high concentration of dissolved salt and faster deionization rates.

2.2.2 Blue Energy Recovery Cycle

Energy obtained from mixing fluids of different salinities, referred to as Blue Energy, is a promising renewable energy source. In delta areas, where a river with low-salinity water flows into the saline seawater, there is immense potential for harvesting energy. Mixing of a highly concentrated saline solution with fresh water dissipates more than 2.2 MJ of free energy per m^3 of fresh water treated (Pattle, 1954). It has been

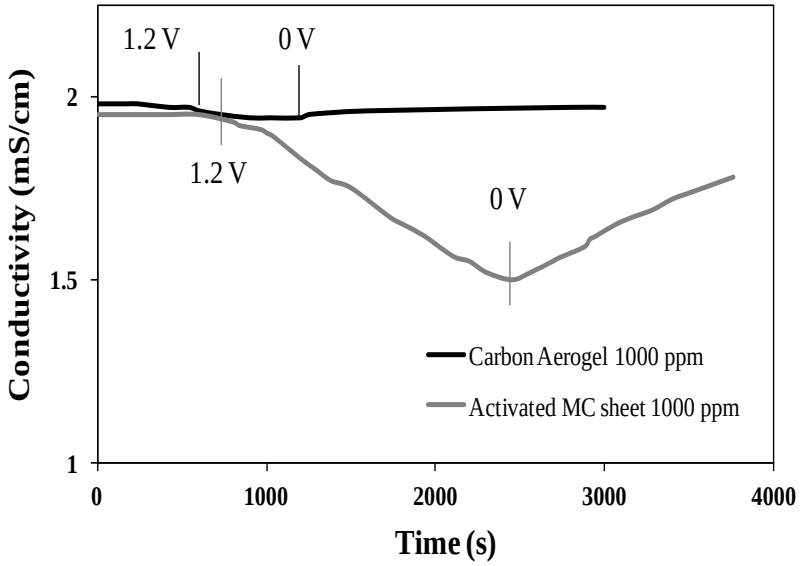

Figure 2.5 Representative capacitive deionization test results: carbon aerogel sheets and activated MC sheets. Conditions: 1000 ppm initial concentration of Instant Ocean, at 1.2 V applied voltage. The electrical conductivity of the solution dropped by 2% for carbon aerogel and 25% for activated MC sheets. After ~2,500 s, the conductivity increased because the applied potential was turned to 0 and the electrodes were shorted.

estimated that the total power generated from all large estuaries in the world could amount to 2 TW, which can cover 20% of the worldwide energy demand (Boon and van Roij, 2011; Wick and Schmitt, 1977). Traditionally, pressure-retarded osmosis (Levenspiel and Godfrey, 1974; Loeb, 1976; Loeb et al., 1976; Thorsen and Holt, 2009) and reverse electrodialysis (Długołęcki et al., 2008; Post et al., 2008; Veerman et al., 2009; Weinstein and Leitz, 1976) have been used to transform Blue Energy into mechanical or electrical work. However, high membrane cost and short life due to membrane fouling hinder the large-scale application of this process (Brogioli, 2009). Recently, a new method using high-capacitance carbon electrodes based on the contraction and expansion of electrical double layers inside the pores of carbon has been proposed (Brogioli, 2009). Reversible cycles that alternate charging and discharging in

supercapacitors using saline and freshwater streams have been developed (Boon and van Roij, 2011; Brogioli, 2009; Brogioli et al., 2011; La Mantia et al., 2011). The carbon electrode materials can help obtain a recovery efficiency as high as 74% of the free energy change (La Mantia et al., 2011). The charging-discharging process inside the nanopores of carbon electrode is influenced by the pore size distribution (Feng et al., 2011; Huang et al., 2008a, b). Ionic competition comes into play when multivalent ions are present along with monovalent ions. In this case, transport of ions is influenced by the ion valence and diameter. Processes for ionic separation based on the difference in ionic charge have also been recently developed (Gao et al., 2009).

2.3 Numerical Modeling of the Electrosorption process

Apart from durable and high-capacity electrode materials, fast exchange of ions between the electrodes and electrolyte solution is required for an efficient operation of the CDI process. Biesheuvel has presented a thermodynamic model for work required for ion removal during a cycle in the CDI process (Biesheuvel, 2009). Biesheuvel and Bazant (Biesheuvel and Bazant, 2010) have also presented a model for capacitive charging and desalination by ideally polarizable porous electrodes, excluding the effect of Faradaic reactions or specific adsorption of ions, valid in the case of a thin EDL. The authors have discussed the theory for the case of a dilute, binary electrolyte using the Gouy-Chapman-Stern (GCS) model of the EDL. This model has been extended to include a dual-porosity approach with macropores and micropores (Biesheuvel et al., 2011). Biesheuvel et al. (Biesheuvel et al., 2012) also presented a porous electrode theory based on electrodes composed of solid particles that are porous themselves. The pore distribution consists of macroporosity outside the particles through which the ions are transported, and the

micropores inside the particles, where the electrical double layers are formed. Bieshuevel and Bazant neglected the Stern layer capacitance and this approximation led to two nonlinear partial differential schemes that were solved numerically.

2.3.1 Model Description

The 1-D model for transport in porous media has been proposed by Biesheuvel and Bazant (Biesheuvel and Bazant, 2010). The porous electrode is divided into pore space filled with quasi-neutral electrolyte and a solid matrix. The solution inside the pore space exchanges ions with a charged, thin double-layer "skin" on the electrode matrix. The system is modeled using a porous electrode of thickness L_{elec} and a thin mass transfer layer just outside the electrode of length L_{SDL}. The approach is based on Newman's macroscopic porous electrode theory (Johnson and Newman, 1971; Newman and Tiedemann, 1975; Newman and Thomas-Alyea, 2004b) with the same assumptions applied. The porous electrode is treated as a homogeneous mixture of charged double layers and a quasi-neutral solution (Figure 2.6).

2.3.2 Model Derivation

The relationship between the dimensionless potential in the solution filling the pore space (ϕ) and the equivalent solid phase potential (ϕ_1) can be calculated by using the Gouy-Chapman-Stern (GCS) model assuming dilute solution conditions. The double layer in the GCS model is described by a combination of a charge-free Stern layer of constant capacity and potential difference $\Delta\phi_S$ and a diffuse layer with potential difference $\Delta\phi_D$.

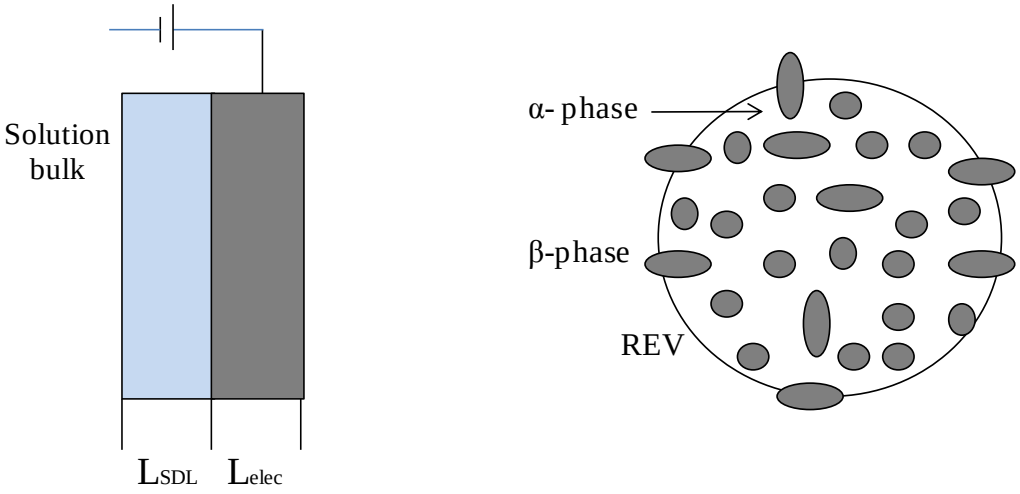

Figure 2.6 (i) Sketch of the model problem. Porous electrode of thickness L_{elec}, relative to a bulk electrolytic solution separated by a stagnant diffusion layer of thickness L_{sdl}. Figure reproduced from reference (Biesheuvel and Bazant, 2010). (ii) Porous medium and representative elementary volume (REV).

$$\phi_1 - \phi = \Delta\phi_s + \Delta\phi_D \tag{2.1}$$

The electrical potentials (ψ) were converted to dimensionless potentials (ϕ) after division by kT/e. The GCS model is described by three main equations. The first is

$$q^* = -2\sqrt{c^*}\sinh(\Delta\phi_D / 2) \tag{2.2}$$

where q^* is a dimensionless surface charge density, i.e., the excess charge in the diffuse layer divided by 2 $\lambda_D C_\infty$; c^* is the dimensionless ion concentration in the pore space at position x (C/C_∞), where C and C_∞ are obtained from N_i and N_{io} by dividing by the Avogadro number, and λ_D is the Debye screening length.

The second equation relates the voltage drop through the Stern layer to q^* by

$$q^* = -\Delta\phi_s / \delta \tag{2.3}$$

where $\delta = \lambda_S/\lambda_D$ and λ_S is the effective thickness of the Stern layer. The third equation gives a formula for the dimensionless excess salt adsorption (w^*):

$$w^* = 4\sqrt{c^*}\sinh^2(\Delta\phi_D/4) \tag{2.4}$$

In order to close the porous electrode model, the dimensionless rate of charge removal from the liquid phase, J^*_{charge}, is related to the charge density, $-q^*$, by

$$\partial q^*/\partial t^* = J^*_{charge} \tag{2.5}$$

and the dimensionless salt adsorption term J^*_{salt} to w^* by

$$\partial w^*/\partial t^* = J^*_{salt} \tag{2.6}$$

J^*_{salt} and J^*_{charge} are made dimensionless by multiplying the rate of salt adsorption (j^*_{salt}) and the rate of charge removal (j^*_{charge}) by $L_{elec}/(J_{lim}\,.\,l_D)$, where $J_{lim} = 2\,D_{eff}C_\infty/L_{elec}$ and D_{eff} is the effective diffusivity.

Originally proposed by Biesheuvel and Bazant (Biesheuvel and Bazant, 2010), the volume averaged transport equations inside the porous electrodes can be written in dimensionless form as:

$$\partial c^*/\partial t^* = D^*_{eff}\nabla^2 c^* - \varepsilon J^*_{salt} \tag{2.7}$$

where t^* is a dimensionless time obtained by rescaling the dimensional time τ_d with $\tau_d = L_{elec}^2/D_{eff}$, and $\varepsilon = \lambda_D/h_p$; the pore thickness h_p is defined as the ratio of the electrode porosity (ε_α) to the electrode specific surface area (a_v), $h_p = \varepsilon_\alpha/a_v$, and D^*_{eff} is the dimensionless effective diffusivity given by the ratio of effective diffusivity and the bulk solution diffusion coefficient (D_{eff}/D).

In dimensionless form, the charge conservation equation becomes

$$\nabla\bullet\left(D^*_{eff}\;c^*\nabla\phi\right) = \varepsilon J^*_{charge} \tag{2.8}$$

In the stagnant diffusion layer (SDL), equations similar to (2.7) and (2.8) are used:

$$\partial c^* / \partial t^* = \nabla^2 c^* \tag{2.9}$$

and $$\underline{\nabla} \bullet (c^* \nabla \phi) = 0 \tag{2.10}$$

2.4 Neutron Imaging

Neutron imaging is a technique for non-destructive investigation of materials that has application in a wide range of disciplines including biology, medicine, materials science, paleontology, soil physics, various industrial sectors, and homeland security. Neutrons have several advantages for imaging over X-rays, electrons, and visible light, as they are non-perturbing, highly penetrating, and able to distinguish between different isotopes. They can determine atomic spacings and crystal structures and reveal magnetic fluctuations. In particular, neutron imaging has been applied to visualize water in fuel cells with an aim to improve performance of fuel cells (Aaron et al., 2011; Bellows et al., 1999; Boillat et al., 2008; Mukundan and Borup, 2009; Park et al., 2008; Pekula et al., 2005; Satija et al., 2004; Tang et al., 2010; Turhan et al., 2006). Neutron imaging has also been used to quantify lithium concentration across electrodes in lithium batteries (Kamata et al., 1997; Lanz et al., 2001; Siegel et al., 2011a). In addition, fields such as soil physics (Menon et al., 2007; Oswald et al., 2008) and biology (Adani and Fallone, 2000; Carey et al., 2008; Carey et al., 2006; Kamali Moghaddam et al., 2008; Kapadia et al., 2008; Sharma et al., 2007) have also utilized neutron imaging for noninvasive studies of various materials of interest.

The basic experimental setup for neutron imaging consists of a neutron source, a collimator which determines the geometric properties of the beam, neutron scintillator

screen, and the sample of study (Figure 2.7). The beam is transmitted through the object and recorded by a neutron scintillator detector. The detector records a 2-dimensional image that is a projection of the sample on the plane. Neutrons are converted to light using a scintillator screen, and the light is captured by the CCD camera.

The present study employs neutron imaging as a tool for observing the diffusion of ions inside mesoporous carbon electrodes. Neutron imaging provides information on the ion transport mechanisms at the electrode-electrolyte interface at nanoscale. A fundamental understanding of the ion transport behavior at the interface can aid in optimization and increasing efficiency in the desalination and energy storage applications in these systems.

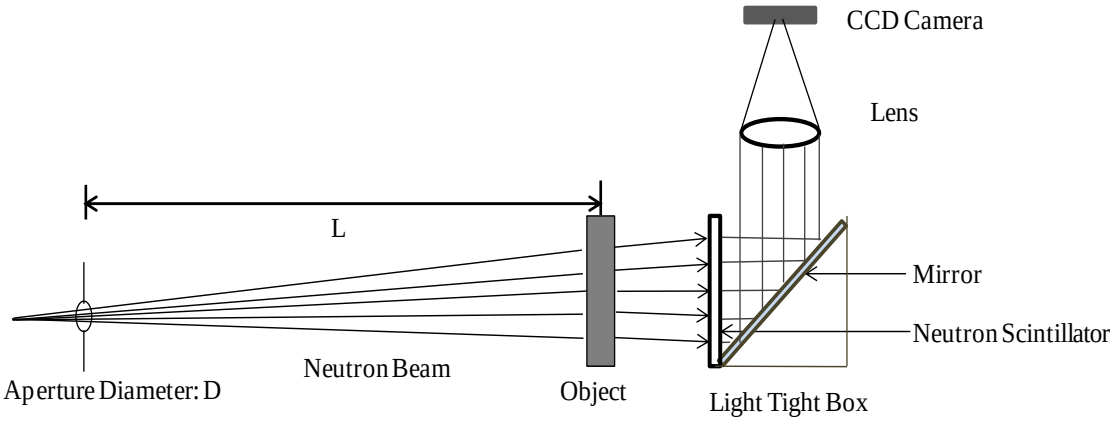

Figure 2.7 Schematic drawing of the experimental setup for neutron imaging.

CHAPTER 3

INFLUENCE OF TEMPERATURE ON ELECTROSORPTION OF IONS FROM AQUEOUS SOLUTIONS USING MESOPOROUS CARBON MATERIALS

Based on the electrosorption of ions by charged electrodes, the capacitive deionization (CDI) method was considered for ion removal from saline water using mesoporous carbon electrodes. Mesoporous carbon was synthesized via a self-assembly method, with a narrow pore size distribution in the range of 6 to 10 nm. It was found that the rates of ion sorption and release by mesoporous carbon electrodes increase with an increase in the temperature of the solution. A drift in the conductivity was observed during electrosorption of Instant Ocean solutions, which may be explained as the result of competition between ions of different valence and size. The diffusion coefficient of ions during electrosorption was evaluated as a function of temperature, and a transport model coupled with an electrical-double-layer model was employed to calculate the mass of salt adsorbed by the electrodes. The calculated cumulative mass of salt captured in the electrical double layers of the electrodes was compared to the experimental data at different temperatures.

3.1 Introduction

The availability of clean affordable water is one of the major challenges facing our society in the present times. Therefore, there has been an interest in developing energy-efficient and economically viable technologies for desalination of water. The capacitive deionization (CDI) method, which is based on the phenomenon of electrosorption of ions, can be used to remove ions from aqueous solutions. Electrosorption involves application of an electrical potential between pairs of electrodes to force the cations and anions towards the oppositely charged electrodes. The ions are held in the electrical double layers (EDL) formed at the surface of the electrodes.

Porous nanostructured carbon materials of high conductivity and high specific surface area have attractive properties as electrode materials for the electrosorption process. Several studies have been carried out to investigate the electrosorption behavior of carbon electrodes (Ayranci and Conway, 2001a; Ayranci and Conway, 2001b; Ban et al., 1998; Kinoshita, 1988; Oren, 2008). A wide range of carbon materials such as carbon aerogel (Farmer et al., 1997; Farmer et al., 1996; Jung et al., 2007; Miller and Dunn, 1999; Xu et al., 2008; Ying et al., 2002), activated carbon cloth (Oh et al., 2006; Ryoo et al., 2003), ordered mesoporous carbon (Li et al., 2009; Zou et al., 2008a), graphene (Mayes et al., 2010; Wang et al., 2010b), carbon nanotubes (Chen et al., 2010; Gao et al., 2009; Gao et al., 2007; Li et al., 2011; Pan et al., 2009; Wang et al., 2006; Zhang et al., 2007), and microporous carbon (Porada et al., 2012) have been utilized for application in the electrosorption of ions. Graphitized carbon has also been investigated for application in the CDI process (Hou et al., 2006).

Apart from durable and high-capacity electrode materials, fast exchange of ions between the electrodes and electrolyte solution is required for an efficient operation of the CDI process. Biesheuvel has presented a thermodynamic model for work required for ion removal during a cycle in the CDI process (Biesheuvel, 2009). Biesheuvel and Bazant (Biesheuvel and Bazant, 2010) have also presented a model for capacitive charging and desalination by ideally polarizable porous electrodes, excluding the effect of Faradaic reactions or specific adsorption of ions, valid in the case of a thin EDL. The authors have discussed the theory for the case of a dilute, binary electrolyte using the Gouy-Chapman-Stern (GCS) model of the EDL. This model has been extended to include a dual-porosity approach with macropores and micropores (Biesheuvel et al., 2011). Biesheuvel et al. (Biesheuvel et al., 2012) also presented a porous electrode theory based on electrodes composed of solid particles that are porous themselves. The pore distribution consists of macroporosity outside the particles through which the ions are transported, and the micropores inside the particles, where the electrical double layers are formed. The authors used a modified-Donnan (mD) method for the micropores, valid for overlapping double layers.

Saline water generated by gas/oil operations, also known as produced water, reaches the surface at elevated temperatures (40-50°C) (Ray and Engelhardt, 1993) and often needs to be treated before reuse or disposal. Since produced water contains relatively high concentrations of dissolved solids, a deionization method is often required to remove ions. Johnson et al. have reported the influence of temperature on desalination performance in electrosorption by porous carbon electrodes. The study reported that there is an improvement in desalination performance when the temperature is increased from

25°C to 50°C, but little improvement in performance is obtained at higher temperatures under 80°C (Johnson et al., 1970). Experimental information and modeling results presented in this study are focused on elucidating the influence of temperature on the electrosorption of ions during the CDI process. Experimental work with CDI is based on novel mesoporous carbon (MC) materials synthesized at the Oak Ridge National Laboratory (Mayes et al., 2010; Wang et al., 2010b; Wang et al., 2008) including resorcinol-based MC-coated graphite with fibers (RMCG-FS), and activated, self-standing MC sheets. Additional information about the application of these materials for the electrosorption of ions can be found in reference (Tsouris et al., 2011). It has been shown that the RMCG-FS electrodes exhibit a slightly higher removal capacity than the activated MC sheets. These materials provide high surface area over a narrow pore size distribution that is ideal for both EDL formation and transport of ions.

In the present study, activated MC sheets and RMCG-FS were used in CDI experiments of sodium chloride and Instant Ocean solutions at different temperatures. A comparison of the results leads to conclusions on the influence of temperature on the performance of mesoporous carbon materials in the deionization process. These conclusions are supported by theoretical results from transport modeling coupled with the EDL theory for sodium chloride and Instant Ocean solutions. A practical implication of the present work is determining whether it would be more effective to treat produced water at its original temperature rather than after it reaches equilibrium with the environmental conditions.

3.2 Materials and Methods

3.2.1 Mesoporous Carbon Materials

Details of the mesoporous carbon used in this study can be found in recent literature (Mayes et al., 2010; Wang et al., 2010b; Wang et al., 2008). In summary, activated mesoporous carbon was synthesized by carbonization of nanostructured polymeric composites, obtained by self-assembly of the triblock copolymer Pluronic F127 and phenol resin in acidic conditions and ethanol. The mixture was heated with continuous stirring while formaldehyde was added. After the solution was heated for 2 hours, the resultant F127 phenol resin polymeric composite particles were separated from the remaining solution. The particles were then washed with ethanol and dried in an oven for 3 hours. Carbonization was carried out under flowing nitrogen gas by heating the polymer particles at 850°C for 2 hours. KOH activation was performed by heating a physical mixture of solid KOH and mesoporous carbon particles in a tube furnace under flowing nitrogen gas.

A fabrication method developed to produce mesoporous carbon sheets involved forming a paper-like product from a slurry or paste containing activated carbon powder, a binder, and a solvent. After activation, the carbon products were ball milled with high-density zirconia media (Glenn Mills) to produce a fine powder. Polyvinylidene fluoride (PVDF, Aldrich Chemicals) was used as the binder or bonding agent, due to its inert interaction with other materials involved in CDI and with dimethylformamide as the slurry solvent. Slurries were made with varying amounts of the PVDF binder. A typical slurry for a 75 mm by 150 mm by 1 mm thick final sheet consisted of 5 grams of carbon with different weights of PVDF in approximately 15-17 grams of solvent. The slurry was

prepared by stirring the carbon into the solvent in which the PVDF was previously dissolved. The slurry was then heated to 50°C to decrease the viscosity of the solution and spread onto a mold for drying. Bonded carbon fiber paper (Toray Industries) and a non-woven carbon fiber paper (Hollingsworth and Vose) were used as a support for the carbon sheet. The samples were then dried under vacuum at 100°C for CDI experiments. Samples from the sheets were also prepared for BET (Brunauer-Emmett-Teller) surface area measurements.

MC-coated graphite plates were also generated by applying the precursor templated resorcinol gel directly onto a graphite current collector plate of dimensions 100 mm × 200 mm × 1 mm. The gel was carbonized to produce R type (for resorcinol) MC-coated graphite plates (RMCG). It was found that the mesoporous carbon adheres well to the graphite, which also provides mechanical strength, so the combination of mesoporous carbon and graphite is acceptable for a CDI reactor. MC-coated graphite was not chemically activated like the activated MC sheets; however, its specific surface area was greater than 600 m^2/g and slightly lower than the specific surface area of the activated MC sheet (in the range of 1000 m^2/g). Due to the addition of PVDF, the specific surface area of MC sheets was lower than that of the original MC powder by as much as 500 m^2/g. Another potential advantage of MC-coated graphite over MC sheets is better connectivity to the charge collector, thus providing a lower resistance to current flow.

3.2.2 Capacitive Deionization Experiments

Capacitive deionization (CDI) experiments were performed using an electrosorption cell consisting of a pair of electrodes made of activated MC sheets attached to titanium plates or MC-coated graphite plates (Figure 3.1). The electrodes

were kept separated by a central hollow piece Plexiglass at a distance of 0.6 cm. Each half of the electrode cell consisted of a Plexiglass outside wall, a titanium plate with activated MC sheet or MC-coated graphite, and Viton gaskets. The two titanium or graphite plates were supplied electrical potential through a direct-current (dc) power supply (Hewlett Packard model 3632A, Loveland, CO) operating at a range of 0-15 V and 0-7 A. In order to measure the capacitance of MC, a 100-ml solution was maintained and continuously recycled through the system until steady state conditions were obtained.

The conductivity was measured at the cell exit stream by using a conductivity meter (model 835 Multi Cell (Au) with Model 3082 EC Meter, Amber Science, Inc., Eugene, OR). The system was assumed to reach equilibrium when the conductivity reached a constant value.

The solutions used in the experiments were sodium chloride and Instant Ocean solutions (Instant Ocean, Blacksburg, VA), and the temperature was maintained at either 25°C or 40°C for experiments at room temperature and elevated temperature, respectively. Instant Ocean solution is a synthetic seawater formulation consisting of salts providing major ions (Cl^-, Na^+, Mg^{2+}) , minor ions (HCO_3^-, Br^-), and trace elements (Cu, Fe, Ni) found in natural ocean water (NaCl - 23.50 g/L, Na_2SO_4 - 4.00 g/L, KCl - 0.68 g/L, H_2BO_3 - 0.02 g/L, $MgCl_2.2H_2O$ - 10.78 g/L, $CaCl_2.2H_2O$ - 1.47 g/L, $NaHCO_3$ - 0.19 g/L, $Na_2SiO_3.9H_2O$ - 0.03 g/L). Instant Ocean solution was used to investigate the influence of competition between ions of different valence and size. Regeneration was carried out by removing the applied potential and shorting the two electrodes with a cable.

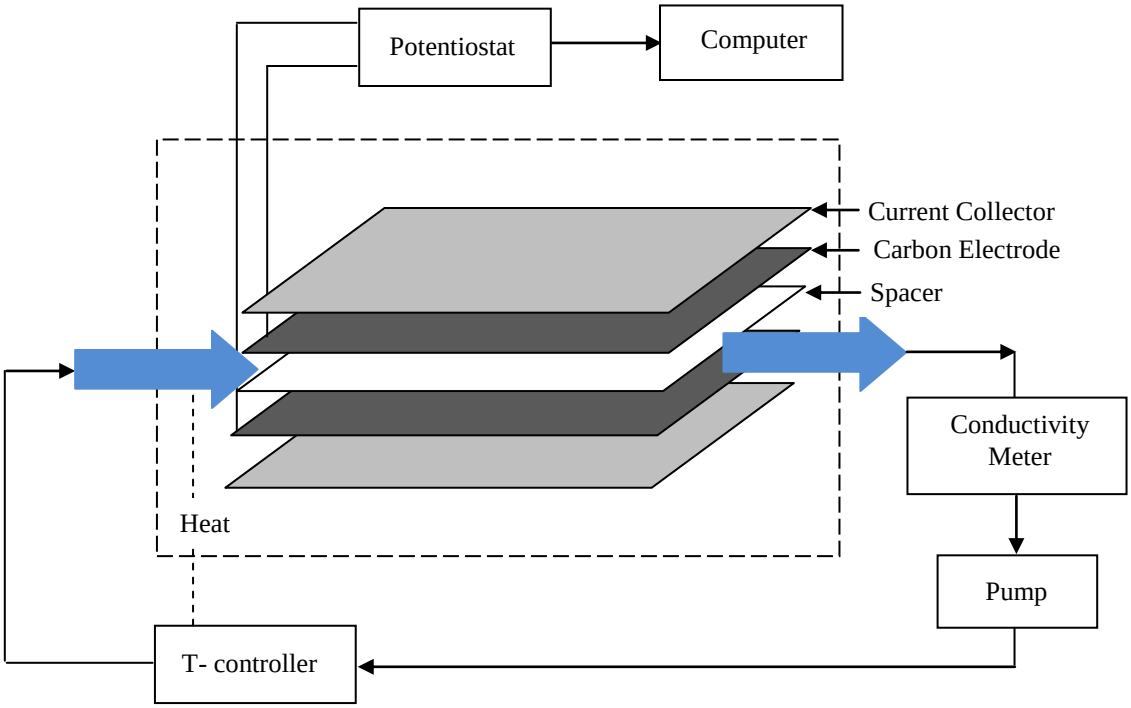

Figure 3.1 Single-cell capacitive deionization reactor with two half cells containing a current collector, a carbon electrode, and a spacer. Left bottom: a temperature controller is used to control the temperature of the cell by providing heat via a heating tape wrapped around the capacitive deionization cell.

3.2.3 Modeling

The 1-D transport model in porous media used in this work is similar to the one proposed by Biesheuvel and Bazant (Biesheuvel and Bazant, 2010). The porous electrode was divided into pore space filled with quasi-neutral electrolyte and a solid matrix. The solution inside the pore space exchanged ions with a charged, thin double-layer "skin" on the electrode matrix. The system was modeled using a porous electrode of thickness L_{elec} and a thin mass transfer layer just outside the electrode of length L_{SDL}. The approach is based on Newman's macroscopic porous electrode theory (Johnson and Newman, 1971;

Newman and Tiedemann, 1975; Newman and Thomas-Alyea, 2004b) with the same assumptions applied. The porous electrode was treated as a homogeneous mixture of charged double layers and a quasi-neutral solution.

The relationship between the dimensionless potential in the solution filling the pore space (ϕ) and the equivalent solid phase potential (ϕ_1) can be calculated by using the Gouy-Chapman-Stern (GCS) model assuming dilute solution conditions. The double layer in the GCS model is described by a combination of a charge-free Stern layer of constant capacity and potential difference $\Delta\phi_S$ and a diffuse layer with potential difference $\Delta\phi_D$.

$$\phi_1 - \phi = \Delta\phi_s + \Delta\phi_D \tag{3.1}$$

The electrical potentials (ψ) were converted to dimensionless potentials (ϕ) after division by kT/e. The GCS model is described by three main equations. The first is

$$q^* = -2\sqrt{c^*}\sinh(\Delta\phi_D / 2), \tag{3.2}$$

where q^* is a dimensionless surface charge density, i.e., the excess charge in the diffuse layer divided by 2 $\lambda_D C_\infty$; c^* is the dimensionless ion concentration in the pore space at position x (C/C_∞), where C and C_∞ are obtained from N and N_o (number of ions per unit volume) by dividing by the Avogadro number (N_{av}), and λ_D is the Debye screening length.

The second equation relates the voltage drop through the Stern layer to q^* by

$$q^* = -\Delta\phi_s / \delta \tag{3.3}$$

where $\delta = \lambda_S/\lambda_D$ and λ_S is the effective thickness of the Stern layer. The third equation gives a formula for the dimensionless excess salt adsorption (w^*):

$$w^* = 4\sqrt{c^*}\sinh^2(\Delta\phi_D / 4) \tag{3.4}$$

In order to close the porous electrode model, the dimensionless rate of charge removal from the liquid phase, J^*_{charge}, is related to the charge density, $-q^*$, by

$$\partial q^* / \partial t^* = J^*_{charge} \tag{3.5}$$

and the dimensionless salt adsorption term J^*_{salt} to w^* by

$$\partial w^* / \partial t^* = J^*_{salt} \tag{3.6}$$

J^*_{salt} and J^*_{charge} are made dimensionless by multiplying the rate of salt adsorption (j^*_{salt}) and the rate of charge removal (j^*_{charge}) by $L_{elec}/(J_{lim} . \lambda_D)$, where $J_{lim} = 2\ D_{eff}C_\infty/L_{elec}$ and D_{eff} is the effective diffusivity.

Originally proposed by Biesheuvel and Bazant (Biesheuvel and Bazant, 2010), the volume averaged transport equations inside the porous electrodes can be written in dimensionless form as:

$$\partial c^* / \partial t^* = D^*_{eff} \nabla^2 c^* - \varepsilon J^*_{salt} \tag{3.7}$$

where t^* is a dimensionless time obtained by rescaling the dimensional time τ_d with $\tau_d = L_{elec}^2/D_{eff}$, and $\varepsilon = \lambda_D / h_p$; the pore thickness h_p is defined as the ratio of the electrode porosity (ε_α) to the electrode specific surface area (a_v), $h_p = \varepsilon_\alpha/a_v$, and D^*_{eff} is the dimensionless effective diffusivity given by the ratio of effective diffusivity and the bulk solution diffusion coefficient (D_{eff}/D).

In dimensionless form, the charge conservation equation becomes

$$\nabla \bullet \left(D^*_{eff}\ c^* \nabla \phi \right) = \varepsilon J^*_{charge} \tag{3.8}$$

In the stagnant diffusion layer (SDL), equations similar to (3.7) and (3.8) are used:

$$\partial c^* / \partial t^* = \nabla^2 c^* \tag{3.9}$$

and $$\underline{\nabla} \bullet (c^* \nabla \phi) = 0 \tag{3.10}$$

In their original work, Biesheuvel and Bazant (Biesheuvel and Bazant, 2010) did not solve the full set of equations. They neglected the Stern layer thickness, and this approximation led to two nonlinear partial differential equations that were solved numerically. They also conducted a detailed study of the dynamical behavior of the aforementioned equations using an asymptotic analysis involving the small parameter ε (λ_D/h_p). In the present work, we have solved the full model equations without neglecting any variable.

The solution of the full problem requires solving simultaneously equations (3.7) and (3.8) for the dimensionless salt concentration and potential inside the porous electrode together with equations (3.5) and (3.6) for the evaluation of the source terms J^*_{salt} and J^*_{charge}. The q^* and w^* values to be used in equations (3.5) and (3.6) are calculated using the GCS model from equations (3.1) through (3.5). Equations (3.9) and (3.10) are solved to calculate the dimensionless salt concentration and potential outside the porous electrode.

Equations (3.1) through (3.4) are non-linear algebraic equations, equations (3.7) and (3.9) are parabolic partial differential equations, while equations (3.8) and (3.10) are elliptic partial differential equations. Thus, a numerical procedure was adopted to solve the system. Parabolic equations were solved using an explicit finite differences scheme, while the elliptic equations were solved using an over relaxation iterative scheme. The

nonlinear algebraic solutions were solved using iterative schemes. It was found that a global solution scheme worked well to solve the combined system simultaneously. Instead of solving individual equations in sequence, the global system was solved iteratively at the same time. In one system iteration, all equations were solved once using a combination of old values and just calculated values at the same time. In this way, new values were used as soon as they were calculated.

The following procedure was used:

1. A time value was set.
2. An iterative procedure was used for all the equations, and the solution of the GCS model was started.
3. The values of q^* and w^* were calculated iteratively from equations (3.5) and (3.6) for all x values inside the electrode.
4. The values of c^* and ϕ were calculated numerically for all x values inside the porous electrode.
5. The values of c^* and ϕ were calculated numerically for all x values inside the SDL.
6. Convergence was checked by comparing a square norm of the ϕ profile inside the electrode with the value of the same profile in the previous iteration.
7. In case of convergence, a new time value was set and the procedure was started again. If there was no convergence, the most recent values were used in a new iteration for the same time.

3.3 Results and Discussion

3.3.1 Materials Characterization

Barrett-Joyner-Halenda (BJH) pore size distributions and nitrogen sorption isotherms for the activated MC sheets and activated MC powder that was used to make the sheets are shown in Figure 3.2. The mesoporous carbon maintains the mesoporous structure after activation with base (Wang et al., 2010b) resulting in a bimodal porosity arising from the mesopores (dictated by the Pluronic F127 template used) and micropores (from KOH activation). The use of polymeric binders is a common method to form monolithic materials from powders. This method, however, can block or partially fill pores as the polymer encapsulates and glues the particles together. The use of PVDF as a binder is common in battery and supercapacitor research. However, it is known to block or partially fill pores due to the polymer untangling in the solvent used, i.e., dimethylformamide (DMF) or N-methylpyrrolidone (NMP) (Park and Choi, 2010). The effect of the pore blockage or filling is observed in the nitrogen sorption isotherms. The decrease in surface area (1567 m^2/g for the activated carbon vs. 1040 m^2/g for the activated carbon-PVDF composite) and pore volume (1.26 cc/g for the activated carbon vs 0.96 cc/g for the activated carbon-PVDF composite MC sheet) is another indication of either pore blockage or partial filling of the pores. A direct implication of this loss of surface area is a loss of ion capacity. Indirectly, ion diffusion can be impacted through a more tortuous route created in the polymer-mesoporous carbon composite. The ion diffusion would then impact charge-discharge rates and the overall efficiency of the electrode by masking the true capacity and charge-discharge rates.

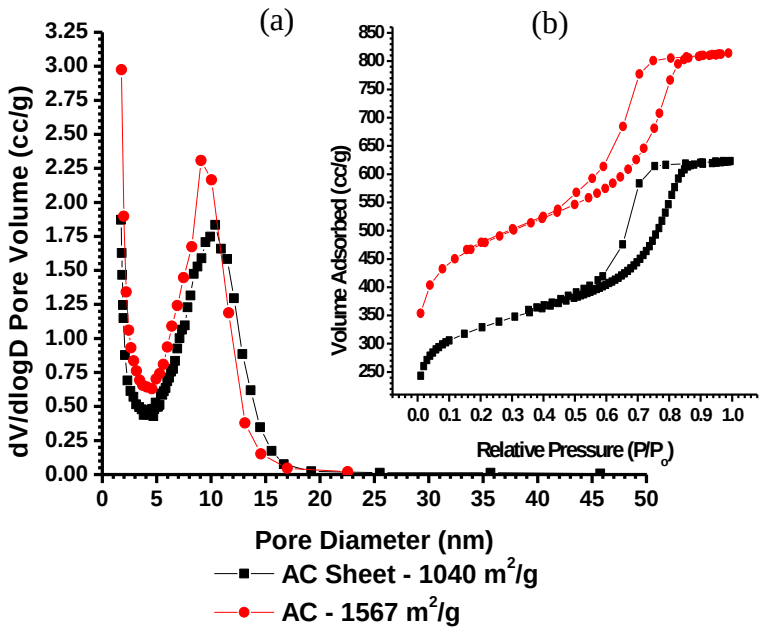

Figure 3.2 (a) Barrett-Joyner-Halenda (BJH) pore-size distributions and (b) Nitrogen adsorption isotherms for the activated MC sheets used in the capacitive deionization experiments.

3.3.2 Influence of Temperature on Electrosorption from Instant Ocean Solution

3.3.2.1 CDI Experiments

The produced water temperature (40-50°C) is typically higher than the surface temperature. Since application of CDI is being considered for the treatment of produced water, CDI experiments were conducted to determine whether it would be more effective to treat water as it is produced rather than storing it and letting its temperature equilibrate with the environment. As shown in Figure 3.3, the sorption rate was higher at a higher temperature. Specifically, 49% faster sorption was recorded during the first 1000 seconds at 40°C in electrosorption from Instant Ocean solution of initial concentration 5000 ppm. At 25°C, the conductivity dropped by 1.8 mS/cm within 4500 seconds, while at 40°C, it dropped by 2.1 mS/cm within 3500 seconds.

The regeneration was also faster at a higher temperature, with a 0.4 mS/cm higher conductivity reached within 1000 seconds at 40°C (Figure 3.4). It should be noted that the conductivity was corrected for the direct effect of temperature using a calibration procedure, thus the comparison is done essentially for the ambient temperature. The final conductivity at 40°C was 0.7 mS/cm higher after 5000 seconds, as compared to the value at 25°C. Figure 3.5 illustrates the drifting in conductivity observed at a higher temperature of 46°C in ion electrosorption from Instant Ocean solution of initial concentration of 945 ppm. Thus, interesting observations were made with Instant Ocean solution at a higher temperature, such as drifting of conductivity before regeneration and a drop in conductivity as soon as the potential was removed, as illustrated in Figures 3.4 and 3.5.

Another set of experiments were conducted to compare the performance of MC-coated graphite at different temperatures for 5000 ppm Instant Ocean solution (Figure 3.6). The rates of sorption and regeneration for MC-coated graphite were higher at a higher temperature of 40°C. The results suggest that MC coated graphite (R type) is a suitable material for CDI at elevated temperatures. There is also a drift in the conductivity before regeneration at 40°C (Figure 3.6b). The hypothesis for the observations of drifting in conductivity during electrosorption and initial drop in conductivity during regeneration observed with Instant Ocean solution is that these phenomena are the result of competition between ions of different size and valence.

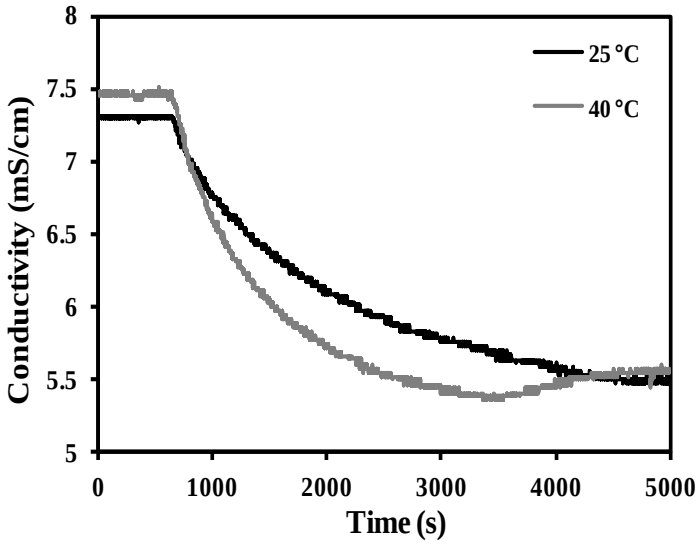

Figure 3.3 Influence of temperature on ion electrosorption from Instant Ocean solution of initial concentration 5000 ppm with activated MC sheets: the sorption rate is 49% higher at 40°C during the first 1000 seconds.

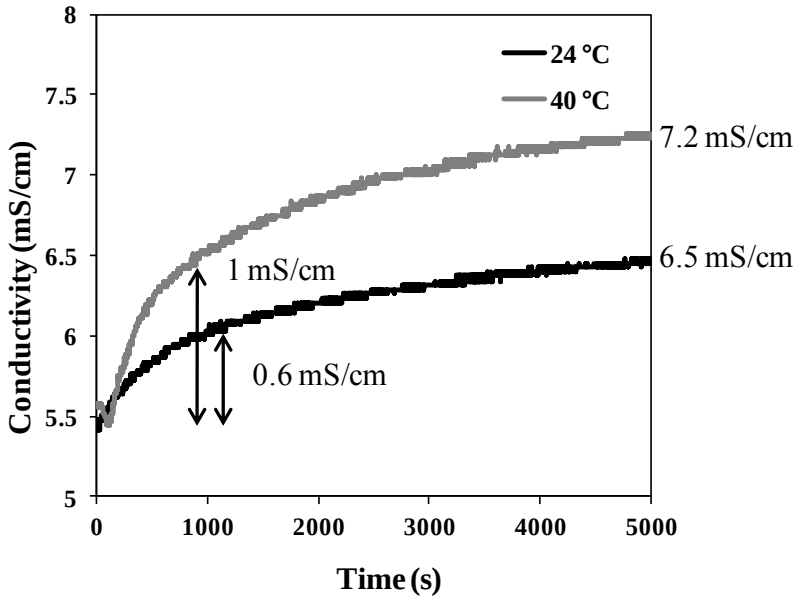

Figure 3.4 Influence of temperature on ion desorption (regeneration) in Instant Ocean solution with activated MC sheets: faster regeneration is observed at 40°C.

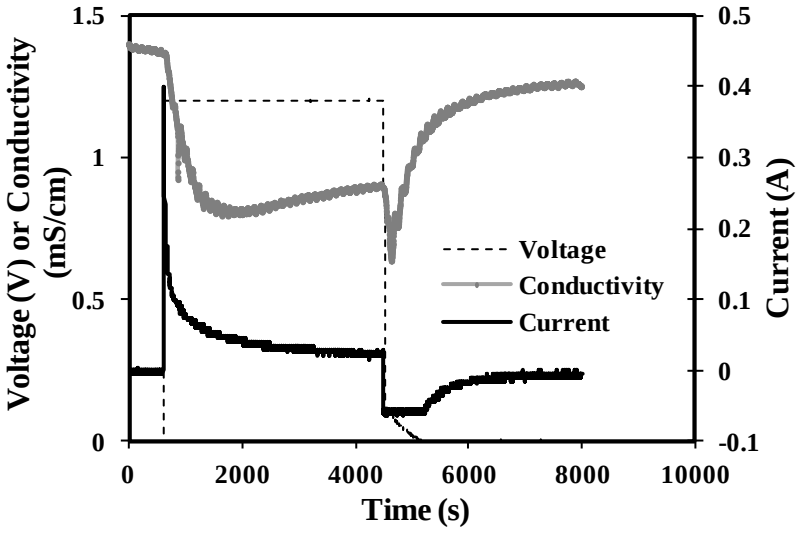

Figure 3.5 Ion electrosorption from Instant Ocean solution with activated MC sheets. Temperature = 46°C, initial concentration = 945 ppm.

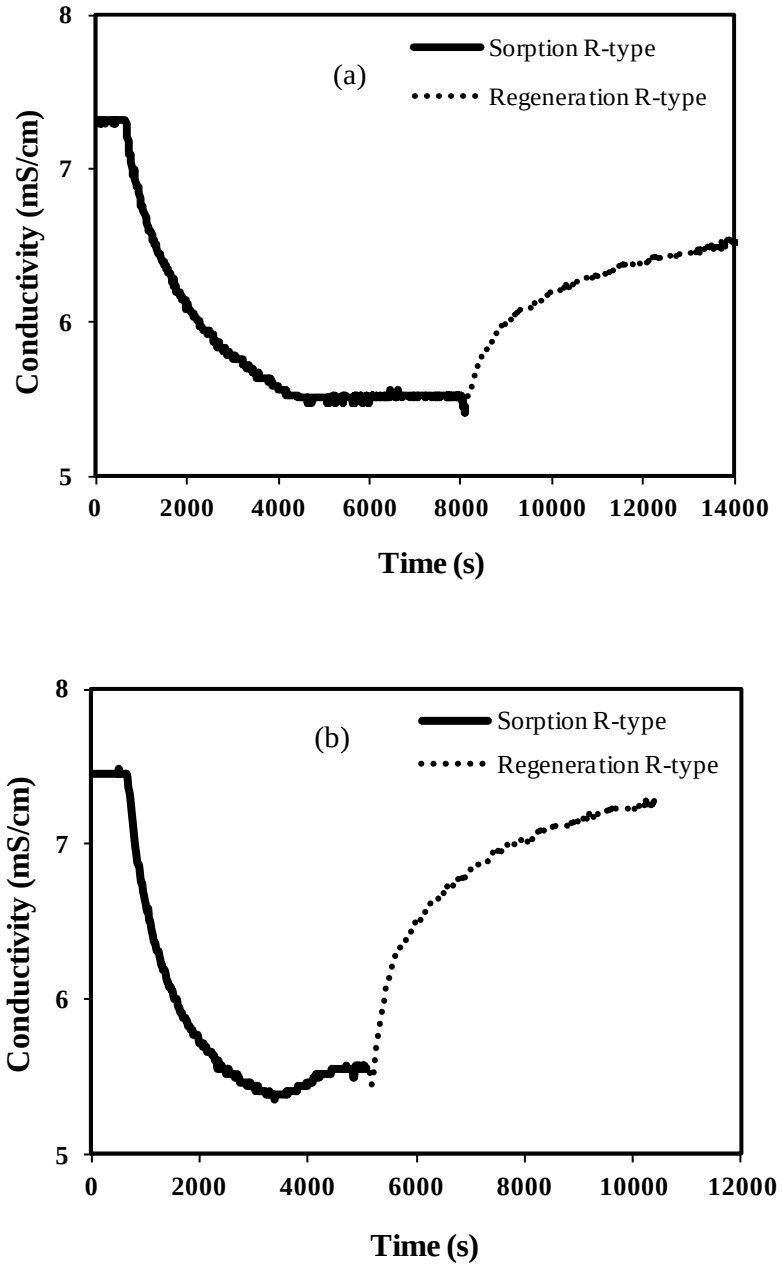

Figure 3.6 Comparison of CDI performance with mesoporous-carbon-coated graphite (R type) in 5000-ppm Instant Ocean solutions: (a) at room temperature (25°C); (b) at higher temperature (40°C).

3.3.3 Influence of Temperature on Electrosorption from Sodium Chloride Solutions

3.3.3.1 CDI Experiments

Another set of experiments were conducted to test the hypothesis proposed in the previous section (Section 4.2.1) that the behavior observed with mixtures of ions at higher temperature is due to the competition of ions of different size and valence (Figure 3.7). In these experiments, NaCl solution was used to compare the data obtained with Instant Ocean solution. Experiments were conducted with NaCl solution at 5000 ppm, and the abnormal behavior with Instant Ocean solution (Figures 3.4, 3.5 and 3.6b) was not observed with NaCl solution. Drifting and conductivity drop during regeneration did not occur when the experiments were conducted with NaCl solution. Unexpected phenomena occurring with Instant Ocean solution at higher temperatures can be explained by the higher mobility of smaller ions, which are not very effective charge carriers to counterbalance the surface charge. As soon as the electrodes are charged, small ions of higher mobility enter the pores to counterbalance the charge. Multivalent ions, which can more effectively neutralize the surface charge, enter the pores slowly and replace smaller monovalent ions. This behavior can explain the drifting that is observed with Instant Ocean solution after 2000 seconds in Figure 3.5. During regeneration, when the pores are occupied by mostly large multivalent ions, which diffuse very slowly from the pores to the bulk solution, smaller counterions diffuse inside the pores to counterbalance the charge before coions and counterions start diffusing from the pores to the bulk solution. This behavior causes the conductivity to drop first, before increasing during regeneration. These phenomena occurred only for Instant Ocean solutions at elevated temperatures (Figure 3.4, 3.5, 3.6b) because of the much higher mobility of the

smaller ions as compared to the mobility of the larger, multivalent ions. When sodium chloride solution was used instead of Instant Ocean (Figure 3.7), the phenomena described above were not observed.

3.3.4 Modeling the Influence of Temperature during Transport in Porous Media

Theoretical results were obtained using the transport model developed by Biesheuvel and Bazant (Biesheuvel and Bazant, 2010). The effective diffusion coefficient, D_{eff}, needed in equation (3.7) within the mesoporous carbon electrodes was estimated based on the solution diffusion coefficient and the equations reported by Ryan et al. (Ryan et al., 1981) by matching the experimental data with the theoretical results.

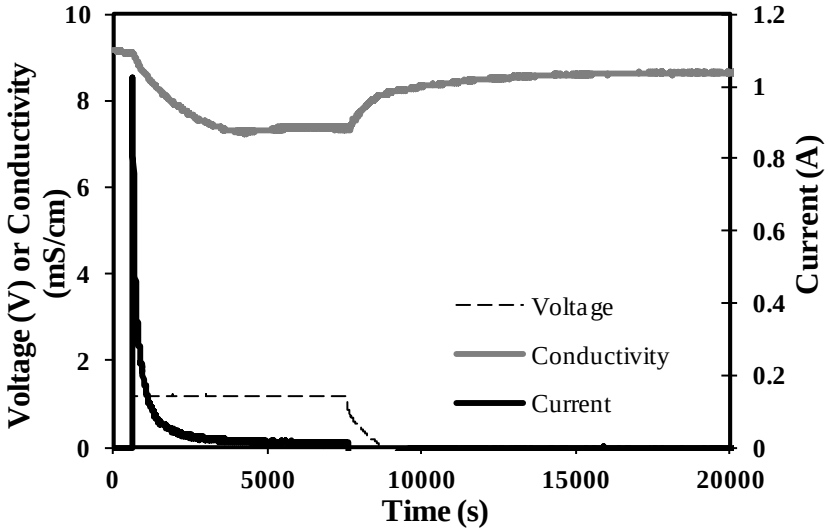

Figure 3.7 Ion electrosorption from NaCl solution with activated MC sheets. Temperature = 40°C, initial concentration = 5000 ppm.

In the first method, employed for NaCl electrolyte solution, an isotropic porous medium was assumed to estimate the influence of geometry on the effective diffusivity value. The equation used, obtained from Ryan et al. data (Ryan et al., 1981), was:

$$D_{eff} / D = \varepsilon_\alpha^3 - 0.7458\,\varepsilon_\alpha^2 + 0.7452\,\varepsilon_\alpha \tag{3.11}$$

where ε_α is the electrode porosity and D is the bulk solution diffusion coefficient.

The solution diffusion coefficient of the salt (D) was calculated based on the procedure by Neumann and Thomas-Alyea (Newman and Thomas-Alyea, 2004a).

$$D = [D_+ D_- (z_+ - z_-)]/(z_+ D_+ - z_- D_-) \tag{3.12}$$

This expression applies to a binary salt based upon the individual ionic diffusivities (D_+ and D_-) and ionic valences (z_+ and z_-). The ionic diffusivities vary with temperature following the temperature dependence proposed by Newman and Thomas-Alyea (Newman and Thomas-Alyea, 2004a):

$$D_i \mu_I / T = \text{Constant} \tag{3.13}$$

where μ_I is the solution viscosity, which also depends on temperature. Figure 3.8 shows the variation of the NaCl solution diffusivity with temperature based on equations (3.12) and (3.13). Experimental data reported in reference (Newman and Thomas-Alyea, 2004a) at 25°C were used to obtain the diffusivity values of D_+ and D_- as functions of temperature.

3.3.4.1 Influence of Temperature on Ion Transport in the Pores for Instant Ocean Solution

The experimental data of cumulative salt mass taken up by the electrodes vs time presented in Figure 3.3 are again depicted in Figure 3.9 and compared with the modeling results that were obtained by using the transport model for sodium and chloride ions. The

cumulative mass includes the ions adsorbed on the electrode surface plus the salt mass trapped in the solution inside the pores of the solid electrodes.

Through an iterative procedure, a good description of the experimental data for one temperature was obtained by adjusting the three parameters: porous medium effective area (A_{eff}), the dimensionless effective diffusivity ($D^*_{eff} = D_{eff}/D$), and the ratio of Stern layer thickness and Debye length (δ). The value of dimensionless effective diffusivity ($D^*_{eff} = D_{eff}/D$) represents the transport influence on the uptake process, and $\delta\,(\lambda_s/\lambda_D)$ value represents the electrostatic effects related to changes in the EDL structure. The dimensionless effective diffusivity is a function of the porous electrode void fraction as given by equation (3.11). The void fraction of the electrodes used in this work is 0.5; therefore, D^*_{eff} is equal to 0.3089. A typical value of the parameter δ used was 0.5 as it ensured stable behavior of the numerical procedure. The goal was to determine if the effective diffusivity changed with temperature as given by equation (3.13).

The uptake curve at 313 K (40°C) was arbitrarily selected to match the experimental data. Repeated runs of the simulation based on the transport model showed that the values of A_{eff} determined the quantity of the cumulative salt mass taken by the electrodes, while D^*_{eff} and δ determined the slope of the cumulative mass vs time curve. A typical simulation was started with the standard values of $D^*_{eff} = 0.3$ and $\delta = 0.5$. Then, different values of A_{eff} were assigned until matching was achieved. The same values of parameters D^*_{eff}, δ, and A_{eff} were used to match the experimental curve measured at another temperature. In case this was not possible for the second curve, D^*_{eff} was varied until a good matching was achieved. Matching of the second curve with the same set of parameters would imply that D^*_{eff} varies according to equation (3.13) and that only

temperature influences the transport process. If matching with the same set of parameter values was not obtained, it implies that the variation in temperature produces more complex changes in the electrosorption process.

Figure 3.9 shows that the cumulative salt mass taken by the electrodes increased fast at short times, due to the high initial salt adsorption on the electrode surface. This process was accompanied by a sharp decrease in the salt concentration inside the electrode pores. At medium and long times, absorption saturation was reached and the salt concentration inside the pores increased continuously due to diffusion from the solution outside the electrodes.

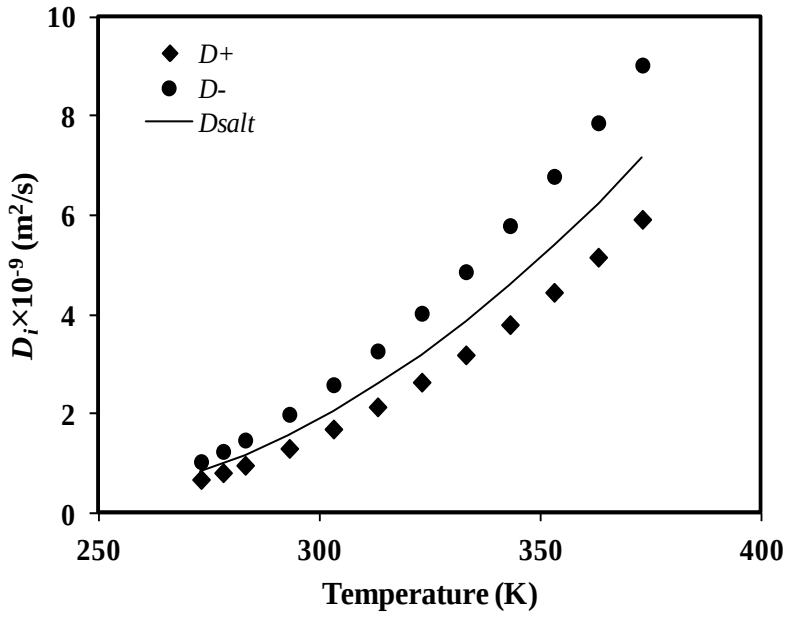

Figure 3.8 Temperature variation of the salt diffusion coefficient as proposed by Neumann and Thomas-Alyea (Newman and Thomas-Alyea, 2004a).

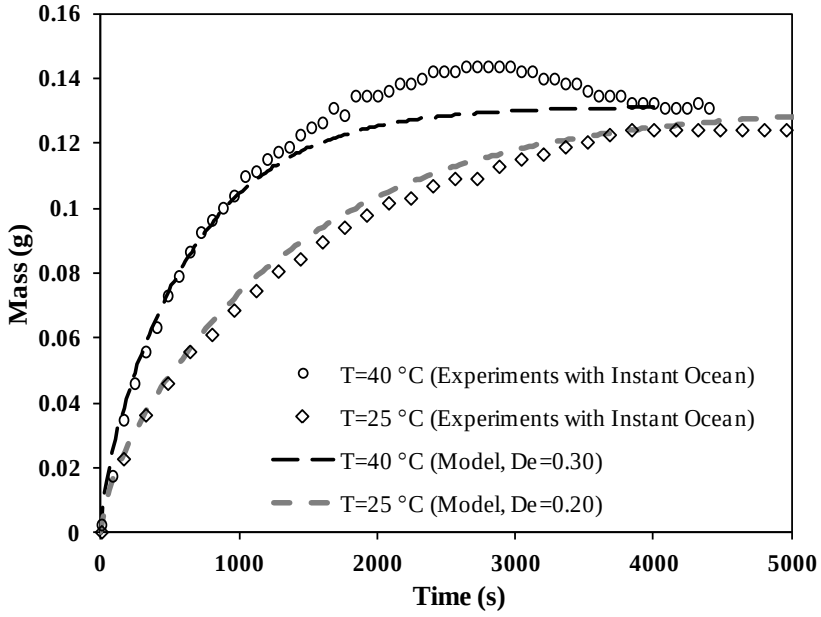

Figure 3.9 Comparison of transport modeling results and experimental data for Instant Ocean solution. Modeling curves have same δ =0.5 (ratio of effective thickness of the Stern layer over the Debye screening length) and A_{eff} = 2.8E7 m^2/m^3 (porous medium effective area), but different D^*_{eff} ($D^*_{eff} = D_{eff}/D$).

This process was first described by Biesheuvel and Bazant (Biesheuvel and Bazant, 2010). Experimental evidence is provided by electric current measurements (Figure 3.7).

A good agreement for both curves at different temperatures using the same set of parameters could not be obtained. However, a fair agreement was found for slightly different D_{eff} values. This result suggests that there is a transport effect that leads to unsatisfactory fitting of the curves at both temperatures. The different D_{eff} values also imply that the difference in cumulative salt mass values cannot be explained only on the basis of the temperature difference.

3.3.4.2 Influence of Temperature on Ion Transport in the Pores for Sodium Chloride Solution

Cumulative salt mass trapped in the electrodes vs time obtained from the experimental data for NaCl solution is depicted in Figure 3.10. The same procedure as described in the previous section was used to describe the data, and the same qualitative behavior was observed. However, in this case curve matching was obtained using different δ values. These results suggest that the difference in cumulative salt mass cannot be explained based only on transport effects, and there is an electrostatic (charge) effect related to changes in the EDL structure, which produces the different results.

In both cases, higher values of cumulative mass were observed at higher temperatures. The different behavior observed with the Instant Ocean and NaCl solutions can be due to competition among ions of different valence and diameter. At short times, lighter monovalent ions are adsorbed faster on the electrodes than heavier divalent ones. However, at medium and long times the higher-charge ions displace the monovalent ions due to stronger electrostatic forces. This effect can occur only for the Instant Ocean solution.

3.4 Conclusions

This study is focused on the influence of temperature on the electrosorption of ions in the CDI process. Higher sorption and regeneration rates were observed at higher temperatures. A comparison of the electrosorption experiments with sodium chloride and Instant Ocean solutions revealed competition effects between ions of different size and valence. The cumulative salt mass adsorbed predicted by the transport model can be

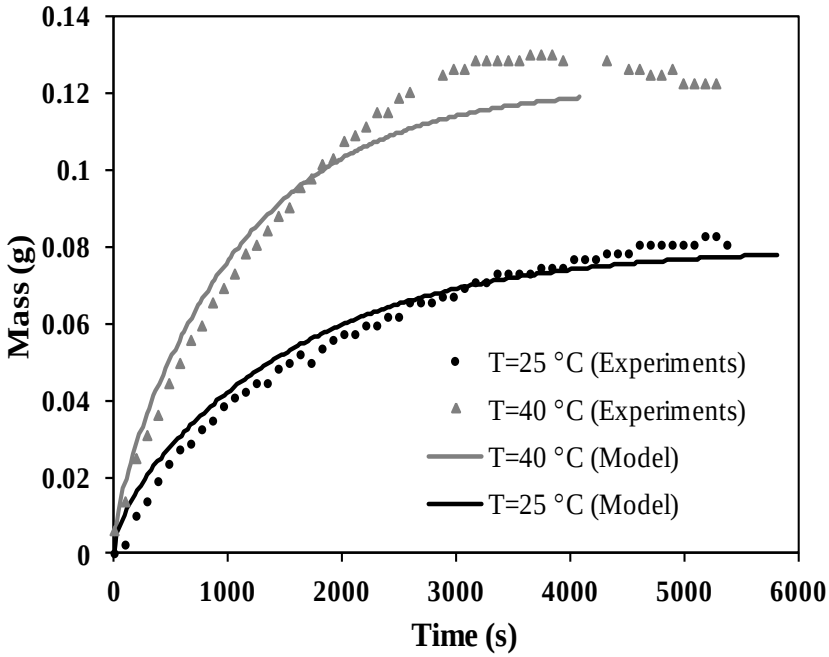

Figure 3.10 Comparison of simulation results and experimental data for NaCl solutions. The porous media parameters (A_{eff}=2.5E7 m^2/m^3, D^*_{eff} =0.15) are the same for the two temperatures, while δ=0.5 for T=40°C and δ=0.75 for T=25°C. Modeling results describe the experimental data at 25°C and 40°C reasonably well.

matched with the experimental data for both Instant Ocean and sodium chloride solution, even though different mechanisms are involved. The results of this study have significant implications in the development of efficient technologies for processing not only produced water generated by the oil and gas industries, but also other types of saline water and wastewater. Regulation of the ion electrosorption rate from a saline solution containing a mixture of ions can be achieved by adjusting the temperature of the solution.

CHAPTER 4

NEUTRON IMAGING OF GADOLINIUM ION TRANSPORT IN MESOPOROUS CARBON MATERIALS

Neutron imaging is presented as a tool for quantifying the diffusion of ions inside porous materials, such as carbon electrodes used in the desalination process *via* capacitive deionization (CDI) and in electrochemical energy-storage devices. Monolithic mesoporous carbon electrodes of ~10 nm pore size were synthesized based on a soft-template method. The electrodes were used with an aqueous solution of gadolinium nitrate in an electrochemical flow-through cell designed for neutron imaging studies. Sequences of neutron images were obtained under various conditions of applied potential between the electrodes. The images revealed information on the direction and magnitude of ion transport within the electrodes. From the time-dependent concentration profiles inside the electrodes, the average value of the effective diffusion coefficient for gadolinium ions was estimated to be $2.09 \pm 0.17 \times 10^{-11}$ m^2 s^{-1}at 0 V and $1.42 \pm 0.06 \times 10^{-10}$ m^2 s^{-1} at 1.2 V. The values of the effective diffusion coefficient obtained from neutron imaging experiments can be used to evaluate model predictions of the ion transport rate in CDI and electrochemical energy-storage devices.

4.1 Introduction

Electrosorption is the phenomenon in which ions in an aqueous solution are forced towards the electrodes through the application of an electrical potential. Ions are held in the electrical double layer (EDL) near the surface of the electrodes. Electrosorption has applications in energy storage (Conway, 1999; Conway et al., 1997; Frackowiak and Béguin, 2001; Simon and Gogotsi, 2008) and water purification (Gabelich et al., 2002; Hou et al., 2006; Oren, 2008; Yang et al., 2001; Ying et al., 2002; Zou et al., 2008a). A supercapacitor or EDL capacitor stores energy at the electrode-electrolyte interface. Supercapacitors have good reversibility, high power density, and a low internal resistance (Simon and Gogotsi, 2008). Electrosorption of ions by electrodes of high surface area is also employed in capacitive deionization (CDI), an electrochemical method for water purification. CDI involves application of an electrical potential between electrode pairs submerged in brackish or seawater, effectively "trapping" the ions in the EDL at the solid-liquid interface, resulting in a reduction of the bulk ion concentration. CDI has several potential advantages over other desalination methods such as ease of regeneration by removing the applied potential, reduction of secondary wastes, operation at low voltages, and simple operation since membranes or chemicals are not involved. Attempts towards commercial application of CDI and its advantages over other water purification methods have been discussed in recent review articles (Anderson et al., 2010; Oren, 2008). Carbon aerogel (Gabelich et al., 2002; Hou et al., 2006; Xu et al., 2008; Yang et al., 2001; Ying et al., 2002), mesoporous carbon (Li et al., 2009; Tsouris et al., 2011; Zou et al., 2008a), graphene (Li et al., 2010a, b), carbon nanotubes (Chen et al., 2010; Gao et al., 2009; Pan et al., 2009; Wang et al., 2006), and

carbon electrodes coupled with ion-exchange membranes (Biesheuvel and van der Wal, 2010; Biesheuvel et al., 2011) have been investigated for application in the electrosorption of ions for water treatment. Porous carbon materials exhibit high electrical conductivity and high surface areas, resulting in materials that are suitable as CDI electrodes. This study presents neutron imaging as a technique to quantify the transport of ions inside mesoporous carbon electrodes used for desalination and energy storage applications.

Neutron scattering techniques are analogous to X-ray scattering, except that, while X-rays probe the electron clouds around the atoms, neutrons probe the atomic nuclei. This feature provides several advantages for imaging over X-rays, electrons, and visible light, as neutrons are highly penetrating. Neutron imaging is a non-destructive technique with applications in a wide range of disciplines including engineering, materials science, paleontology, soil physics, and others. It can be used as a complementary technique to the conventional X-ray radiography due to the different sensitivities of the two methods (Deschler-Erb et al., 2004). In particular, neutron imaging has been applied to visualize water in fuel cells with the aim to improve the performance of fuel cells (Aaron et al., 2011; Bellows et al., 1999; Boillat et al., 2008; Mukundan and Borup, 2009; Park et al., 2008; Pekula et al., 2005; Satija et al., 2004; Tang et al., 2010; Turhan et al., 2006). Neutron imaging has also been used to quantify lithium concentration in electrodes in lithium batteries (Goers et al., 2004; Kamata et al., 1997; Lanz et al., 2001; Nanda et al., 2012; Siegel et al., 2011a). In addition, neutron imaging has been utilized to investigate plant-soil interactions (Menon et al., 2007; Oswald et al., 2008), archaeological specimens (Jacobson et al., 2011; Van Langh et al.,

2009), and in the fields of biology and medicine (Adani and Fallone, 2000) for noninvasive studies of various materials of interest. Study of ion transport phenomena in porous carbon materials by neutron imaging provides an avenue for improvement in electrode materials employed in CDI and supercapacitors.

4.2 Materials and Methods

4.2.1 Capacitive Deionization Cell for Neutron Imaging

A specially designed flow-through CDI cell for neutron imaging was constructed as shown in the inset of Figure 4.1. The solution was allowed to circulate from a beaker through the cell, while ions were taken up by the carbon electrodes via electrosorption.

4.2.2 Materials Synthesis and Characterization

The electrodes used in neutron imaging were composed of monolithic, mesoporous carbon synthesized via a previously reported procedure at the Oak Ridge National Laboratory (ORNL). The method of synthesis results in a mesoporous carbon material with high porosity. Phloroglucinol was dissolved in ethanol (200 Proof, Decon Labs, Inc.) with the structure-directing template Pluronic F127 (BASF), hydrochloric acid (3M, Fisher Scientific), and glyoxal (40 wt. % aq., Sigma Aldrich). The resulting phenolic carbon polymer was isolated from the solvent after phase separation and dried at 80°C. The agglomerated and partially fused material was then broken up into a powder form by shredding the clumps in a blender in small 50-g portions for 1 to 2 minutes. The material was subsequently sieved to 40 mesh, and the fraction that was not broken up was processed for an additional 1 to 2 minutes. Portions of the sieved material were mixed with Toho Tenax 344 milled carbon fiber to produce a blend that is 20 wt% carbon fiber.

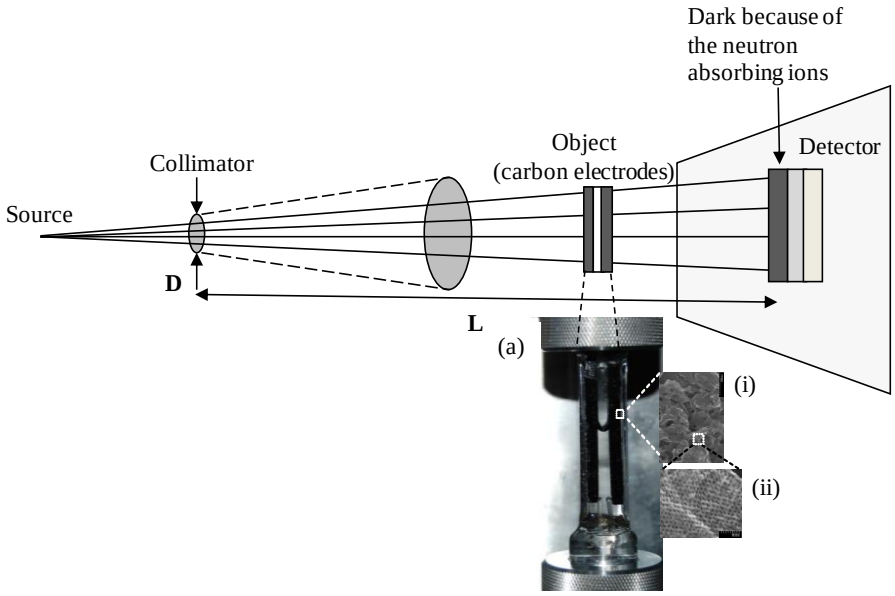

Figure 4.1 Neutron imaging basic setup: inset (a) shows a picture of the flow-through cell with the electrodes constructed of ORNL mesoporous carbon. (i) STEM (Scanning Transmission Electron Microscopy) image of mesoporous carbon and (ii) high-resolution STEM image of the mesopores in the carbon matrix are also shown.

Portions of the polymer-carbon-fiber blend material were pressed into 7.6-cm diameter discs at 68 and 136 atm to a final thickness of ~3.8-mm thick. The discs were carbonized at 1123 K at 2 K/min under a nitrogen atmosphere. The carbonized discs were machined into rectangular bars for the test apparatus. A 0.76-mm hole was then drilled into the end of each bar to a depth of over 10 mm. A platinum wire was pressed into the end of each electrode bar for electrical connection and glued at the tip of the electrode.

Surface area measurements were performed with a Micromeritics Tristar 3000 at 77 K with nitrogen as the adsorbate. Cyclic voltammetry (CV) experiments for electrochemical characterization were conducted on the samples from which the carbon electrodes for the imaging experiments were constructed. CV experiments were performed with a Bioanalytical Systems (BAS) (West Lafayette, IN) voltammetric analyzer (CV-50W Version 2), which was connected with a BAS C2 cell stand. The BAS Model RE-1 (Ag/AgCl electrode in a 3 M NaCl electrolyte solution) was used as the reference electrode. The experiments were conducted with 0.1 M NaCl solution at room temperature (25°C) at a scan rate of 1 mV/s.

4.2.3 Neutron Imaging Principle

The High Flux Isotope Reactor (HFIR) CG-1D neutron imaging beamline at ORNL was used in this study (Bilheux et al., 2013). Neutron imaging is based on the principle that radiation passing through matter is attenuated depending on the properties and structure of the material. In neutron imaging, a camera captures the attenuation of a neutron beam passing through a sample (Figure 4.1). A two-dimensional projection of the sample on the detector plane is collected by the detector. The detection system consists of a neutron sensitive LiF/ZnS scintillator screen, which converts the neutrons to visible

light. The pixelated image is then captured by the charge coupled device (CCD) camera. The L/D ratio contributes to the image spatial resolution, where D is the diameter of the inlet aperture or pinhole and L is the distance from the aperture to the detector plane.

The attenuation of beam caused by a uniformly thick, homogeneous sample is given by the Beer-Lambert equation:

$$I = I_o e^{-\mu\delta} \tag{4.1}$$

where μ is the linear attenuation coefficient given by:

$$\mu = \sigma \frac{\rho N_A}{M} \tag{4.2}$$

I is the intensity of neutron beam after attenuation, I_o is the intensity of the incident beam, δ is the thickness of the sample, σ is the material-specific total cross section for neutrons, ρ is the material density, N_A is the Avogadro number, and M is the molar mass.

For a real sample consisting of several components, the total neutron attenuation can be calculated as the summation of attenuation due to each component weighted with the molar concentration of that material. For the cell used in the present study, the total attenuation at a point can be written as the sum of two components, one that is constant and another that changes over time (attenuation due to gadolinium ions):

$$I(t) = I_o \exp(-\sigma_{Gd} c_{Gd}(t) N_A \delta - \sum_{i, i \neq Gd} \sigma_i c_i N_A \delta) \tag{4.3}$$

where $I(t)$ is the intensity of neutron beam after attenuation at time t, and c is the molar concentration. Changes in the neutron beam intensity as a function of position, measured by the CCD camera, depend on variations of gadolinium concentration vs position and time.

The optical density (denoted by OD), which is the negative logarithm of the ratio of two measurements of neutron intensity taken at times t_1 and t_2, is directly proportional to changes in gadolinium ion concentration (Siegel et al., 2011b). It should be noted that the cell creates an offset in neutron transmission, while the solution does not attenuate enough to create any significant change in neutron transmission.

$$OD = -\ln(I(t_2)/I(t_1)) = \sigma_{Gd} N_A \delta \ (c_{Gd}(t_2) - c_{Gd}(t_1)) \propto \Delta c_{Gd} \tag{4.4}$$

$$\Delta c_{Gd} = \frac{-\ln(I(t_2)/I(t_1))}{\sigma_{Gd} N_A \delta} \tag{4.5}$$

4.2.4 Neutron Imaging Experiments

The experimental setup for neutron imaging is shown in Figure 4.1. The inset (a) in the figure is a picture of the electrochemical flow-through cell containing the mesoporous carbon electrodes. Upward flow of the electrolyte solution through the cell was provided through Teflon tubing by a gear pump. A flowrate of 30 mL/min was typically used in the experiments. Vertical glass fibers below the carbon electrodes were used to maintain electrical separation of the electrodes. The electrodes in the cell were connected to a power supply (HP 3632A; Hewlett Packard, CO) through the platinum wire leads, so that the applied potential could be remotely adjusted away from the beam. The cell was placed in the neutron beam with the electrodes aligned in the direction of the beam, and the CCD camera captured the intensity of the attenuated neutron beam after passing through the cell.

A 100-mL volume of 3000 ppm solution of gadolinium (III) nitrate [Gd $(NO_3)_3$] in D_2O was continuously recycled through the cell throughout the experiment at room

temperature (25°C). Gadolinium ions were used because of their large cross section for neutron absorption; however, other ions, such as lithium or hydrogen-containing ions can also be used. Deuterium oxide was used instead of normal water to increase the imaging contrast for gadolinium ions since deuterium has a much smaller cross section for neutron capture than hydrogen. The first set of experiments was carried out without voltage applied to provide a baseline attenuation of an image with no electrosorption. In the subsequent experiments, a DC voltage of 1.2 V was applied between the two electrodes to observe the influence of the electrical potential. For all the experiments, images were captured at a time interval of 5 minutes. The concentration of the solution in the space between the electrodes was assumed constant at 3000 ppm (0.00874 M) throughout the experiment. This assumption did not affect the results because the solution attenuation did not change with time.

4.2.5 Image Analysis

The image analysis was carried out by using ImageJ (Rasband et al., 1997-2011) software developed at the National Institutes of Health. The intensity values were obtained at various points of the images. The transmission value (I/I_o) was calculated by dividing the intensity values measured at each pixel of the image by the incident beam intensity at each pixel.

Since gadolinium ions absorb neutrons, a higher quantity of gadolinium ions at a point on the electrode would result in a lower transmission value. The initial value of attenuation in the electrodes corresponds to essentially zero concentration of gadolinium. The change in the intensity (decrease in transmission) at various points within the electrodes, as the experiment progresses, is due to changes in gadolinium concentration

due to diffusion of ions inside the electrodes (by assuming that the other cell components are not changing or moving). The ratio of measurements of neutron intensity, taken at times t_1 and t_2, is directly proportional to the change in gadolinium ion concentration (for constant neutron path length through the different components of the cell). The increase in the concentration of gadolinium ions in the negative electrode was obtained from equation (4.5).

4.3 Results and Discussion

4.3.1 Materials Characterization

Nitrogen sorption isotherms and BJH pore size distributions for mesoporous carbon are shown in Figure 4.2. The type H2 hysteresis observed is indicative of large and uniform mesopores, consistent with cylindrical shape, as expected based on the utilization of soft-templating to produce the carbon material (Kruk and Jaroniec, 2001). The extension of the hysteresis to lower relative pressures indicates constrictions in some of the pores. The BET surface area of the mesoporous carbon was calculated to be 633 m^2/g with the BJH average pore diameter centered at 10 nm. The total pore volume calculated at $P/P_o = 0.995$ is 0.626 cm^3. CV characterization was performed to compare different carbon materials and select one with an appropriate rate of ion uptake for neutron imaging experiments.

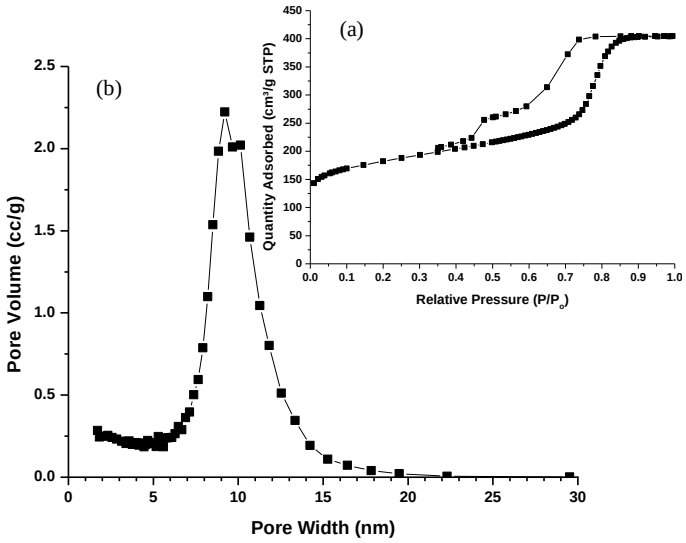

Figure 4.2 (a) Nitrogen adsorption isotherms and (b) BJH pore-size distributions for the mesoporous carbon used in neutron imaging experiments.

The specific capacitance was calculated by dividing the current by scan rate and weight of the carbon sample:

$$C = \frac{I}{\left(dV/dt\right) * m} \tag{4.6}$$

where C is the specific capacitance in (F/g), I is the current measurement, dV/dt is the potential scan rate, and m is the mass of the carbon sample. The CV results demonstrate that the rate of electrosorption and the specific capacitance increase when the pressure used to make the samples decreases (Figure 4.3). Samples of mesoporous carbon discs prepared at 68 atm were selected for the preparation of electrodes for use in the neutron imaging experiments. For a specific capacitance value of 50 F/g corresponding to the materials prepared at 68 atm, which had a surface area of 633 m^2/g, the normalized

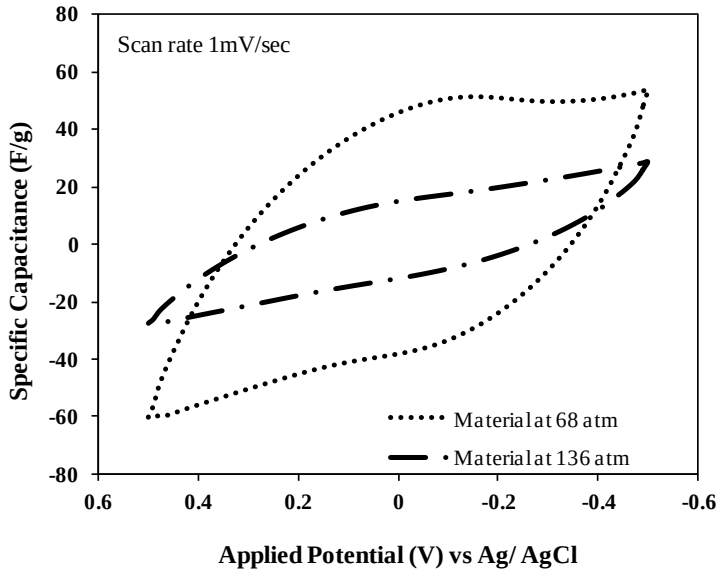

Figure 4.3 Influence of pressure used while synthesizing carbon samples from mesoporous carbon powder: A higher electrosorption rate and a higher capacitance are observed when the pressure used to synthesize samples decreases from 136 atm to 68 atm.

capacitance was 0.08 F/m^2. The CV patterns are slightly distorted because of differences in the transport rates of the cations and anions. It appears that the cation diffusion is slightly higher than that of the anion. Materials generated under pressures lower than 68 atm may also be appropriate for imaging experiments, as long as the ion diffusion time from one end of the electrode to the other is much greater than the time needed to construct one neutron image, which in this case is five minutes.

4.3.2 Image Sequences

A series of images obtained with no potential applied is presented in Figure 4.4(a). In the first image of the series, the cell contained pure D_2O without ions. In subsequent images of the same series, the solution contained 3000-ppm gadolinium (III)

nitrate in D_2O. With no voltage applied, cations diffused mostly onto the periphery of both electrodes during the two-hour period of the experiment. In Figure 4.4(b), a DC voltage of 1.2 V was applied between the two electrodes. Under the influence of electrical potential, gadolinium cations migrated into the pores throughout the negative electrode. It is assumed that nitrate ions migrated to the positive electrode to balance charges. From a qualitative comparison of the two time-series of images, it was found that the application of an electrical potential increased the ion adsorption capacity and the uptake rate, as counterions in the solution were adsorbed by the oppositely charged electrodes to balance the applied potential. This phenomenon is a result of the higher surface charge when an electrical potential is applied. Counterions are attracted by the electrodes to neutralize the surface charge, thus the electrosorption capacity increases with increasing the applied potential. As the capacity increases, the driving force for electrosorption also increases leading to faster ion uptake rates. The change in the bulk concentration of gadolinium ions depends on the transmission value at that point (equation 4.4). Thus, the amount of gadolinium ions adsorbed as a function of time can be estimated from the images.

Figure 4.5 presents the transmission of neutrons at various heights along the entire width of the two electrodes corresponding to the series of images in Figure 4.4. From the transmission plots at the height 21 mm above the reference level, it can be inferred that, when gadolinium nitrate solution was added in the cell, gadolinium ions were adsorbed by the carbon electrodes (0-V series). Adsorption of gadolinium ions by the mesoporous carbon results in lower transmission values in the electrode region of the images.

Application of a DC voltage of 1.2 V resulted in further penetration of gadolinium

ions by electrostatic attraction. The plots for gadolinium 1.2-V series illustrate that lower transmission values for the left electrode can be attributed to the application of the electrical potential, which results in greater penetration of gadolinium ions inside the pores of the electrode. Specifically the average transmission value through the left electrode when 1.2 V potential had been applied for 105 minutes was about 24.7% lower than the transmission value in the case no potential was applied (corresponding to an OD of 0.284). The total amount of gadolinium adsorbed by the left electrode after 1.2 V had

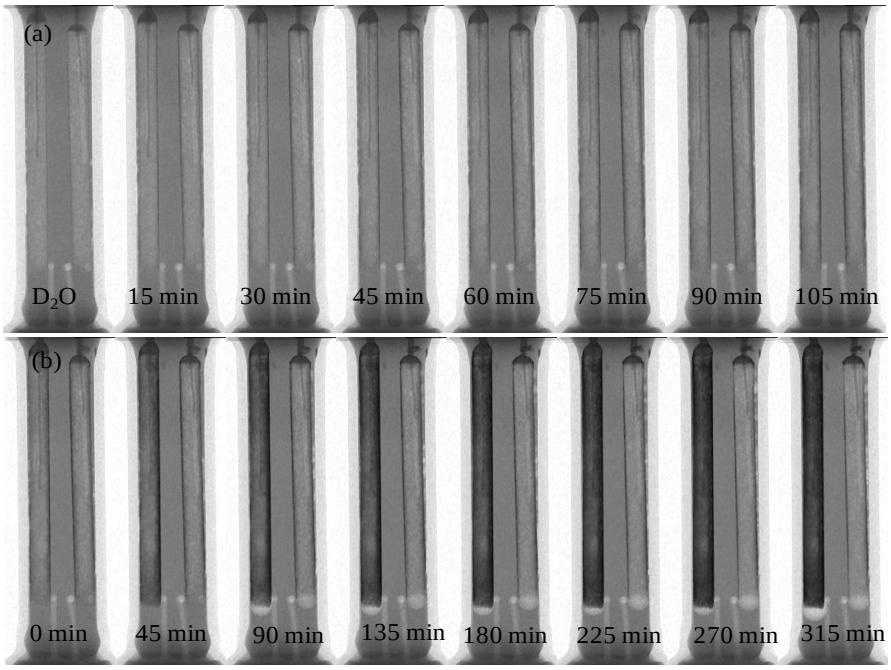

Figure 4.4 Time sequences of neutron images for (a) no potential applied and (b) 1.2-V DC potential applied. In (b), the left electrode is negatively charged.

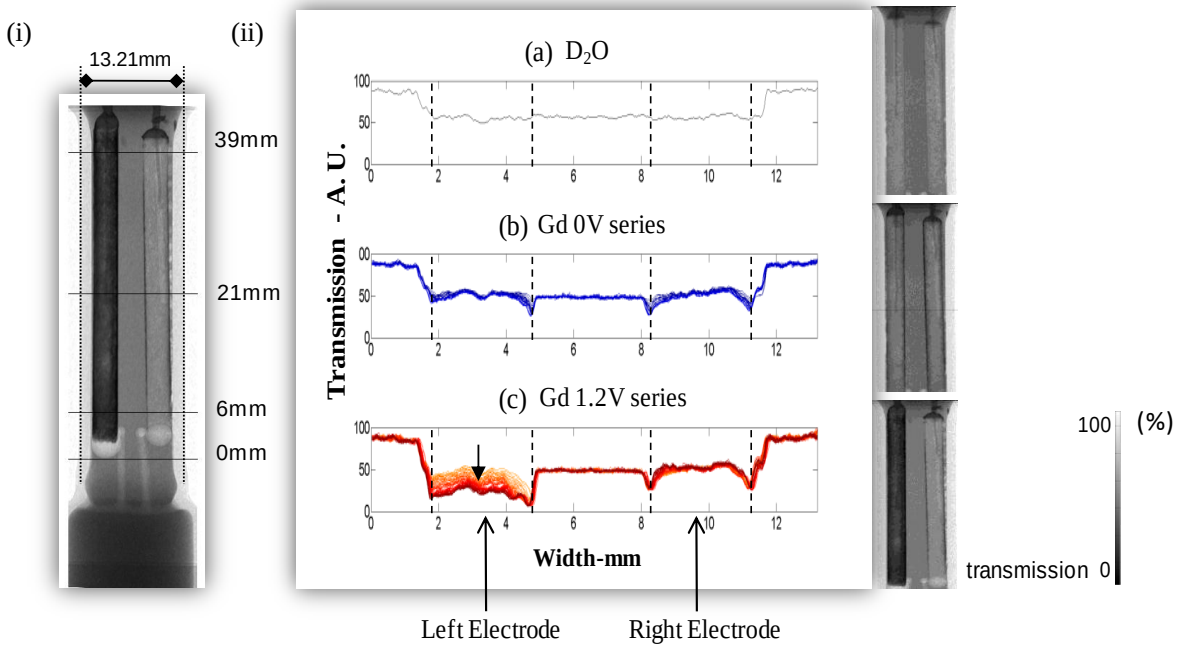

Figure 4.5 (i) Representative image of the set of electrodes showing the height levels chosen for analysis (ii) Transmission of neutron beam at various points across the width of the left electrode (at height 21 mm above the reference level denoted as 0 mm) for three conditions: (a) cell filled with only D_2O solution, (b) cell filled with gadolinium nitrate solution, and (c) cell filled with gadolinium nitrate and negative potential applied to the left electrode for 240 minutes. The arrow in the left electrode region on the graph for 1.2-V applied indicates the decrease in transmission value with the progression of time.

been applied for 340 minutes was estimated at 1 mg of Gd in a volume of 0.6 cm^3 of the electrode.

Figure 4.6 (a) presents a series of images obtained from a second set of mesoporous carbon electrodes with 3000 ppm gadolinium (III) nitrate solution in D_2O. The first image at time t = 0 minutes was taken after a DC potential of 1.2 V had been applied between the two electrodes for about 6 hours. The electrode on the right was negatively charged; therefore, gadolinium ions accumulated within this electrode, while

nitrate ions (not visible in neutron imaging) accumulated in the left electrode to counter balance the charge. After the first image was obtained, the external DC potential was removed and the two electrodes were shorted. It was observed that the left electrode initially became darker as some of the gadolinium ions migrated into the left electrode after the removal of the potential. Figure 4.6 (b) illustrates the transport of Gd ions by presenting the decrease in the average transmission value across the width of the left electrode after the DC potential was removed [corresponding to images in Figure 4.6 (a)].(Bevington, 1969) The average transmission value across the left electrode decreased by 18.4% (at t=250 minutes) from the value at t=0 minutes when the potential was removed (corresponding to an OD of 0.203). The decrease in transmission corresponds to an increase in gadolinium ion concentration on the left electrode. The transmission in the region between the electrodes did not change significantly, as the solution was being circulated continuously through the cell from a relatively large reservoir.

The observations in Figure 4.6 may be described in terms of transport properties of ions. When a potential is applied between the electrodes, counterions from the solution diffuse into the pores to counterbalance the surface charge. Trivalent gadolinium ions move into the negatively charged electrode and monovalent nitrate ions move into the positively charged electrode. After equilibrium has been established, as soon as the applied potential is removed, there is an excess positive charge in the pores of the first electrode and an excess negative charge in the pores of the other electrode due to the presence of gadolinium and nitrate ions, respectively. This charge accumulation needs neutralization that can happen by ion diffusion from the pores back to the solution and counterion diffusion from the solution to the pores.

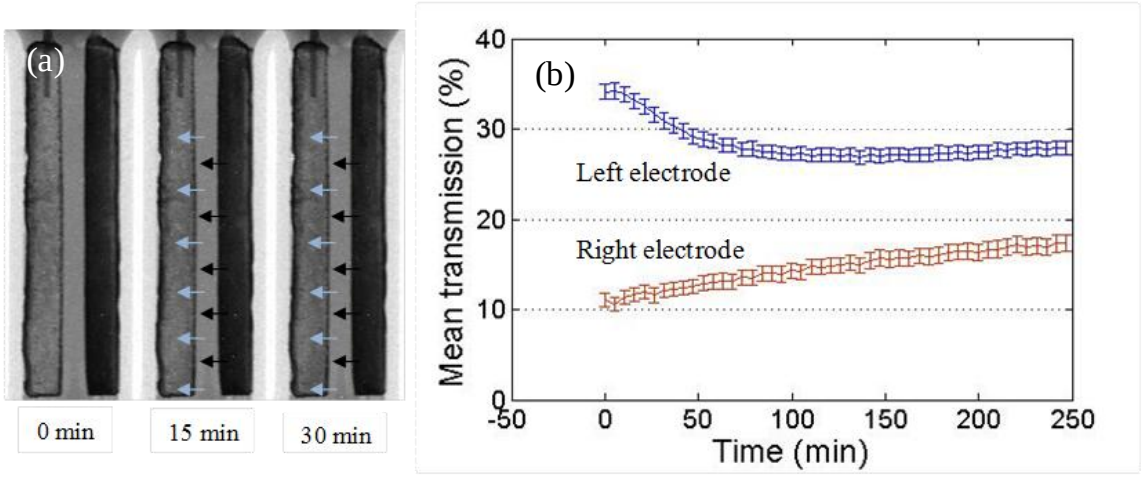

Figure 4.6 (a) Time sequence of neutron images after 1.2 V DC potential was removed and the electrodes were shorted at t = 0 min. As expected, gadolinium ions were released from the right electrode to the recycled solution between the electrodes (dark arrows). However, gadolinium ions were also taken up from the solution by the left electrode (light arrows). The left electrode became darker as the gadolinium ions moved towards the left electrode to balance the charge. (b) Average transmission of the neutron beam across the left and the right electrodes, after the DC voltage was removed. The transmission through the right electrode, which is initially loaded with gadolinium, increased due to the loss of gadolinium ions. The transmission through the left electrode decreased considerably in the beginning before starting to increase, indicating initial transport of gadolinium ions to the left electrode.

The experimental results shown in Figure 4.6 demonstrate that, initially, counterions diffuse from the solution into the pores to neutralize the surface charge. It can be observed that after about 100 minutes, the left electrode stopped adsorbing Gd ions and, from that time on, both electrodes appeared to lose Gd ions.

Another experiment was conducted with a different set of electrodes to examine the effect of reversing the polarity on the transport characteristics of ions. After the gadolinium ions had been loaded onto the left electrode, the polarity of the applied voltage was reversed from +1.2 V to -1.2 V. The combined transport of Gd ions out of the left electrode and from the solution into the right electrode was faster than the transport of Gd ions when a voltage change from 0 V to 1.2 V was applied. This phenomenon is due to a larger overall driving force. When the polarity is reversed, two factors play a role in the transport of ions: electrical potential and concentration gradient between the two electrodes due to which a relatively faster migration of gadolinium ions occurs.

4.3.3 Measurements

The equation for Fick's second law of diffusion was considered:

$$\frac{\partial C}{\partial t} = D_{eff} \frac{\partial^2 C}{\partial x^2} \tag{4.7}$$

with the following boundary conditions for the negative electrode in the system:

$C = C_1, \quad x = 0, \quad t \geq 0,$

$C = C_2, \quad x = l, \quad t \geq 0,$

$C = 0, \quad 0 < x < l, \quad t = 0.$

The electrode on the left is the negative electrode in our system. An analytical solution is obtained in this case (Crank, 1979):

$$C = C_1 + (C_2 - C_1)\frac{x}{l} + \frac{2}{\pi}\sum_1^{\infty}\frac{C_2\cos n\pi - C_1}{n}\sin\frac{n\pi x}{l}\exp\left(-\frac{D_{eff}n^2\pi^2 t}{l^2}\right) \tag{4.8}$$

where D_{eff} is the effective diffusion coefficient, C is the concentration of ions (defined as the total number of gadolinium ions in a volume of solution or electrode), x is the distance from the right edge of the electrode, t is the time, C_1 is the concentration at the right edge of the left electrode (0.00874 M), C_2 is the concentration at the left edge of the electrode (0.00874 M), and l is the width of the electrode. Since the only unknown in the equation (4.8) is D_{eff}, the value of the diffusion coefficient can be obtained by matching the experimental data with calculated concentration histories. The value of the diffusion coefficient was obtained through this optimization process using the MATLAB(Matlab Users Guide et al., 1998) Optimization toolbox.

When a potential of 1.2 V was applied between the two electrodes, the solution given by equation (4.8) was used to estimate the value of the effective diffusion coefficient. It should be noted that the solution of Fick's diffusion law was adopted here mainly for the purpose of comparison of ion transport rates in the cases of 0 V and 1.2 V applied potential. The Nernst-Planck equation extends the Fick's law of diffusion to the case where two factors, electrical potential and concentration gradient, drive the transport of ions. The solution of Nernst-Planck equation would account for the migration of ions due to the application of the electric field; however, the solution of the Nernst-Planck equation for an asymmetric electrolyte, such as the trivalent gadolinium ions and monovalent nitrate ions, is beyond the scope for the present analysis. Recent studies have been focused on the solution of the Poisson-Nernst-Planck equation for symmetric and

asymmetric electrolytes (Biesheuvel et al., 2012; Golovnev and Trimper, 2009), but the numerical solutions offered cannot be easily adopted here because of the asymmetric electrolyte. Since the influence of the electric field has not been taken into account in the diffusion equation, an increase in the effective diffusion coefficient of ions through the electrodes can reflect the influence of the applied electric potential on the transport of ions in the electrodes.

From the series of images in Figure 4.4, the concentration data were analyzed using equation (4.8) to obtain the values for the effective diffusion coefficient: $2.09\pm0.17 \times 10^{-11}$ m^2/s at 0 V and $1.42\pm0.06 \times 10^{-10}$ m^2/s at 1.2 V. Figure 4.7 shows a comparison of experimental data and modeling results for history of gadolinium concentration with and without applied voltage. The modeling results were obtained by substituting the value of the diffusion coefficient in equation (4.8). Thus, the effective diffusion coefficient obtained in the case of 1.2 V applied potential between the carbon electrodes is approximately 6.8 times higher than the 0-V diffusion coefficient. Previous studies have reported the bulk diffusion coefficient of gadolinium ions at various electrolyte concentrations (Latrous and Oliver, 1992; Rafik et al., 2010). Rafik *et al.* (2010) reported the bulk diffusion coefficient of gadolinium ions in a solution of gadolinium nitrate as 5.71×10^{-10} m^2/s at 0.002 M and 5.81×10^{-10} m^2/s at 0.0002 M. As expected, those values are much higher (about 25 times) than the diffusion coefficient estimated in this study because diffusion in the solution is significantly faster than diffusion in the mesopores of a solid matrix. In principle, the diffusion coefficient should be independent of applied potential; however, because a simple diffusion model was employed that does not consider the effect of the electrical potential, the increase in transport due to the electrical

potential is incorporated in the effective diffusivity. For the experiments in which the polarity of the applied potential was reversed from +1.2 V to -1.2 V, the analysis was done using equation (4.8) to obtain the value of the effective diffusion coefficient of gadolinium ions with a different set of electrodes. The diffusivities were estimated as $8.28\pm0.44 \times 10^{-11} m^2/s$ at 1.2 V, and $2.68\pm0.37 \times 10^{-10}$ m^2/s at 1.2 V applied potential with polarity reversed. Thus, the value of effective diffusion coefficient in the case of reversed polarity is about 3.2 times higher than the value with 1.2 V applied. A higher driving force when the polarity is reversed is reflected in a higher value of diffusion coefficient.

Future experiments with symmetric electrolytes will be conducted to compare the increase in the transport rate, due to the application of electrical potential, with modeling results. In previous studies, the electrochemical impedance spectroscopy (EIS) technique has been utilized for estimating the diffusion coefficient of lithium ions in carboneous materials such as graphite and carbon fibers.(Morita et al., 1993; Takami et al., 1995; Yu et al., 1999) Takami et al. reported the diffusion coefficient of lithium ions to range between 1×10^{-12} to 3×10^{-11} m^2/s in carbon fibers. The diffusion coefficient of gadolinium ions reported here, i.e., $2.09\pm0.17 \times 10^{-11}$ m^2/s at 0 V applied, is within this range. It should be noted, however, that the value of diffusion coefficient depends on the structural properties of the carbon material.

Neutron imaging has thus been demonstrated as a useful technique to observe the transport behavior of ions during electrosorption in efforts to provide a better understanding of the electrolyte transport mechanisms.

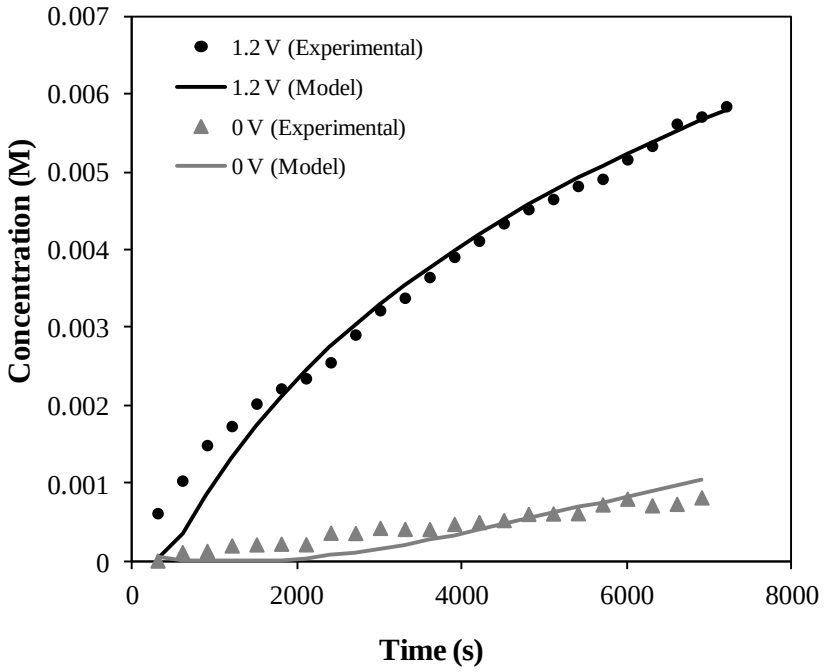

Figure 4.7 Concentration histories of gadolinium ions as a function of time at 0.84 mm from the right end of the electrode for the case of (a) 0 V and (b) 1.2 V applied potential at a height of 20.52 mm above the reference level shown in Figure 4.5.

4.4 Conclusions

This study describes the application of neutron imaging in observing ion transport inside porous carbon electrodes. Images of the mesoporous carbon electrodes acquired over time can yield kinetic information on the transport of ions inside the pores. This technique can be employed to quantify an effective diffusion coefficient of ions through porous materials, and subsequently validate transport models of ions in porous carbon. The value of the effective diffusion coefficient of trivalent gadolinium ions through mesoporous carbon electrodes synthesized in our laboratories has been estimated to be 25 times smaller than the bulk diffusion coefficient. This behavior is a property of the mesoporous carbon used in the experiment and is expected to range widely for different types of carbon materials. When a potential of 1.2 V was applied between the electrodes, the effective diffusion coefficient increased approximately 6.8 times. Furthermore, when the potential was reversed, an even higher rate of diffusion was observed because of a higher driving force. Information about the effective diffusion coefficient under different conditions of applied voltage can be utilized to guide material design in the production of electrodes with enhanced transport properties. In-depth information about the transport characteristics of ions through porous materials can help guide materials design to optimize transport characteristics and cell efficiency.

CHAPTER 5

NEUTRON IMAGING OF LITHIUM IONS IN MESOPOROUS CARBON MATERIALS

Neutron imaging technique has been applied to visualize the transport of lithium ions in mesoporous carbon materials that have applications as electrodes in the capacitive deionization process for water desalination. The experiments were conducted with a flow through capacitive deionization cell designed for neutron imaging and with lithium chloride (^{6}LiCl) as the electrolyte. Sequences of neutron images have been obtained at 1.5 M and 0.5 M concentration of lithium chloride solution. The experiments conducted at high concentration of lithium chloride solution provide an insight into why capacitive deionization is not efficient for desalination of high ionic strength solutions. Furthermore, the effective diffusivity of lithium ions has been estimated by solving Fick's second law of diffusion. The information on ion transport mechanisms can help in better design of the capacitive deionization experiments to improve the process efficiency. The value of effective diffusion coefficient of lithium ions obtained from these experiments can also aid in the design of electrochemical energy storage devices such as lithium-ion batteries.

5.1 Introduction

With the rapid population growth and expanding industrialization, the scarcity of water resources is one of the major challenges of the present time. Apart from better water management practices, we need to rely on energy-efficient methods for water desalination to increase the supply of available water resources. Since approximately 98% of water on earth is in the form of seawater, desalination is a viable option for obtaining fresh water and adding to the current supply. In addition, water produced from gas and oil operations, such as hydraulic fracturing (fracking), needs to be treated for organics and salts removal prior to recycling and reuse. Thus, desalination processes can be used to produce drinking water and treat gas/oil-produced water for recycling/reuse.

The current widely applied desalination technologies are reverse osmosis and thermal desalination. These technologies have some limitations that need to be addressed. Thermal desalination is a high-energy-demand process, while membrane fouling and scaling are severe issues in reverse osmosis of fracking water. Capacitive deionization (CDI), which is based on the electrosorption of ions by charged porous carbon electrodes, has attracted interest as an alternative desalination technology, as it has low-energy requirements (Anderson et al., 2010; Farmer et al., 1997; Farmer et al., 1996; Oren, 2008; Ying et al., 2002). CDI operates at low potentials in the range of 1-1.4 V, and membranes and high-pressure pumps are not required for its operation, so problems of scaling and fouling are avoided. When an electrical potential is applied across porous electrodes, dissolved ions are adsorbed in the electrical double layer (EDL) formed at the electrode-liquid interface. Regeneration of electrodes is carried out by electrically discharging the electrodes, which leads to the release of ions back into the solution. The electrosorption

capacity in this process depends significantly on the physical properties of the electrode material. Porous nanostructured carbon electrodes have been used, as they have a high surface area (400-2000 m^2/g) and low electrical resistivity. Many studies have been carried out with the aim of improving the desalination performance of the CDI process, specifically by synthesizing improved carbon materials for the electrodes. Various carbon materials have been investigated as electrodes for CDI including carbon aerogel (Gabelich et al., 2002; Xu et al., 2008), activated carbon (Ryoo et al., 2003; Zou et al., 2008b), carbon nanotubes (Gao et al., 2009; Wang et al., 2006), graphene (Li et al., 2010a, b), and mesoporous carbon (Li et al., 2009; Tsouris et al., 2011; Zou et al., 2008a).

The salt removal capacity of carbon electrodes in the CDI process depends highly on the pore size and surface area of electrodes. When an electrical potential is applied across the electrodes, ions are adsorbed from solution present in the pores to the surface of the pores and co-ions are expelled from the electrodes. Andelman (2002) suggested that CDI is energy inefficient due to dissolved salt present in the pore volume of the electrodes (Otowa, 1996), and this effect becomes more pronounced at higher electrolyte concentrations. To solve this issue, Andelman (Otowa, 1996) suggested a charge barrier to be placed next to the electrode to compensate for losses associated with ions present in the pores of the electrode. Recently, Lee at al. (2006) developed a membrane capacitive deionization (MCDI) system, in which anion- and cation-exchange membranes were placed onto the external surface of the carbon electrodes (Lee et al., 2006), and reported a 19% higher salt removal efficiency with the MCDI setup compared to the conventional CDI setup. Motivation for the MCDI system came from the fact that regeneration can

occur fast by reversing the polarity of the applied potential. Li et al. (2008) developed a new MCDI device using ion exchange membranes with carbon nanotubes and nanofibers (Shannon et al., 2008), and reported that the removal capacity with MCDI was approximately 50% higher compared to the conventional CDI system. In these studies, it has been demonstrated that the MCDI setup can enhance the desalination efficiency. More recently, Biesheuvel et al. presented a theoretical model for the MCDI process, which describes the time-dependant electric current and effluent ion concentration during the sorption and regeneration phases (Biesheuvel and van der Wal, 2010).

As a desalination method, conventional CDI has not been found to be an energy-efficient method for the treatment of high-salinity solutions when compared to reverse osmosis (Oren, 2008) . Therefore, the process efficiency of CDI needs to be improved in order to become viable for treatment of high salinity solutions. Desalination of high-salinity solutions has relevance in the treatment of seawater and water produced in the hydro-fracking process, as well as other oil/gas operations. In this context, MCDI technology has the potential for being energy efficient for solutions of high ionic strength. In the present work, neutron imaging of lithium-6 ions was conducted to observe the electrosorption and regeneration behavior during CDI at varying electrolyte concentrations. Neutron imaging reveals the ion-transport behavior during the regeneration phase at a high electrolyte concentration, which can aid in making the CDI process more efficient for desalination of seawater or fracking water. Neutron imaging results reveal the reason why desalination of high-salinity solutions by CDI is challenging and point to a solution for more efficient regeneration. Furthermore, we have evaluated the effective diffusivity of lithium ions by employing Fick's second law of diffusion.

5.2 Materials and methods

5.2.1 Capacitive Deionization cell for Neutron Imaging

A specially designed CDI cell, containing mesoporous carbon electrodes in electrolyte solution, was used in the study. The cell was filled up with 70 mL of lithium-6 chloride (^{6}LiCl) solution of 1.5 M concentration, and the experiments were conducted in a batch mode. Lithium-6 isotope was used as it has a high neutron attenuation coefficient of 940.97 barns. Deuterium oxide was used instead of normal water as hydrogen has a high neutron scattering cross section which can inhibit the visualization of the lithium ions in the experiments.

5.2.2 Materials Synthesis and Characterization

The electrodes used in neutron imaging were composed of monolithic, mesoporous carbon synthesized at the Oak Ridge National Laboratory (ORNL), as previously reported (Sharma et al., 2013a). The synthesis method results in a mesoporous carbon material with high porosity. A platinum wire was pressed into the end of each electrode bar for electrical connection and glued at the tip of the electrode. Surface area measurements were performed with a Micromeritics Tristar 3000 at 77 K with nitrogen as the adsorbate.

5.2.3 Neutron Imaging Principle

The experiments were conducted at the CG-1D neutron imaging beamline at the High Flux Isotope Reactor (HFIR) at ORNL (Bilheux et al., 2013). Neutron Imaging is based on the Beer-Lambert law which states that radiation passing through matter is attenuated depending on the thickness and structural properties of the material (Sharma et

al., 2013a). The attenuation of the beam caused by a uniformly thick, homogeneous sample is given by the Beer–Lambert equation:

$$I = I_0 e^{-\mu\delta} \tag{5.1}$$

where I is the intensity of the neutron beam after attenuation, I_0 is the intensity of the incident beam, μ is the attenuation coefficient, and δ is the thickness of the sample.

5.2.4 Neutron Imaging Experiments

The experimental setup for neutron imaging is shown in Figure 5.1. In the experiments conducted in the present study, the specially designed CDI cell was filled up with lithium chloride (^{6}LiCl) solution in deuterium oxide. The electrodes in the cell were connected to a power supply (HP 3632A; Hewlett Packard, CO) through the platinum wire leads, so that the applied potential could be remotely adjusted away from the beam.

5.3 Results and discussion

5.3.1 Materials Characterization

From the characterization studies, the pore surface area of the mesoporous carbon for rectangular and cylindrical electrodes was determined to be 365 m^2/g. Also, the pore volume at $P/P_o = 0.995$ is 0.43 cm^3/g and the average pore size is centered at 15 nm. Nitrogen sorption isotherms and BJH pore size distributions for mesoporous carbon are shown in Figure 5.2.

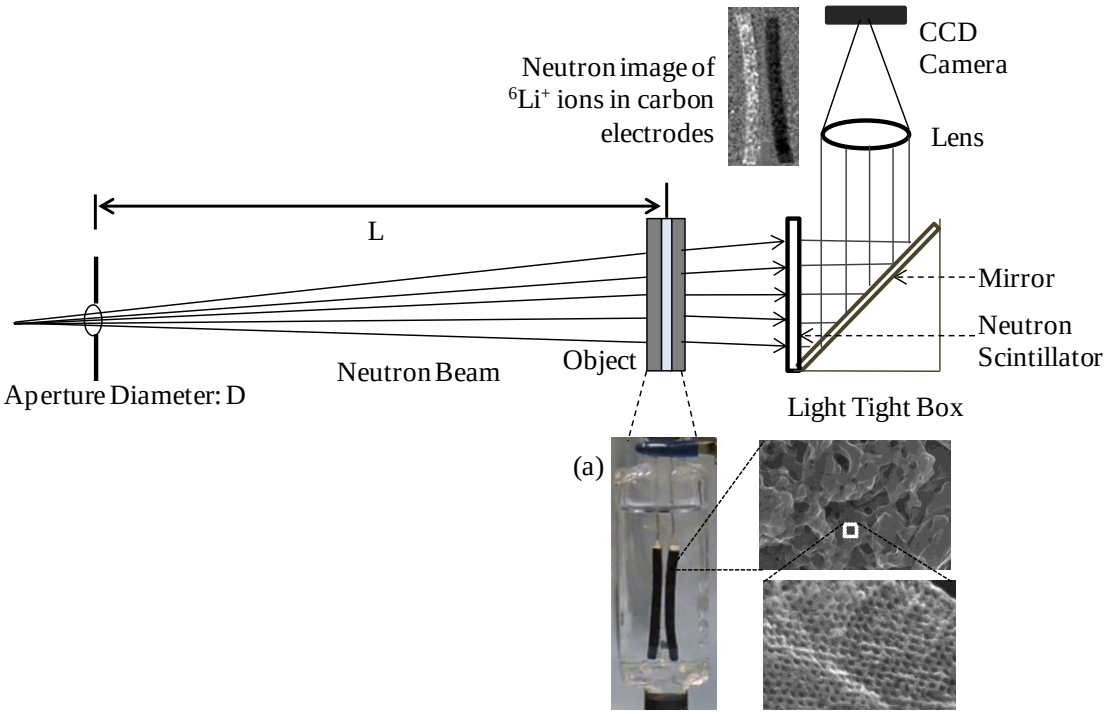

Figure 5.1 The basic experimental setup for neutron imaging consists of a neutron source, a collimator which determines the geometric properties of the beam, neutron scintillator screen, and the sample of study (mesoporous carbon electrodes in the present study). The beam is transmitted through the object and recorded by a neutron scintillator detector. The detector records a 2-dimensional image that is a projection of the sample on the plane. Neutrons are converted to light using scintillator screen, and the light is captured by the CCD camera.

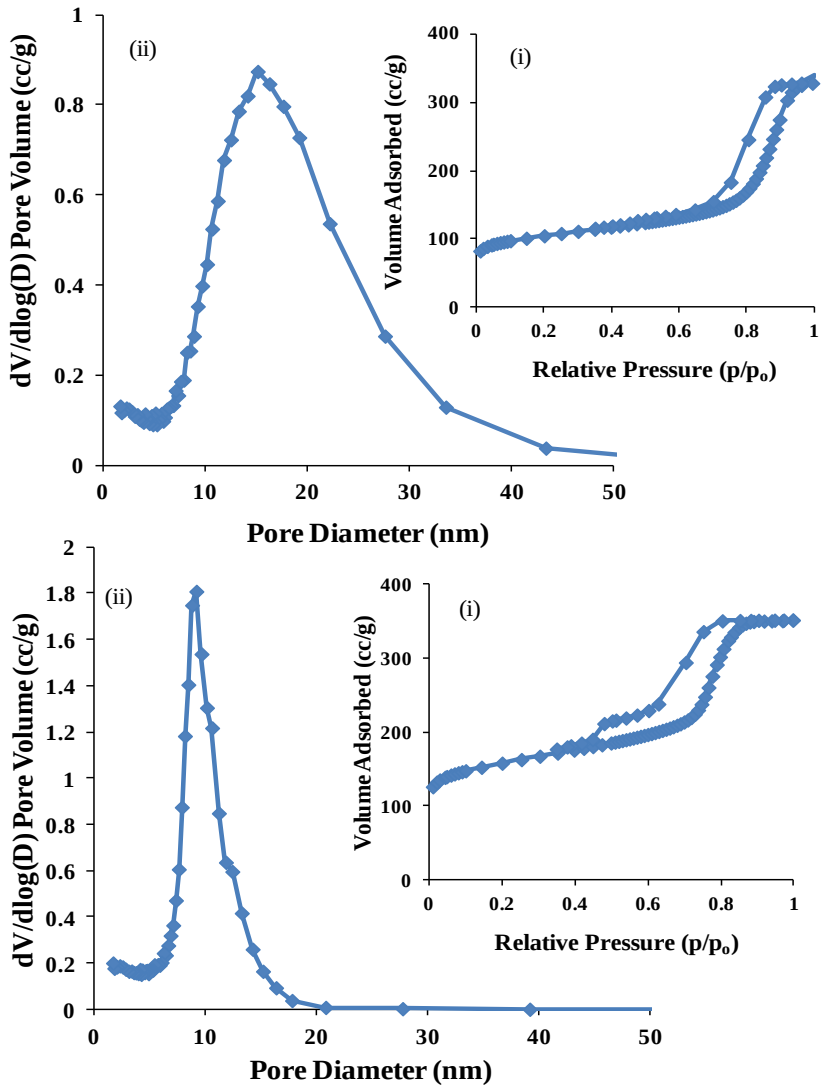

Figure 5.2 (i) Nitrogen adsorption isotherms and (ii) BJH pore-size distributions for the mesoporous carbon used in neutron imaging experiments. The plot (a) corresponds to the rectangular electrodes and (b) corresponds to the cylindrical electrodes. The pore surface area of the mesoporous carbon is 365 m^2/g, and the average pore size is around 15 nm.

5.3.2 Image Sequences

Figure 5.3 represents a series of images from a sorption/regeneration experiment carried out with 1.5 M lithium chloride in D_2O. The images presented are shown as differences from the first image in the series, thus lighter color means less $^6Li^+$ ions and darker color means a higher concentration of $^6Li^+$ ions. Images in Series (a) were obtained during electrosorption, while images in series (b) were obtained during regeneration.

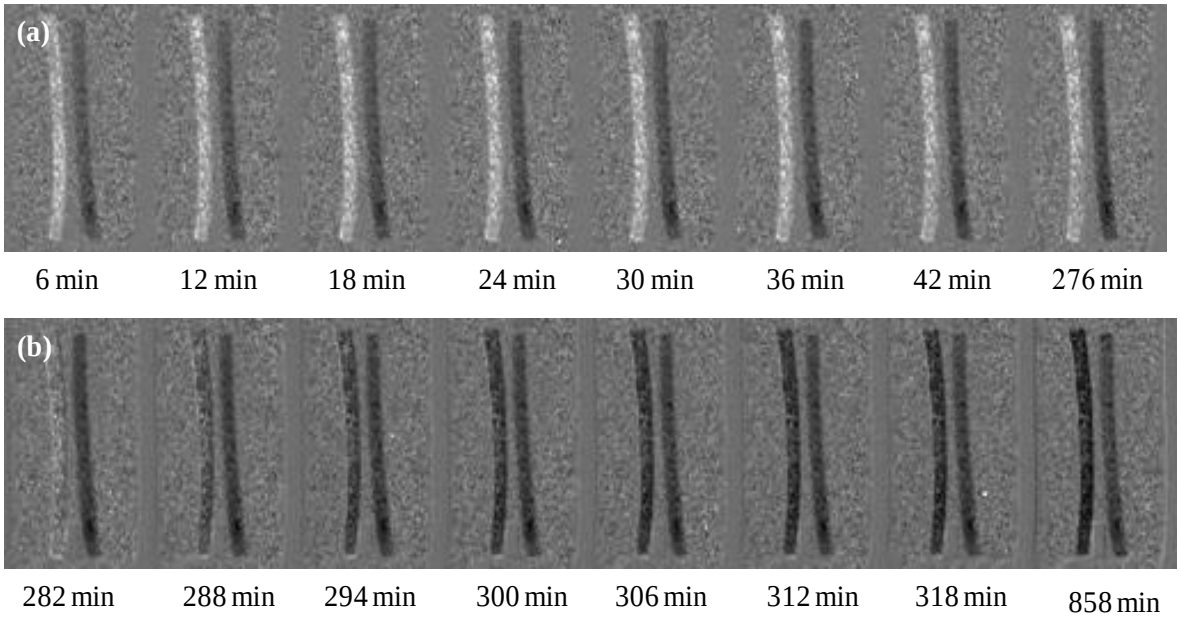

Figure 5.3 Time sequences of neutron images for CDI cell with 1.5 M LiCl solution in D_2O: (a) 1.2 V DC potential applied, the right electrode is negatively charged and (b) electrodes short-circuited during regeneration.

During electrosorption, the left electrode is positive and the right electrode negative, thus, $^{6}Li^{+}$ ions transfer from the solution to the right electrode and Cl^{-} ions transfer from the solution to the left electrode. We also observe that $^{6}Li^{+}$ ions on the right electrode are adsorbed throughout the width of the electrode. For the regeneration step [images in Series (b)], the electrode charge was removed by short-circuiting the electrodes. In the images of Series (b) of Figure 5.3, we observe that, as soon as the electrodes were discharged, the left electrode which was loaded with chloride ions, instead of releasing the Cl^{-} ions, adsorbed $^{6}Li^{+}$ ions to neutralize the charge of the Cl^{-} ions. The right electrode, which was loaded with $^{6}Li^{+}$ ions, remained dark with time suggesting that, instead of releasing $^{6}Li^{+}$ ions, it adsorbed Cl^{-} ions to neutralize the charge of the $^{6}Li^{+}$ ions. We expected adsorption of some counterions (lithium ions in this case) by the left electrode before the ions diffused out of the electrodes into the solution, as observed in a previous study (Sharma et al., 2013a). However, in this case another interesting observation is that, even after a period of approximately 10 hours, both electrodes are very dark, which means that regeneration failed. It is possible that this failure occurred due to precipitation of solid $^{6}LiCl$ salt in the pores of the electrodes owing to the localized high concentration of both $^{6}Li^{+}$ and Cl^{-} ions in both electrodes.

It should be noted that the phenomenon of counterion adsorption for neutralization after electrode discharging was also observed in the case of gadolinium nitrate in our previous work [18]. Thus, the commonly accepted behavior during the regeneration cycle, where we simply expect the adsorbed ions to diffuse out of the electrodes into the solution is not totally accurate. Instead, counterions first diffuse into the electrode pores. In the case of low salt concentration in the original solution, it was

observed [18] that after a certain period of counterion diffusion into the electrode pores, both types of ions diffuse back from the electrodes into the solution. However, in the case of high salt concentration, as it is the case of seawater or fracking water, as counterions diffuse into the electrode pores during regeneration, the temporally high concentration of positive and negative ions in the pores leads to precipitation of solids. The result of this behavior is that the CDI process becomes irreversible and cannot operate as planned.

The neutron imaging data presented here provide insight into the ion transport behavior during CDI, and reveal the mechanism of failure of CDI with high-salinity solutions, such as seawater and oil/gas produced or fracking water. Furthermore, the neutron imaging data can be used to improve the CDI process. Specifically, the saturation of electrodes during regeneration can be prevented by placing anion- and cation-exchange membranes adjacent to the electrodes, as is done in the MCDI setup. Figure 5.4 further illustrates the direction of ion transport during the regeneration step and shows how placing anion- and cation-exchange membranes can eliminate the transport of counterions into the electrodes during regeneration and, thereby, prevent undesirable saturation of the electrodes and precipitation of salt. Thus, the MCDI setup can play a significant role in desalination applications of high-salinity solutions, including seawater and fracking water. From the work of Lee at al. (2006) [13], where it was reported that MCDI is 19% more efficient than CDI (for low-salinity systems), it can be argued that the higher efficiency is due to blocking the counterion diffusion into the electrodes during regeneration. Based on the work of Lee et al. (2006), it is also expected that MCDI will work efficiently for the desalination of high-salinity solutions.

Figure 5.5 presents the neutron images for a sorption experiment carried out with 0.5 M lithium chloride in D_2O at 0 V and 1.2 V. The concentration profiles were obtained from the series of images to obtain the effective diffusivities at 0 V and 1.2 V. The images presented are difference from the first image in the series to show the relative transport of lithium ions as the experiment progressed.

5.3.3 Measurements

The equation for Fick's second law of diffusion was considered:

$$\frac{\partial C}{\partial t} = D_{eff} \frac{\partial^2 C}{\partial x^2} \tag{5.2}$$

with the following boundary conditions for the negative electrode in the system:

$C = C_1, \quad x = 0, \quad t \geq 0,$

$C = C_2, \quad x = l, \quad t \geq 0,$

$C = 0, \quad 0 < x < l, \quad t = 0.$

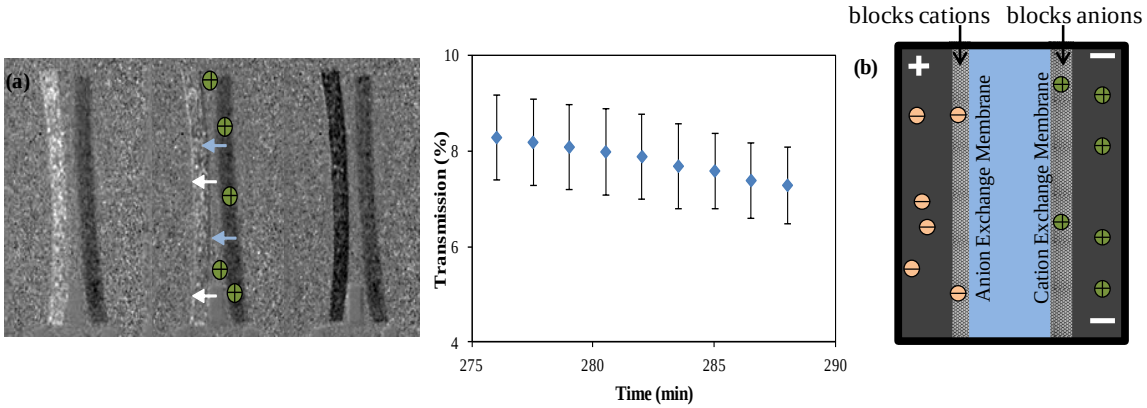

Figure 5.4 (a) Ion transport behavior during regeneration. The plot shows the decrease in transmission profile across the left electrode, which indicates adsorption of neutron blocking cations. (b) The schematic for membrane capacitive deionization setup shows how the ion exchange membranes can prevent adsorption of counter-ions during regeneration of electrodes.

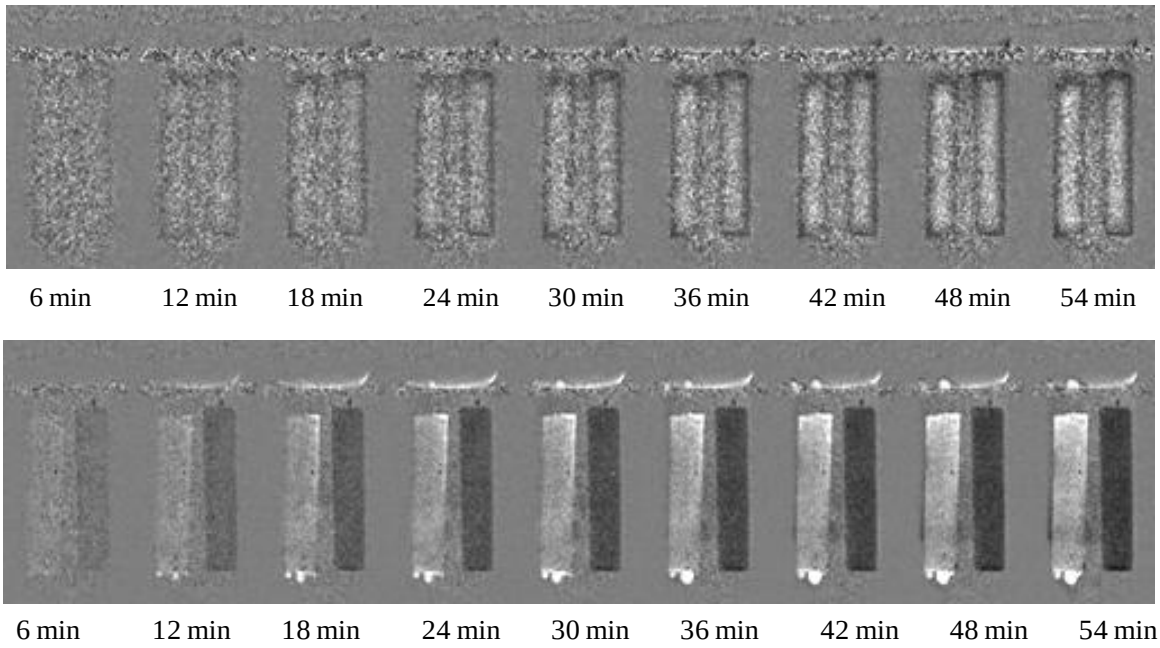

Figure 5.5 Time sequences of neutron images for the CDI cell with 0.5 M LiCl solution in D_2O: (a) no potential applied and (b) 1.2 V DC potential applied. In (b), the right electrode is negatively charged.

The electrode on the left is the negative electrode in our system. An analytical solution is obtained in this case (Crank, 1979):

$$C = C_1 + (C_2 - C_1)\frac{x}{l} + \frac{2}{\pi}\sum_1^{\infty}\frac{C_2\cos n\pi - C_1}{n}\sin\frac{n\pi x}{l}\exp\left(-\frac{D_{eff}n^2\pi^2 t}{l^2}\right) \tag{5.3}$$

where D_{eff} is the effective diffusion coefficient, C is the concentration of ions (defined as the total number of gadolinium ions in a volume of solution or electrode), x is the distance from the right edge of the electrode, t is the time, C_1 is the concentration at the right edge of the left electrode (0.00874 M), C_2 is the concentration at the left edge of the electrode (0.00874 M), and l is the width of the electrode. Since the only unknown in the equation (5.3) is D_{eff}, the value of the diffusion coefficient can be obtained by matching

the experimental data with calculated concentration histories. The value of the diffusion coefficient was obtained through this optimization process using the MATLAB(Matlab Users Guide et al., 1998) Optimization toolbox.

From the series of images in Figure 5.5, the concentration profiles obtained from experiments were analyzed using Fick's second law (equation 5.3) to obtain the value of effective diffusion coefficient of lithium ions as: 3.56×10^{-11} m^2/s at 0 V and 2.06×10^{-10} m^2/s at 1.2 V. The effective diffusivity of lithium ions increased by about 6 times on application of 1.2 V DC potential. Figure 5.6 shows a comparison of experimental data and modeling results for history of lithium ion concentration with and without applied voltage.

5.4 Conclusions

Neutron imaging has been demonstrated to be a useful tool to reveal the ion transport phenomena during the different cycles of the CDI process. With experiments conducted with 1.5 M lithium chloride solution, it was observed that the electrode pores became saturated with salt due to which the regeneration of electrodes did not occur. Thus neutron imaging gives an insight into why the CDI process is not efficient for desalination of solutions of high ionic concentration. When a potential of 1.2 V was applied between the electrodes, the effective diffusion coefficient of lithium ions increased approximately 6 times (at 0.5 M concentration). Information on the diffusivity of lithium ions in carbon materials at different values of applied potential can also aid in the design of lithium ion batteries. Electrical energy storage (EES) devices such as lithium batteries are an important tool for converting intermittent renewable energy into continuous peak energy.

An in depth knowledge about the ion transport mechanisms will help in developing advanced systems with higher capacity and better dynamic behavior, so that we can make renewable energy sources more reliable and economical. A fundamental knowledge of ion transport characteristics at the electrode/electrolyte interface will contribute immensely in the development of new electrode materials having longer durability and higher power generation.

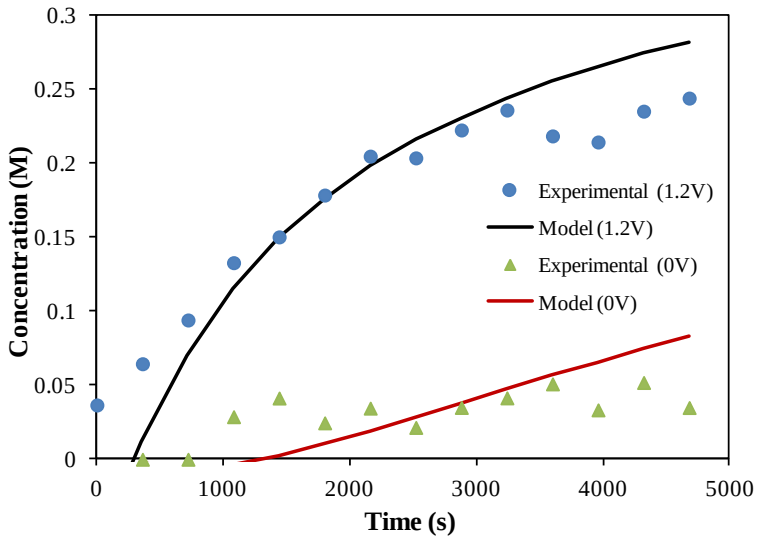

Figure 5.6 Concentration histories of lithium ions as a function of time at 0.80 mm from the right end of the electrode for the case of (a) 0 V and (b) 1.2 V applied potential.

CHAPTER 6

ENHANCEMENT OF ELECTROSORPTION RATES USING LOW-AMPLITUDE, HIGH-FREQUENCY ELECTRICAL POTENTIAL

The influence of low-amplitude, high-frequency, alternating-current (AC) electrical potential on ion transport in mesoporous carbon electrodes has been investigated. Mesoporous carbon electrodes of approximately 10-nm average pore size were synthesized based on a soft-template method. The carbon electrodes were used in capacitive deionization (CDI) experiments with salt solutions consisting of a mixture of ions of concentrations ranging from 5000 ppm to 10,000 ppm to investigate the effect of an AC potential on the ion removal rate. Higher rates of sorption and regeneration were observed when the AC potential was superimposed on a direct current (DC) offset of 1.2 V that is typically applied in CDI. The rate of ion sorption in CDI experiments was a dependant on the amplitude and frequency of the AC potential. Conductivity measurements showed enhancement in transport rates due to AC potential up to 130%. The effect was stronger during regeneration. Neutron imaging, a visualization technique, was also employed to quantify the diffusion of ions through mesoporous carbon electrodes under different conditions. Sequences of neutron images showed enhanced transport of gadolinium ions under the influence of AC potential. From the concentration histories of gadolinium ions inside the carbon electrodes, the effective diffusion coefficient of gadolinium ions was estimated to be $8.3\pm0.4\times10^{-11}$ m^2/s at 1.2 V DC and 1.1×10^{-10} m^2/s at 1.2 V DC with AC potential added.

6.1 Introduction

Inadequate access to clean drinking water is one of the major global challenges afflicting mankind. About 97.5% of water on earth is in the form of seawater (Shannon et al., 2008). To increase the supply of water resources, we need to adopt efficient recycling and conservation practices while devising new desalination technologies. The major desalination technologies currently in use are reverse osmosis (RO), multi-stage flash (MSF), and multi-effect distillation (MED). MSF distillation is a thermal-based desalination technology involving the phase change to water vapour, thus requiring large amounts of energy for operation (Anderson et al., 2010). Biofouling, scaling, and the need for energy intensive high-pressure pumps pose operational challenges in reverse osmosis (Oren, 2008). To address these challenges, we need to develop new low-cost energy-efficient methods for water desalination, which are simple in operation and have minimal impact on the environment.

Capacitive deionization (CDI), a method based on the electrosorption of ions by charged porous electrodes of high surface area, has been investigated in recent years as an alternative method for desalination of saline water. When an electrical potential is applied, ions in the solution accumulate in the electrical double layer formed at the solid-liquid interface of electrodes to counterbalance the surface charge. Regeneration of electrodes can be achieved by discharging the electrodes. The process operates at a low voltage, typically on the order of 1.2 V, and no secondary waste, other than concentrated brine, is produced during regeneration. CDI presents potential operational advantages over other water purification methods such as reverse osmosis since membranes or high-pressure pumps are not involved in its operation. The electrode material is an important

factor affecting the performance of the CDI process. A suitable electrode material for CDI should have a high surface area and low electrical resistivity to allow a rapid response of the entire surface area to charging and discharging of the electrodes. Carbon materials such as carbon aerogel (Gabelich et al., 2002; Hou et al., 2006; Xu et al., 2008; Yang et al., 2001; Ying et al., 2002), activated carbon (Oh et al., 2006; Ryoo et al., 2003), carbon nanotubes (Chen et al., 2010; Gao et al., 2009; Gao et al., 2007; Li et al., 2011; Pan et al., 2009; Wang et al., 2006; Zhang et al., 2007), graphene (Li et al., 2010a, b), and mesoporous carbon (Li et al., 2009; Tsouris et al., 2011) have been investigated as potential electrode materials. Recent review articles have discussed the various operational modes, electrode materials and cell geometries for the CDI technology (Anderson et al., 2010; Oren, 2008; Porada et al., 2013).

Besides developing high performance electrode materials, understanding the ion transport phenomena occurring at the electrode-electrolyte interface during electrosorption is critical in improving the efficiency of the process. Various parameters such as applied voltage, salinity, and size of ions in the solution govern the electrosorption behaviour of nanoporous carbon electrodes. Elucidating the underlying physics of the process can lead to enhancement in the transport rates of ions into the pores through tailoring electrode materials and charging/discharging strategies to the specific CDI application. In this study, it is hypothesized that one of the factors affecting the transport rate of ions in the porous carbon electrodes is the attractive electrostatic image force. This force arises between a charged ion and its image ion on the opposite side of a conducting planar surface. The image particle arises due to polarization of the conducting surface material by the charged particle. The coulombic interaction between

the charged ion and its image is attractive. During sorption of ions, the electrostatic image force in the nanopores causes the conductive wall to behave like a sticky surface for the ions and slows down ionic mobility in conductive membranes. It is proposed here that an oscillating electrostatic coulombic force can reduce the effect of the image force, thereby enhancing the transport rate of ions.

In this respect, we examine the influence of application of a low-amplitude, high-frequency, alternating-current (AC) potential on the charging and discharging rates during the CDI process. The influence of the AC potential superimposed on the direct-current (DC) potential has been found to increase desalination performance in the electrodialysis process (Barragán et al., 2002). In the present study, the effect of an AC potential (superimposed on the DC potential) on ion-transport rates during adsorption/desorption of ions by mesoporous carbon electrodes during electrosorption has been investigated. The study also presents neutron-imaging experiments of a CDI cell to observe the influence of application of AC potential on ion- transport in mesoporous carbon electrodes.

6.2 Materials and Methods

6.2.1 Materials Synthesis

Details of the synthesis and characterization of mesoporous carbon materials suitable for CDI have been described elsewhere (Sharma et al., 2013b; Tsouris et al., 2011). In summary, activated mesoporous carbon was synthesized by carbonization of nanostructured polymeric composites, obtained by the self-assembly of the triblock copolymer Pluronic F127 (BASF) and a phenolic resin, comprised of phloroglucinol and formaldehyde, in acidic conditions and ethanol. Formaldehyde was added while heating

the mixture. After heating the solution for 2 hours, the resultant F127-phenolic resin particles were separated from the remaining solution. The particles were washed in ethanol and dried in an oven for 3 hours. The polymer particles were carbonized in a nitrogen atmosphere at 1123 K for 2 hours. A physical mixture of solid KOH and mesoporous carbon particles was heated under flowing nitrogen gas to 1123 K for one hour. The mesoporous carbon (MC) powder was transformed into activated carbon sheets (ACS) through the use of non-porous carbon paper (Hollingsworth and Vose) with a polyvinylidene fluoride binder. For ACS, a slurry was prepared with activated MC powder with 7.5% wt PVDF (polyvinylidene fluoride) and dimyethyl formamide (DMF). The slurry was heated and spread onto the carbon fiber paper in a mould for drying. The samples were dried at 373 K under rough vacuum.

For preparing PMCG (phloroglucinol-based MC-coated graphite) electrodes, pholoroglucinol and Pluronic F-127 were dissolved in ethanol, and 3 M hydrochloric acid (HCl) (Mayes et al., 2010). Glyoxal was added and phase separation was observed after 20 minutes of stirring at room temperature. The mixture was stirred for another 30 minutes and the gel was separated from the solvent. The gel was spread onto the graphite plates and allowed to dry overnight at room temperature followed by 24 hours at 353 K. The mesoporous carbon coated graphite electrodes were carbonized at 1123 K under nitrogen.

The procedure for synthesis of monolithic carbon electrodes used in neutron imaging experiments has been described elsewhere (Sharma et al., 2013a). Briefly, phloroglucinol was dissolved in ethanol with the structure-directing template Pluronic F127, hydrochloric acid, and glyoxal. The phenolic carbon polymer was separated from

the solvent and dried at 353 K. The material was then made into a powder form, sieved to 40 mesh and mixed with Toho Tenax 344 milled carbon fiber to produce a blend. The polymer-carbon-fiber blend material was pressed into discs at 68 atm. The discs were carbonized at 1123 K at 2 K/min under a nitrogen atmosphere. The carbonized discs were machined into rectangular bars and a hole was then drilled into the end of each bar. A platinum wire was inserted into the end of each electrode bar and fixed with glue.

Nitrogen sorption analysis was performed using a Micromeritics Gemini Analyzer. Surface area was calculated using the Brunnauer-Emmet-Teller (BET) method. Pore size distributions were calculated in the 0.05 - 0.2 relative pressure region using the Barrett-Joyner-Halenda (BJH) method. Surface area analysis for the ACS sheets was done on the composite material, i.e., the activated carbon with binder and the carbon fiber backing, while the analysis of the MC-coated graphite electrodes was performed on a composite of mesoporous carbon and carbon fiber scraped off the graphite current collector.

6.2.2 Capacitive Deionization Experiments

Figure 6.1 illustrates the setup of the CDI experiments with AC potential superimposed on a DC potential applied to the electrodes. The experiments were conducted in a batch mode, while the salt solution was recycled continuously. A micro pump was used to recycle the salt solution (Instant Ocean® or sodium chloride, 150 ml total volume) from a reservoir to the CDI unit cell and back to the reservoir at a flow rate of 30 ml/min.

The conductivity of the solution was measured at the cell exit stream by using a conductivity probe [model 835 Multi Cell (Au) with Model 3082 EC Meter, Amber

Science, Inc., Eugene, OR]. The conductivity probe fed conductivity and temperature measurements into the EC meter. The data acquisition system recorded voltage, current, and conductivity for a certain time interval prior to turning on the voltage. Then, the power source was switched on, and the conductivity, current, voltage, and temperature were recorded for the duration of the experiment. Application of electrical potential resulted in the transport of ions from the salt solution into the electrodes. Regeneration of electrodes was accomplished by discharging the electrodes.

6.2.3 Neutron Imaging

Neutron imaging is a non-destructive technique based on the interaction of neutrons with the nuclei of atoms. Neutrons have several advantages for imaging as they are non-perturbing, highly penetrating, and can distinguish between different isotopes of the same element. Neutron imaging has been utilized to visualize water in fuel cells in order to improve the water management system of the cell (Aaron et al., 2011; Bellows et al., 1999; Boillat et al., 2008; Mukundan and Borup, 2009; Park et al., 2008; Pekula et al., 2005; Satija et al., 2004; Tang et al., 2010; Turhan et al., 2006). Neutron imaging has also been used to visualize the transport of lithium ions across the electrodes in lithium batteries (Kamata et al., 1997; Lanz et al., 2001; Siegel et al., 2011a). In the present work, neutron imaging of gadolinium ions was conducted to reveal ion transport phenomena in mesoporous carbon under different conditions of applied potential. In particular, we have studied the effect of application of low-amplitude, high-frequency electrical potentials on the diffusion of ions in mesoporous carbon electrodes.

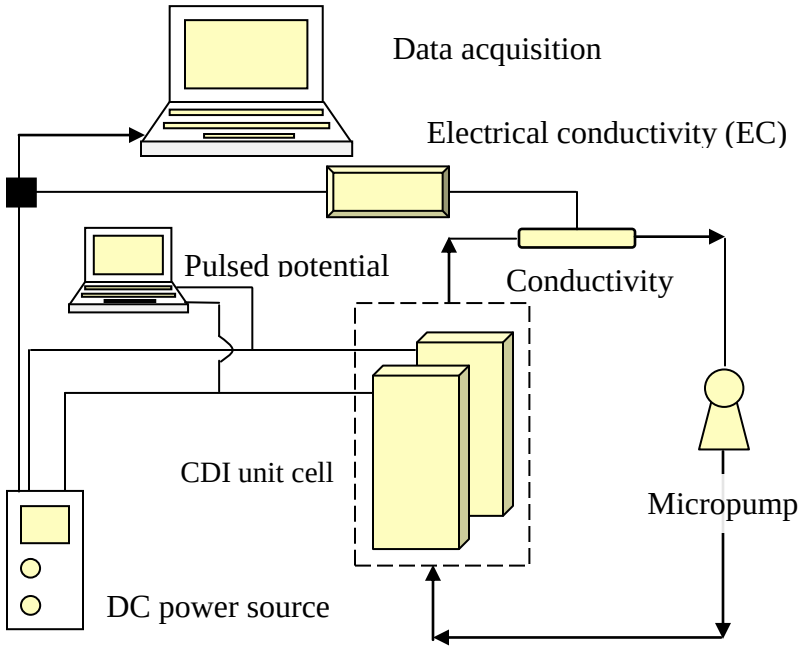

Figure 6.1 Schematic diagram of the setup for CDI experiments.

6.2.3.1 Neutron Imaging Principle

Neutron imaging is based on the Beer-Lambert principle, which relates the absorption of radiation passing through an object to the properties and thickness of the material. In neutron imaging, a neutron-sensitive ^{6}LiF/ZnS scintillation screen collects a two-dimensional projection of the sample and converts the neutrons to visible light. The image is then captured by a charge coupled device (CCD) camera. The attenuation of neutron beam caused by an object is given by the Beer-Lambert law:

$$I = I_o e^{-\mu\delta} \tag{6.1}$$

where μ is the linear attenuation coefficient given by:

$$\mu = \sigma \frac{\rho N_A}{M} \tag{6.2}$$

I is the intensity of the attenuated neutron beam, I_o is the intensity of the incident beam, δ is the uniform thickness of the object, σ is the material-specific total cross section for neutrons, ρ is the material density, N_A is the Avogadro constant, and M is the molar mass. Details of the methodology used in image analysis and how the concentration history of gadolinium ions is obtained can be found in previous work.(Sharma et al., 2013a) Gadolinium ions were used as they have a high neutron scattering cross-section of 260044 barn.(Sears, 1992) The change in the concentration of gadolinium ions can be obtained by the ratio of measurements of neutron intensity taken at times t_1 and t_2 (Siegel et al., 2011b) :

$$-\ln(I(t_2)/I(t_1)) = \sigma_{Gd} N_A \delta \, (c_{Gd}(t_2) - c_{Gd}(t_1)) \propto \Delta c_{Gd} \tag{6.3}$$

6.2.3.2 Neutron Imaging Experiments

The experimental setup for neutron imaging is shown in Figure 6.2 with the flow-through CDI unit cell constructed for neutron imaging experiments (Figure 6.2a). Details of the neutron-imaging experimental setup and electrode materials have been described in earlier work (Sharma et al., 2013a). Gadolinium (III) nitrate [$Gd(NO_3)_3$] in D_2O (100mL, 3000 ppm) was recycled through the CDI cell at a flow rate of 30 mL/min using a micropump. The experiments were conducted at the CG-1D neutron imaging beamline of the High Flux Isotope Reactor (HFIR) at Oak Ridge National Laboratory (ORNL).

6.2.3.3 Image Analysis

Image analysis was carried out by using the ImageJ (Rasband et al., 1997-2011) software developed at the National Institutes of Health. The transmission values were calculated at various points of the image. Since gadolinium ions block neutrons, a higher quantity of gadolinium ions in the electrode pores result in a lower transmission value at the particular point on the image. The increase in the concentration of gadolinium ions in the negative electrode was obtained from equation (6.3).

6.3 Results and Discussion

6.3.1 Materials Characterization

The nitrogen adsorption isotherms and BJH pore size distributions for the PMCG-FS (MC-coated graphite with a fiber sheet), and activated carbon sheet have been discussed in previous work (Sharma et al., 2013b; Tsouris et al., 2011). The pore size distribution for activated carbon sheets is in the range of 5-15 nm while that for the PMCG-FS material is around 5-20 nm. The surface area for the PMCG-FS material is 610 m^2/g, while that of the activated carbon sheet is 1040 m^2/g. The PMCG-FS material has a total pore volume of ~0.54 cc/g. The PMCG-FS has hierarchical porosity which is believed to enable higher active surface area and increased transport rates of ions through the material.

6.3.2 Capacitive Deionization Experiments

CDI experiments were conducted with activated mesoporous carbon sheet electrodes to study the influence of a square wave AC potential superimposed on a DC voltage of 1.2 V with a 5000 ppm aqueous sodium chloride (NaCl) solution. An AC potential of 10 mV amplitude and 100 kHz frequency was superimposed on a DC

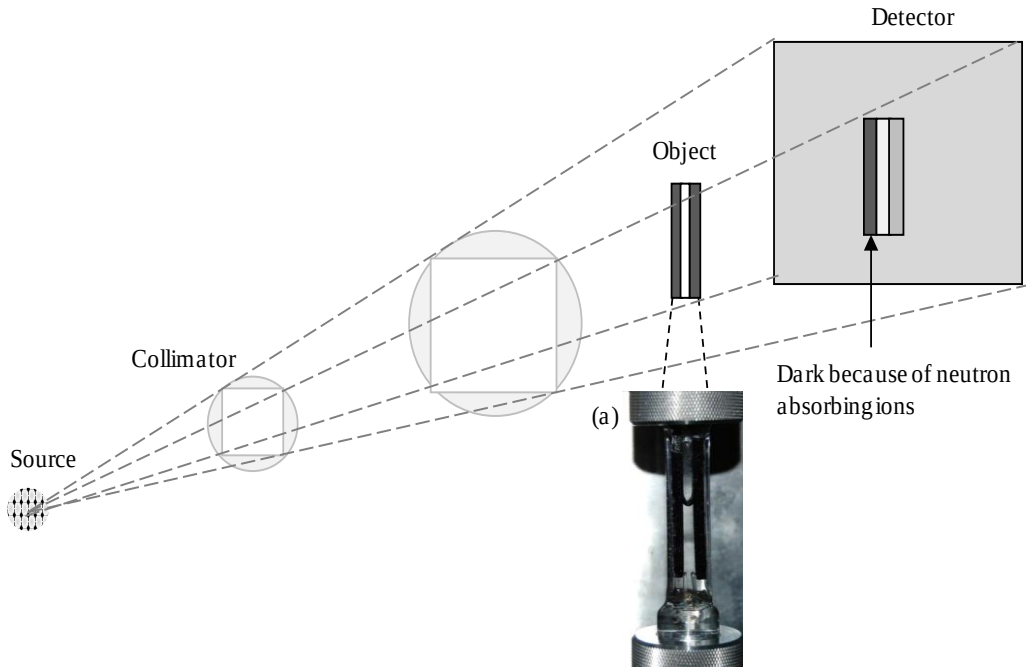

Figure 6.2 Neutron imaging setup. Inset (a) shows a picture of the flow-through cell used in the experiments with the electrodes constructed of ORNL mesoporous carbon.

potential of 1.2 V (Figure 6.3). The potential was turned on at t = 700 s and removed at t=3,200 s. Higher rates of sorption and regeneration of ions were observed in the case AC potential was applied, but it was observed that the effect of the AC potential was stronger in the case of desorption. Further experiments were conducted with PMCG electrodes to validate the observation made with activated carbon sheets (Figure 6.4). It was again observed that the sorption and regeneration rates were higher in the case an AC potential was added on to the DC potential.

The influence of AC potential on the ion removal rate was also investigated for Instant Ocean® solution of approximately 10,000 ppm concentration as illustrated in Figure 6.5. It was observed that the addition of AC potential had a stronger effect on the rate of regeneration. During regeneration without AC voltage, a delay was observed in

the increase of conductivity with time. The addition of AC potential eliminated this delay.

6.3.2.1 Influence of Amplitude of AC potential

The effect of amplitude of AC potential on sorption and desorption of ions was also investigated. The experiments were conducted with 1, 10, and 100 mV amplitude pulsed potential. Experiments conducted with 1 mV amplitude pulsed potential showed no significant difference from the case in which no pulsed potential was applied. The results tabulated in Table 1 show the sorption/regeneration behavior when the amplitude of AC potential varied from 10 mV to 100 mV. A sweeping frequency of the AC potential between 100 and 10 kHz was used in these experiments. The results of Table 1 show that the percentage increase in sorption rate is higher at higher amplitude of the AC potential with about 130% increase in sorption rate observed at 100 mV amplitude of AC potential.

6.3.2.2 Influence of Frequency of AC potential

The effect of the frequency of the AC potential was studied for amplitude of 10 mV. The frequency of AC potential was varied from 0.1 kHz to 100 kHz (Table 2), and it was observed that the enhancement in sorption rate increases with frequency up to 10 kHz.

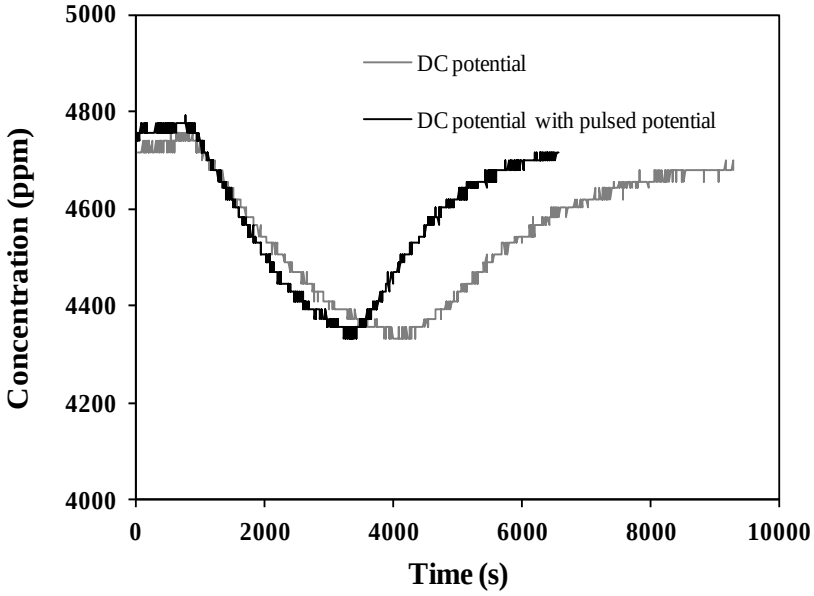

Figure 6.3 Influence of pulsed potential (10 mV, 100 kHz superimposed on 1.2 V DC) on ion sorption and desorption in solutions of approximately 5,000 ppm NaCl concentration with activated-carbon-sheet electrodes.

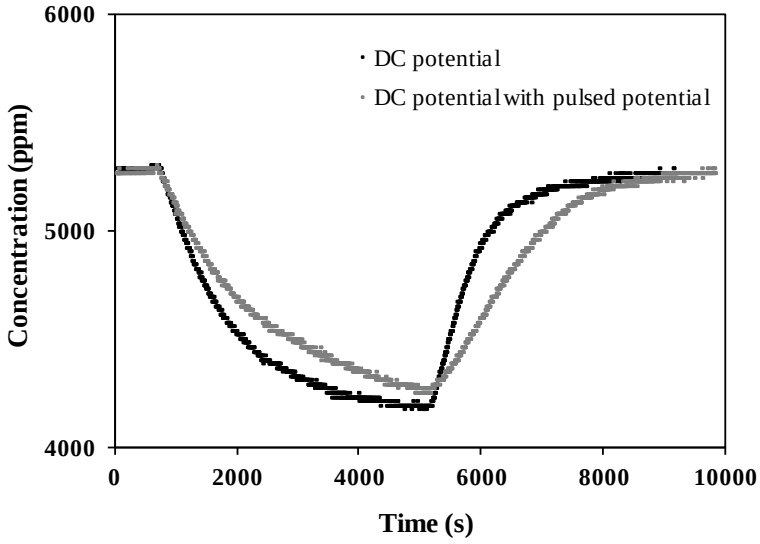

Figure 6.4 Influence of pulsed potential (10 mV, 100 kHz superimposed on 1.2 V DC) on ion sorption and desorption in solutions of approximately 5,000 ppm NaCl concentration with PMCG electrodes.

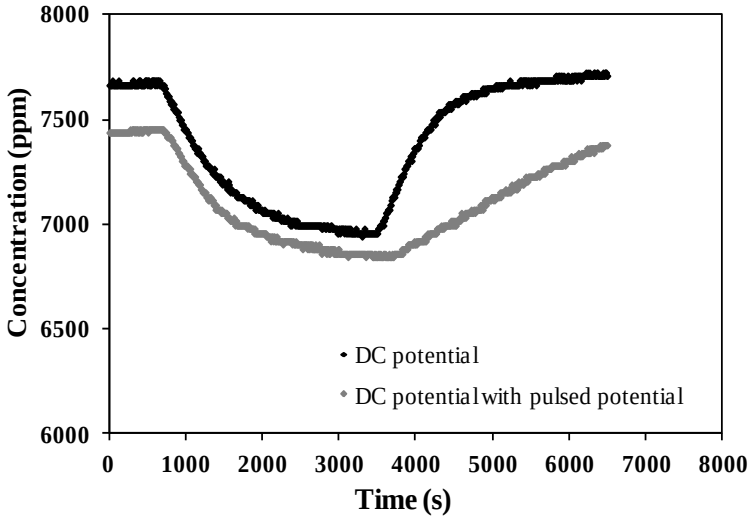

Figure 6.5 Influence of pulsed potential (100 mV, 100 kHz superimposed on 1.2 V DC) on sorption and desorption in solutions of approximately 10,000 ppm concentration of Instant Ocean with PMCG electrodes. (a) DC potential: sorption rate: 65 mg for the first 1000 s; regeneration rate: 28 mg for the first 1000 s. (b) pulsed potential: sorption rate: 80 mg for the first 1,000 s; regeneration rate: 89 mg for the first 1,000 s. The initial sorption and desorption rates were increased by 23% and 218%, respectively, when a pulsed potential of 100 mV amplitude was superimposed on the DC voltage.

Table 6.1 Influence of amplitude of pulsed potential on sorption/desorption of ions.

	Sorption rate (ppm/min)	Desorption rate (ppm/min)
10 mV amplitude		
Without pulsed potential	27.6	26.4
With pulsed potential	36.6	48.6
% Change in rate	+33%	+84%
100 mV amplitude		
Without pulsed potential	34.8	17.4
With pulsed potential	77.9	34.2
% Change in rate	+130%	+99%

Table 6.2 Sorption rate (ppm/min) as a function of frequency for 10 mV pulsed potential.

	100 kHz	10 kHz	1 kHz	0.1 kHz
Without pulsed potential	27.6	25.2	32.4	35.4
With pulsed potential	36.6	37.8	40.2	37.8
% Change	+33%	+50%	+24%	+6.4%

6.3.3 In-situ Electrode Characterization by Neutron Imaging

6.3.3.1 Image Sequences

The transmission values for the neutron images obtained with 1.2 V DC potential applied without and with a square wave AC potential of frequency 10 kHz and amplitude 0.1 V are presented in Figure 6.6. Since gadolinium ions absorb neutrons, an increase in gadolinium ion concentration results in a lower transmission value. The decrease in the transmission value at the electrode is greater in the case the AC potential was added onto 1.2 V DC potential, indicating a greater transport rate of gadolinium ions to the left (negative) electrode.

Figure 6.7 (a) presents a series of images obtained after 1.2 V DC potential had been applied with a square wave AC potential (10 kHz frequency, 100 mV amplitude) across the two electrodes for about 3 hours. At t = 0 minutes the DC potential was removed, and the AC potential was still kept applied across the electrodes. It was observed that the right electrode initially became darker as some of the gadolinium ions diffused into the right electrode after the removal of DC voltage. Figure 6.7 (b) further illustrates the direction of ion transport by presenting the decrease in transmission value across the right electrode after the removal of DC voltage. The average transmission value across the right electrode decreased by 11.5% (at t = 70 minutes) from the initial transmission value at t = 0 minutes (corresponding to an OD of 0.122). The decrease in transmission across the right electrode indicates the transport of gadolinium ions to the right electrode. It can be observed that after 70 minutes, the transmission across the right electrode started increasing indicating that the electrode stopped adsorbing gadolinium ions. This adsorption of counterions by the electrode occurs to counter the charge

imbalance in the electrode pores after the removal of the external potential. This phenomenon was observed for the case when no AC signal was applied (Sharma et al., 2013a), and as demonstrated in Figure 6.7, the phenomenon persists in the case of AC voltage applied.

6.3.3.2 Quantitative Measurements

The effect of the AC potential on the transport of ions from the solution to the electrodes was analyzed in terms of changes of the effective diffusivity of ions in the negative electrode. For this purpose, the equation for Fick's second law of diffusion was considered:

$$\frac{\partial C}{\partial t} = D_{eff} \frac{\partial^2 C}{\partial x^2} \tag{6.4}$$

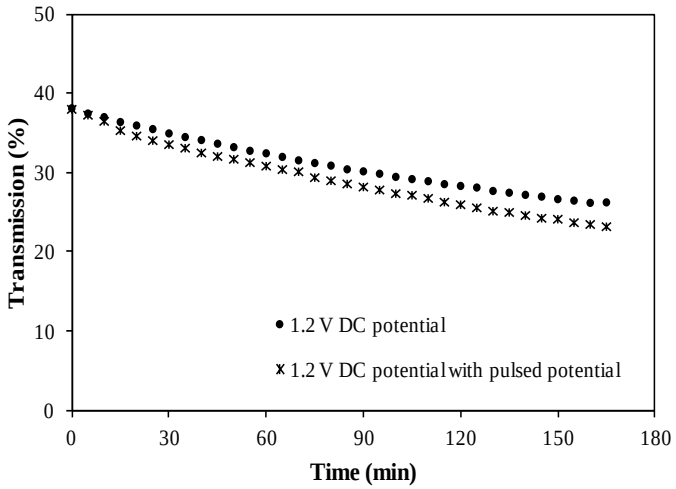

Figure 6.6 Average transmission of the neutron beam across the negative electrode after the external potential was applied. The transmission through the negative electrode decreases indicating uptake of gadolinium ions. Adding 100 mV amplitude pulsed potential accelerated the decrease in the transmission values due to a higher uptake rate of gadolinium ions.

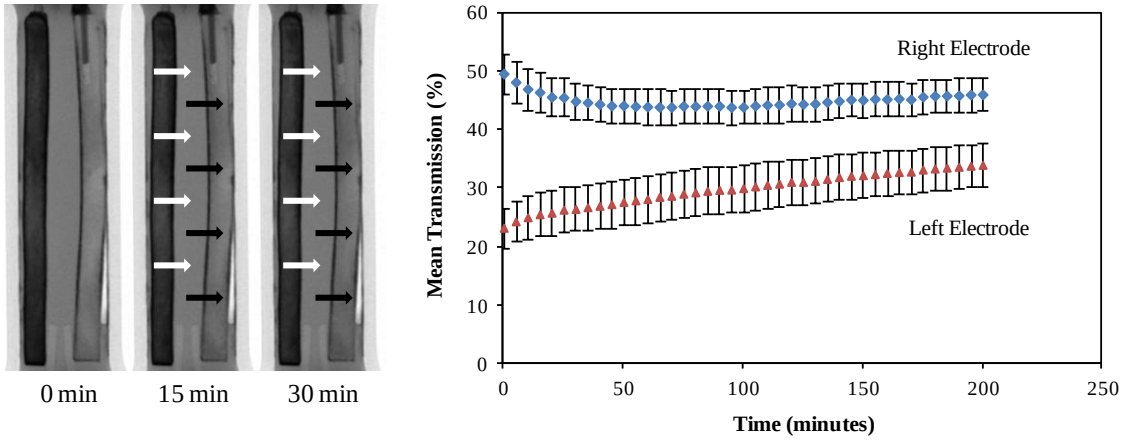

Figure 6.7 (a) Time sequence of neutron images after 1.2 V DC potential was removed at t = 0 min (with pulsed potential on). As expected, gadolinium ions were released from the left electrode to the solution between the electrodes (white arrows). However, gadolinium ions were also taken up by from the solution by the right electrode (black arrows) (b) Average transmission of neutron beam across the left and right electrodes, after the DC voltage was removed, and pulsed potential remained on. The transmission through the right electrode decreased in the beginning before starting to increase indicating initial transport of gadolinium ions to the right electrode.

The following boundary conditions apply for the negative electrode:

$C = C_1, \qquad x = 0, \qquad t \geq 0,$

$C = C_2, \qquad x = l, \qquad t \geq 0,$

$C = 0, \qquad 0 < x < l, \qquad t = 0.$

An analytical solution for the concentration of ions, C as a function of time is obtained (Crank, 1979):

$$C = C_1 + (C_2 - C_1)\frac{x}{l} + \frac{2}{\pi}\sum_1^{\infty}\frac{C_2\cos n\pi - C_1}{n}\sin\frac{n\pi x}{l}\exp\left(-\frac{D_{eff}n^2\pi^2 t}{l^2}\right) \qquad (6.5)$$

x is the distance from the edge of the electrode, t is time, D_{eff} is the effective diffusivity, C is defined as the number of gadolinium ions in a volume of solution or electrode, C_1 and

C_2 are the concentrations at the right and left edge of the electrode correspondingly (0.00874 M), and l is the width of the electrode. C_1 and C_2 have the same values because both sides of the electrodes are in contact with the solution flowing through the cell. The bulk solution concentration is considered constant because of the continuous flow of the solution through the cell. The value of diffusion coefficient (D_{eff}) was obtained through equation (6.5) using the MATLAB Optimization toolbox (Matlab Users Guide et al., 1998).

It should be noted that Fick's second law of diffusion was adopted mainly with the purpose of comparing the transport rates with and without AC potential applied. The Nernst-Planck equation includes both the electric-field and concentration-gradient forces driving the transport of ions. However, the solution of the Nernst-Planck equation for an asymmetric electrolyte is not the focus of the present analysis. From the concentration data and using equation (6.5) the effective diffusion coefficient at 1.2 V DC was determined to be $8.3\pm0.4\times10^{-11}$ m^2/s and $1.1\pm0.03\times10^{-10}$ m^2/s at 1.2 V DC with AC potential superimposed. Thus the diffusion coefficient of ions with an applied AC potential superimposed on a DC potential was 35% higher than in the case where only a DC potential was applied.

It is expected that the AC effect depends strongly on the type of porous material used. In the case discussed here, mesoporous carbon of a narrow pore size distribution in the range of 10 nm was used, thus the effects reported here refer to similar materials. Information on the diffusivity of ions under the influence of an AC potential can be employed to produce electrode materials with desirable porosities for efficient ion removal in the CDI process.

6.4 Conclusions

This study is focused on the influence of an AC potential, superimposed on the DC potential that is normally applied to CDI systems, on ion transport in mesoporous carbon materials. Capacitive Deionization experiments showed an increase in ion removal rates when an AC potential was superimposed on the DC offset. The influence of the AC potential was greater on the regeneration rate. Neutron imaging was also employed to quantify the influence of AC potential on the transport characteristics of ions in mesoporous carbon electrodes. The effective diffusion coefficient increased by 35% when an AC potential of ±100 mV was superimposed onto to the applied DC potential of 1.2 V during electrosorption. The hypothesis for the AC potential effect reported here is that there is an electrostatic attractive force that hinders a rapid transport of ions through the pores of the carbon material. With the application of an AC potential, due to a reduction in the electrostatic attractive force, the transport rate of ions in the electrodes increases. Furthermore, electrode specific sorption and regeneration rates can be optimized by varying the frequency and amplitude of the AC potential to achieve a more efficient desalination device.

CHAPTER 7

NEUTRON IMAGING OF BLUE ENERGY RECOVERY CYCLE

The mixing process of fresh water and sea water releases a significant amount of energy and is potentially an enormous source of renewable energy. The so called ‘blue energy’ or salinity gradient energy can be harvested by a device consisting of carbon electrodes immersed in an electrolyte solution, based on the principle of capacitive double layer expansion (CDLE). In this study, we have investigated the feasibility of energy production based on the CDLE principle. Mesoporous carbon materials synthesized at the Oak Ridge National Laboratory (ORNL), were used as electrode materials in this work. Neutron imaging of the blue energy cycle was conducted with cylindrical mesoporous carbon electrodes and 0.5 M lithium chloride as the electrolyte solution. For experiments conducted at 0.6 V and 0.9 V applied potential, a voltage increase of 0.061 V and 0.054V was observed respectively. Moreover from the sequences of neutron images obtained for each step of the blue energy cycle experiments, we obtained information on the direction and magnitude of lithium ion transport.

7.1 Introduction

The depletion of fossil fuels drives the need for new clean, renewable sources of energy. The mixing of saline water with fresh water that takes place at the mouth of rivers, leads to dissipation of free energy, due to an entropy increase experienced by the mixing solutions. This entropy increase due to controlled mixing of two solutions of different salinity can be harnessed to obtain electrical energy (Norman, 1974). The process is clean and no green-house gases or secondary byproducts are formed which could have harmful impact on the environment.

The free energy release is around 2.4 kJ when one liter of freshwater is mixed with salt water, which is equivalent to a waterfall of 200 m (Pattle, 1954). The potential of energy extraction from all the river estuaries worldwide is estimated at around 2 TW, which could account for about 20% of the global energy demand (Post et al., 2008; Wick, 1978). This renewable source of energy known as 'blue energy' or salinity gradient energy has been discovered since the 1950's, but a commercially viable method to tap the energy has not been devised until recently. The energy can be harvested by interposing a suitable device between the salt and the fresh water, so that mixing takes place in a controlled way.

The technologies which have been investigated include pressure retarded osmosis (PRO) (Achilli et al., 2009; Thorsen and Holt, 2009), reverse electrodialysis (RED) (Długołęcki et al., 2009; Post et al., 2008; Veerman et al., 2009; Weinstein and Leitz, 1976) and capacitive energy extraction. The PRO technique utilizes the osmotic pressure difference across a semi-permeable membrane that is interposed between fresh and saline water. The pressure difference that drives the flow of water across the membrane, is

converted into electrical power by the means of a turbine and pressure exchanger. Thorsen and Holt (2009) presented results from a theoretical model that show approximately 40% of the mixing energy of freshwater with seawater or 1 MW/(m^3/s) can be obtained with the PRO process (Thorsen and Holt, 2009). Achilli et al. (2009) developed a PRO model to predict water flux and power density and determine optimal membrane characteristics and configuration for design of a PRO system. Power densities of 2.7 and 5.1W/m^2 were observed for 35 and 60 g/L NaCl draw solutions respectively (Achilli et al., 2009). In RED, compartments fed alternatively by fresh and saline water are separated by a stack of cation and anion exchange membranes. The chemical potential difference between fresh and salt water generates a voltage difference over each membrane. The total potential of the system is the sum of potential difference over the ion exchange membranes and the end electrodes. Długołęcki et al. (2008) developed a theoretical membrane model and predicted that the best available anion exchange membranes can reach a power density of more than 5 W/m^2. Based on the model calculations, they proposed that higher power density could be obtained by using thin spacers and membranes with low membrane resistance and high permselectivity (Długołęcki et al., 2008). Veerman et al. (2009) reported the power density of a RED stack of 50 cells to be 0.93 W/m^2 which is the highest value reported with RED. They proposed that a higher power density can be obtained with a more open spacer and manifold desgin (Veerman et al., 2009). The main drawbacks of PRO and RED technologies include the use of membranes that are expensive and prone to fouling. Moreover, the methods involve pumping and the need for energy converters and in addition, the membranes do not have high selectivity.

A recent technology based on extracting energy by charging carbon electrodes in a saline solution, and discharging them in fresh water. Capacitive energy extraction is based on Capacitive Double-Layer Expansion (CDLE) (Brogioli, 2009; Brogioli et al., 2012; Brogioli et al., 2013) or Capacitive energy extraction based on Donnan Potential (CDP) (Liu et al., 2012; Sales et al., 2012a; Sales et al., 2012b; Sales et al., 2010). When extracting energy based on the CDLE principle, fresh and saline water sequentially flow in the space between two electrodes connected via an external power source. When saline water flows through the cell, the electrodes are charged up. On switching to the flow of fresh water, the double layers in the electrode expand and the cell voltage increases spontaneously leading to power production.

There are four steps in the charging and discharging process to extract electrical energy by capacitive double layer expansion (Figure 7.1):

Step I: The electrodes are charged in a concentrated saline solution. The circuit is closed and the current flows through the circuit. Salt water is being circulated across the cell.

Step II: The circuit is opened and fresh water flows through the cell. The cell potential increases due the double layer expansion.

Step III: The circuit is closed and the current flows in reverse direction.

Step IV: The circuit is opened and saline water is allowed to circulate through the cell. This step closes the cycle.

In the present work, neutron imaging experiments were conducted to visualize the ion transport across mesoporous carbon electrodes during the various stages of the capacitive blue energy cycle.

7.2 Materials and Methods

7.2.1 Capacitive Deionization Experiments

The setup for capacitive deionization (CDI) experiments was modified so that the circuit could be opened and closed by using a switch for the different stages of the blue energy cycle. A simple schematic of the CDI setup for blue energy experiments is shown in Figure 7.2. The saline solution used in the experiments was sea-water diluted with deionized water at approximately 6000 ppm concentration. After step I, the sea-water solution was replaced by deionized water. A flow rate of 46 ml/min was maintained in the experiment.

7.2.2 Capacitive Deionization Cell for Neutron Imaging

A specially designed CDI cell, containing mesoporous carbon electrodes in electrolyte solution, was used in the study. The cell was filled up with 70 mL of lithium-6 chloride (^{6}LiCl) solution of 0.5 M concentration, and the experiments were conducted in a batch mode. After step I, the salt solution was drained out and the cell was filled with pure deuterium oxide (D_2O). After step III, D_2O was again drained out from the solution and replaced by ^{6}LiCl solution. Lithium-6 isotope was used as it has a high neutron attenuation coefficient of 940.97 barns. D_2O was used instead of normal water as hydrogen has a high neutron scattering cross section, which can inhibit the visualization of the lithium ions in the experiments.

7.2.3 Materials Synthesis and Characterization

The electrodes used in neutron imaging were composed of monolithic, mesoporous carbon synthesized at the Oak Ridge National Laboratory (ORNL), as

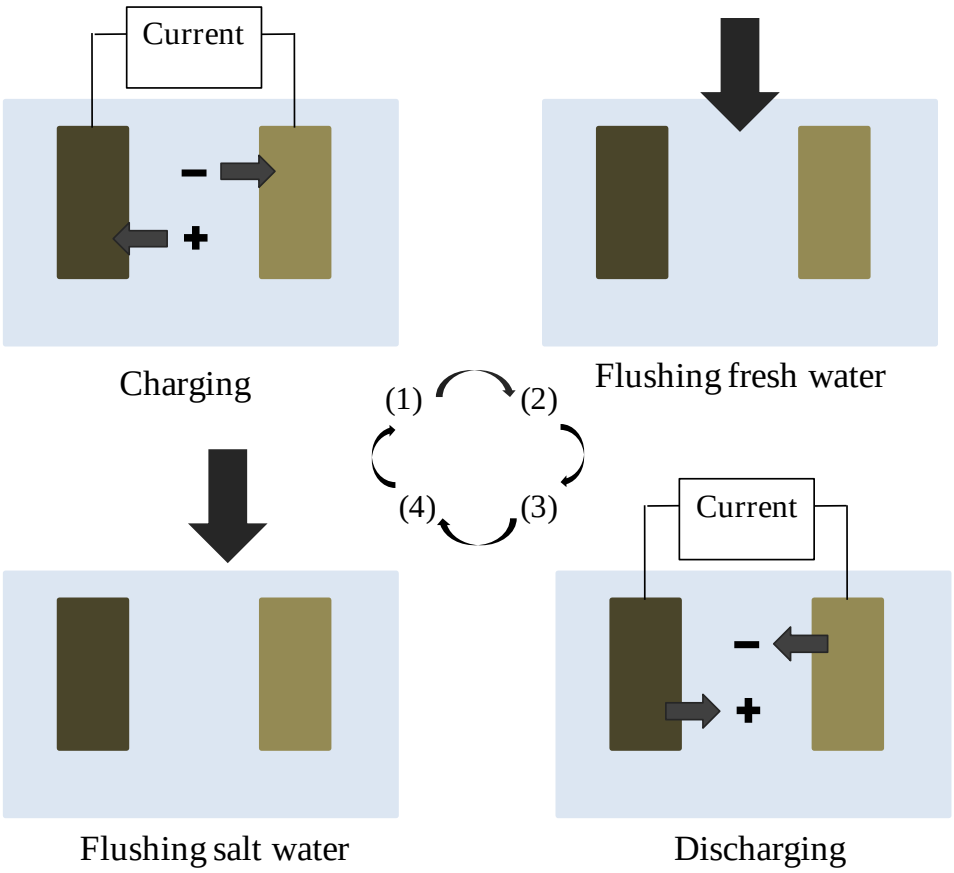

Figure 7.1 Steps of the blue energy cycle based on the CAPMIX technique. The cell is filled with salt water in the beginning. The steps are (1) charging (Step I), (2) flow of fresh water (Step II), (3) discharging (Step III), and (4) flow of saline water (Step IV).

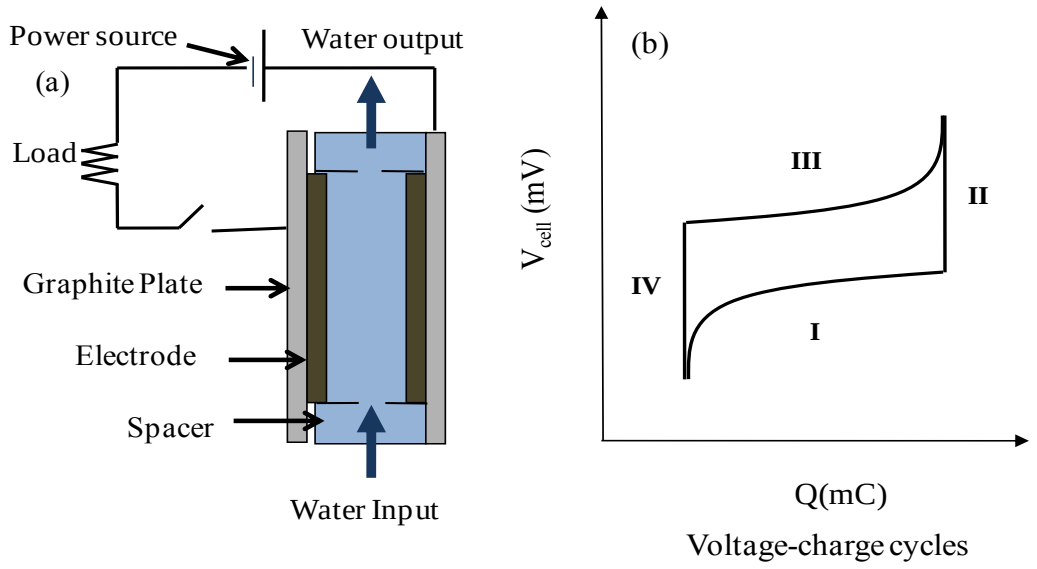

Figure 7.2 (a) Schematic view of the capacity energy extraction experimental setup. (b) Typical voltage-charge cycle.

previously reported (Sharma et al., 2013a). The synthesis method results in a mesoporous carbon material with high porosity. A platinum wire was pressed into the end of each electrode bar for electrical connection and glued at the tip of the electrode. Surface area measurements were performed with a Micromeritics Tristar 3000 at 77 K with nitrogen as the adsorbate.

7.2.4 Neutron Imaging Principle

The neutron imaging experiments were performed at the CG-1D beamline at the High Flux Isotope Reactor (HFIR) at ORNL (Bilheux et al., 2013). Neutron Imaging is based on the principle of Beer-Lambert law, which gives a linear relationship between the absorbance and concentration and the length of the path through the sample species that

absorbs radiation. The attenuation of the beam caused by a uniformly thick, homogeneous sample is given by the Beer–Lambert equation:

$$I = I_0 e^{-\mu\delta} \tag{7.1}$$

where I is the intensity of the neutron beam after attenuation, I_0 is the intensity of the incident beam, μ is the attenuation coefficient, and δ is the thickness of the sample.

7.2.5 Neutron Imaging Experiments

The experimental setup for neutron imaging is shown in Figure 7.3. In the experiments conducted in the present study, the specially designed CDI cell was filled up with lithium chloride (^{6}LiCl) solution in deuterium oxide (D_2O). The electrodes in the cell were connected to a power supply (HP 3632A; Hewlett Packard, CO) through the platinum wire leads, so that the applied potential could be remotely adjusted away from the beam.

The experiment was conducted in four cycles typical for energy extraction by capacitive double layer expansion:

Step I: The cell was filled up with 0.5 M ^{6}LiCl salt solution. The electrodes were charged on application of external potential. The circuit was closed and there was current flow through the circuit.

Step II: The circuit was opened and the cell was filled up with D_2O solution. The potential across the electrodes was measured as a function of time.

Step III: The circuit was closed and the current flow was in reverse direction.

Step IV: The circuit was opened and the cell was filled up with salt solution again. This

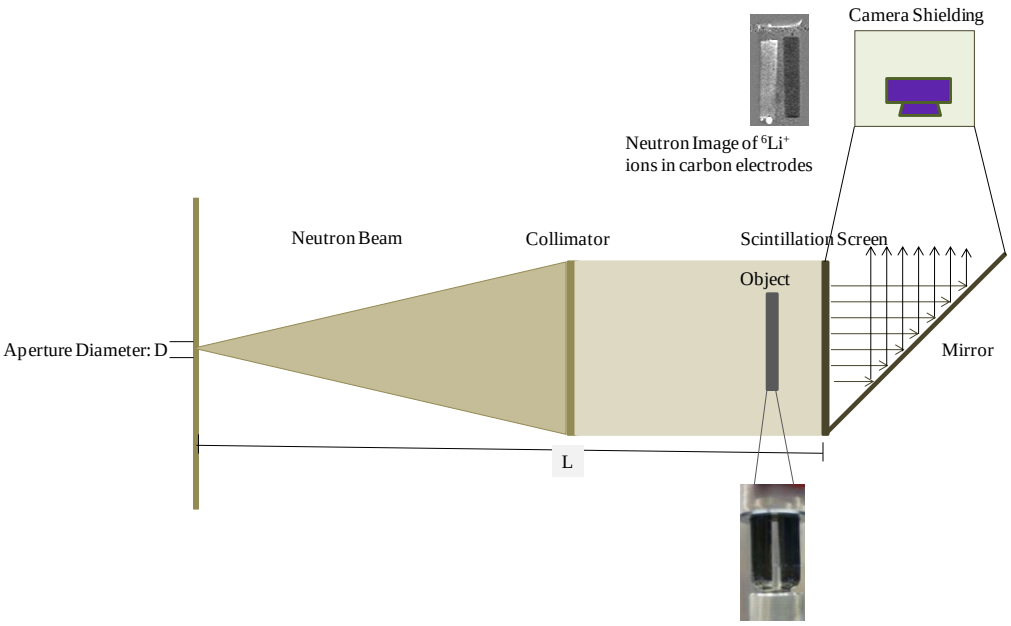

Figure 7.3 Neutron imaging experimental setup for blue energy experiments.

step closed the cycle for each experiment.

During all four stages of the cycle, the potential across the electrodes was measured continuously as a function of time.

7.2.6 Image Analysis

The image analysis was carried out by using the ImageJ (Rasband et al., 1997-2011) software developed at the National Institutes of Health. The images shown have been normalized by dividing all the images by the first image in the series to visualize the transport of ions in each step of the blue energy cycle.

7.3 Results and Discussion

7.3.1 Materials Characterization

From the characterization studies, the pore surface area of the mesoporous carbon for the

cylindrical electrodes used in the study was determined to be 365 m^2/g. Also, the pore volume at $P/P_o = 0.995$ is 0.43 cm^3/g and the average pore size is centered at 10 nm. Nitrogen sorption isotherms and BJH (Barrett– Joyner–Halenda) pore size distributions for mesoporous carbon are shown in Figure 7.4.

7.3.2 Capacitive Energy Extraction

The experiments were based on sequentially flowing fresh and saline water through the CDI cell. The voltage across the electrodes, current, and conductivity of the solution were continuously measured throughout the entire duration of the experiment.

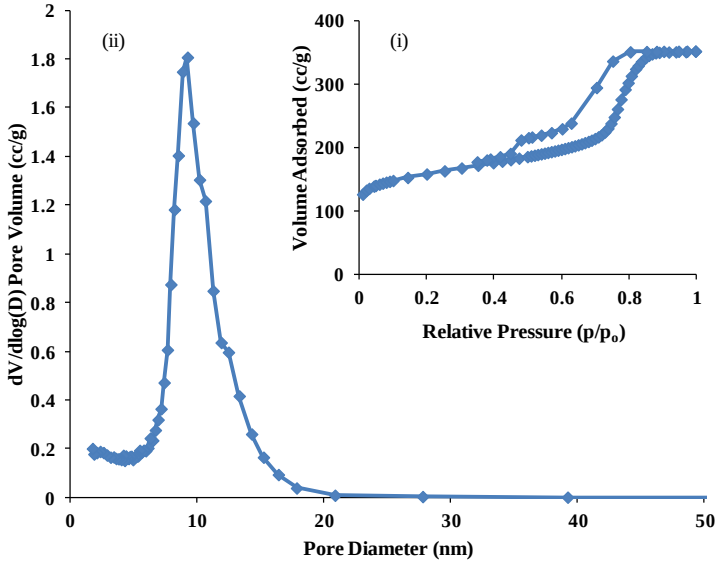

Figure 7.4 (i) Nitrogen adsorption isotherms and (ii) BJH pore-size distributions for the mesoporous carbon used in neutron imaging experiments. The pore surface area of the mesoporous carbon is 365 m^2/g, and the average pore size is around 15 nm.

The experiments were conducted to determine if there was a voltage increase across the electrodes during the switching step I (soaking step) when deionized water is flushed through the CDI cell.

For experiments conducted at 1.2 V, no increase in voltage was observed during step II, and the potential across the electrodes kept dropping as the external potential had been removed. For experiments conducted at 0.6 V, the potential increased up to 0.612 V from 0.6 V within 650 seconds.

7.3.3 Image Sequences

A series of images obtained in the cycle with 0.6 V applied across the electrodes is shown in Figure 7.5. All the images shown have been obtained by dividing the respective images by the first image in the series to provide a good contrast for observing ion transport. In the series 7.5 (a), images corresponding to an applied potential of 0.6 volts in the charging step of the cycle are shown. With the voltage applied across the electrodes, the lithium ions diffuse inside the left electrode that is negatively biased. It is assumed that chloride ions migrated to the right electrode to balance the charge. The series 7.5 (b) corresponds to the step II in which the cell is filled with D_2O solution and the external potential is removed. Due to the concentration gradient, the lithium ions which were present in the pores of the electrode start diffusing out into the solution. This is evident from the image series as the region inside the electrodes (particularly near the edges) is getting lighter as time progresses. During this step the potential across the electrodes was continuously measured as a function of time, the potential rose from 0.601 V to 0.662 V during a period of 5 hours.

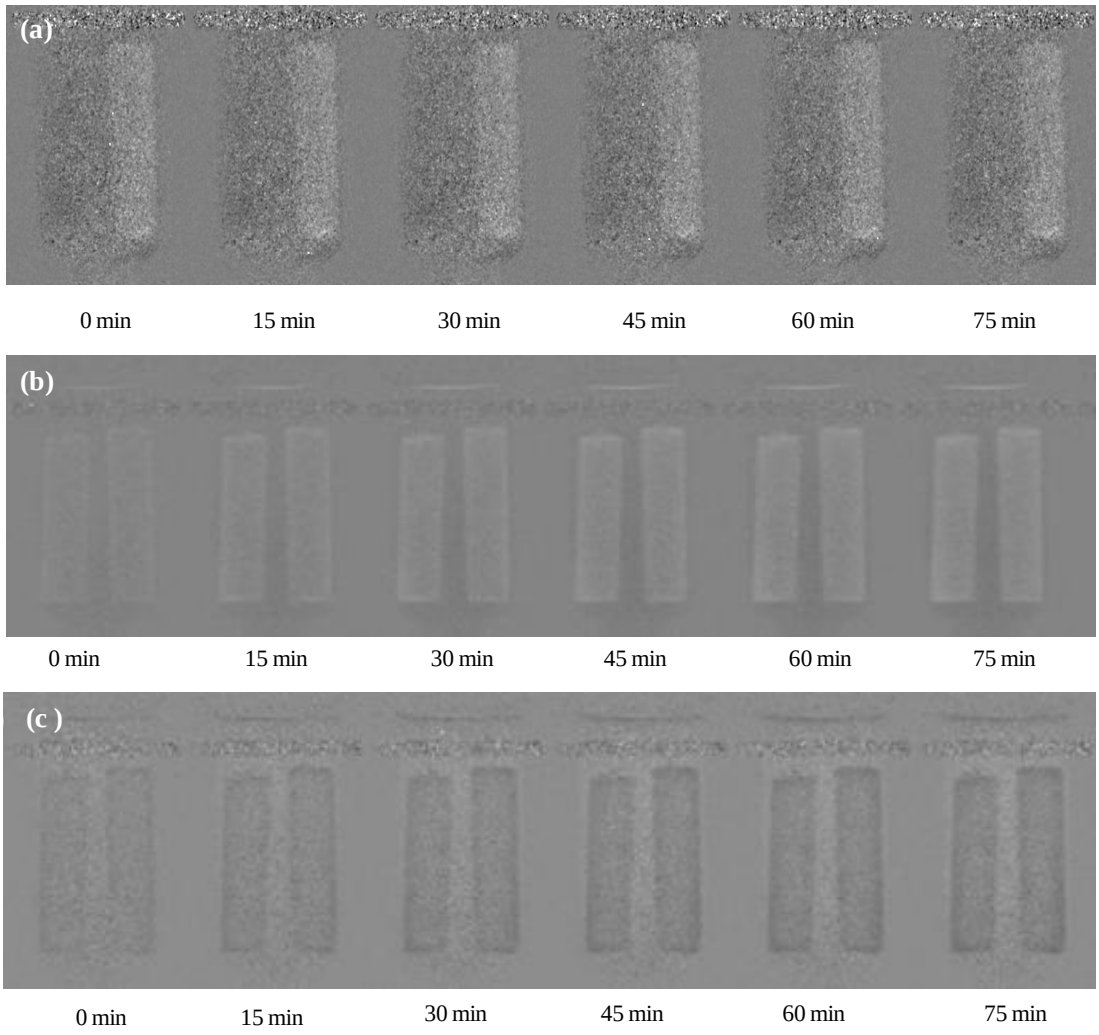

Figure 7.5 Time sequences of neutron images for blue energy cycle (for 0.6 V applied potential) with 0.5M LiCl solution in D_2O: (a) Step I, (b) Step II, (c) Step IV.

In step III the circuit was closed and the electrodes were discharged to the initial potential. This step was quite fast and no images were acquired during that period. The step IV is shown in the series 7.5 (c). In this step the circuit was opened and the cell was again filled up with the salt solution. In the series 7.5 (c), the electrodes are getting darker, as the lithium ions diffuse inside the electrodes.

Figure 7.6 illustrates the change in average transmission value across the electrodes after the potential was removed and the cell flushed with D_2O in the switching step. In this step, we expect the double layers in the pores of the electrode to expand due to the presence of low concentration solution outside the pores. As time progresses, we expect the concentration of salt solution in the electrode pores to decrease as lithium ions move out into the solution due to the concentration difference. This is evident from the increase in relative transmission value across the electrodes with time (Figure 7.6a). During step IV, the circuit is open and ^{6}LiCl salt solution is introduced into the cell. Due to concentration gradient, lithium ions move inside the pores of the electrode, which is evidenced by the decrease in the average transmission value across the electrodes (Figure 7.6b).

In Figure 7.7 (a), images corresponding to an applied potential of 0.9 V, in the charging step of the cycle, are shown. The image series in the experiments with 0.9 V applied followed the same behavior as with 0.6 V. After step I, when the external potential was removed, the potential increased from 0.9 V to 0.954 volts over a period of 6 hours. Figure 7.8 further demonstrates the ion transport behavior by showing the change in transmission across the electrodes. The transmission increased during step II, as the lithium ions migrate out of the pores into the solution to counter the concentration

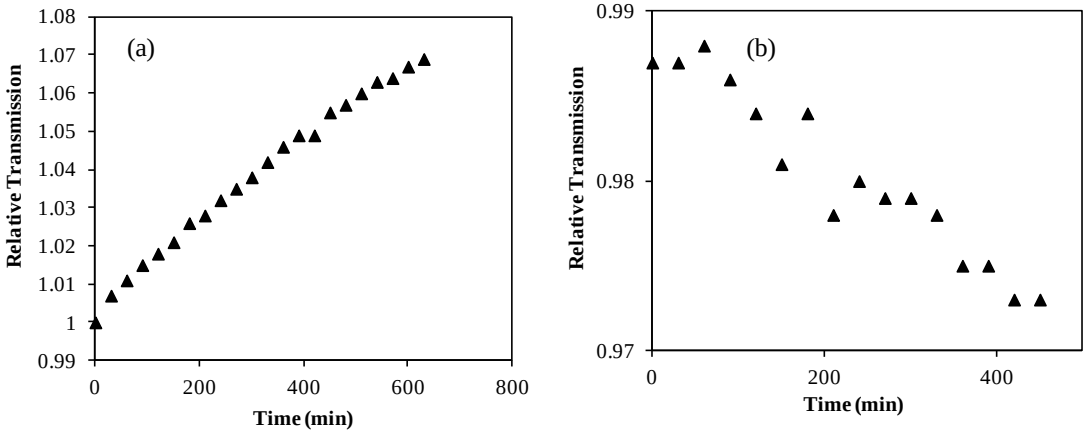

Figure 7.6 Relative transmission value at electrode for (a) Step II and (b) Step IV for blue energy cycle at 0.6 V.

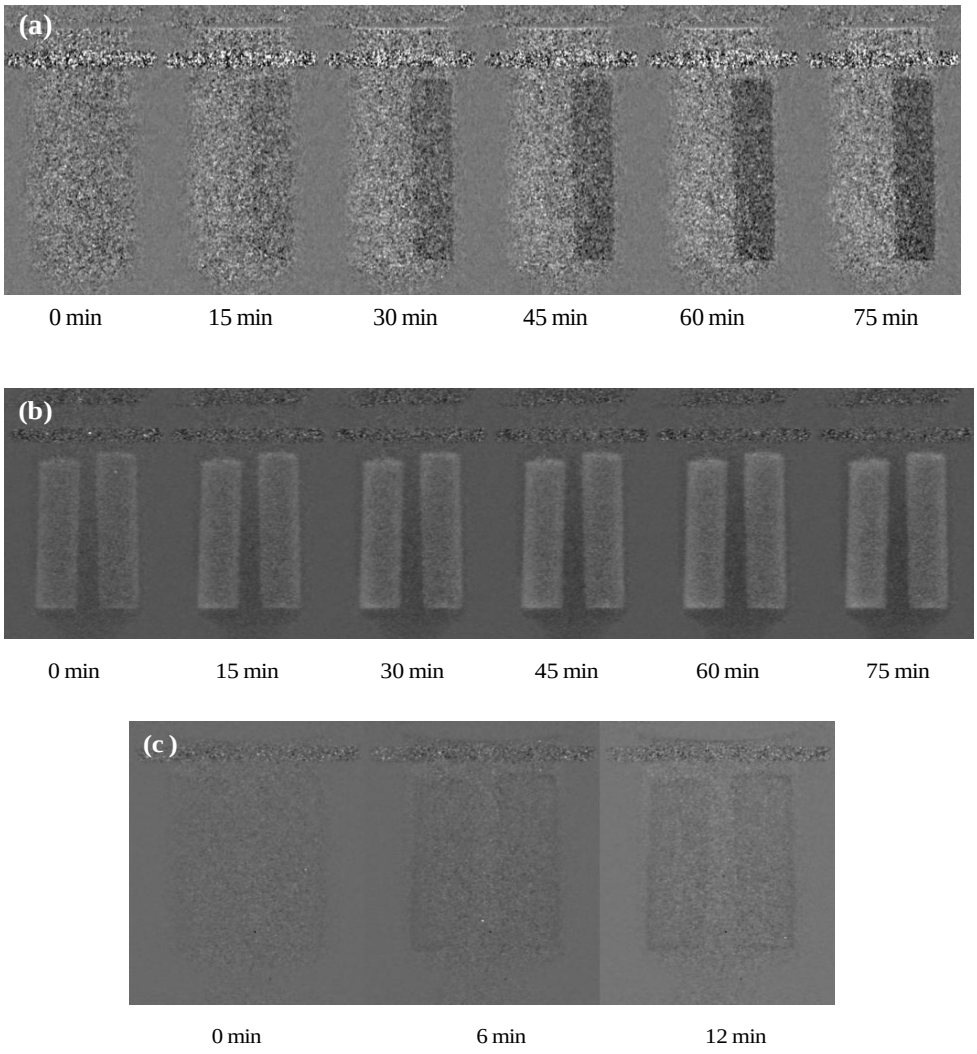

Figure 7.7 Time sequences of neutron images for blue energy cycle (for 0.6 V applied potential) with 0.5M LiCl solution in D_2O: (a) Step I, (b) Step II, (c) Step IV.

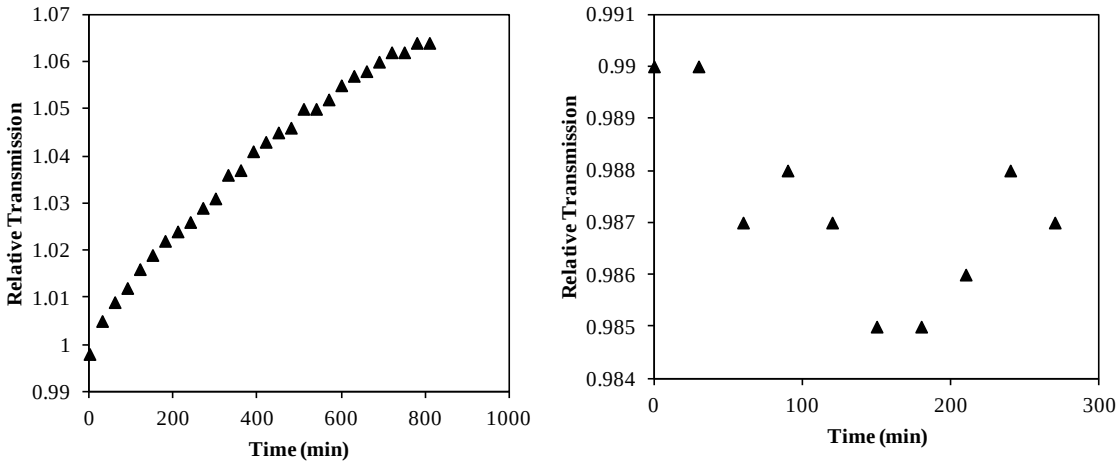

Figure 7.8 Relative transmission values at electrode for (a) Step II and (b) Step IV for blue energy cycle at 0.9 V.

gradient. During the step IV, the electrodes were again saturated with lithium ions resulting in a decrease in transmission value with time.

7.4 Conclusions

In the present study, neutron imaging of the blue energy cycle has been carried out to observe the direction of ion transport across the electrodes during the various stages of the cycle. In both the CDI and the neutron imaging experiments, the cycles conducted at 1.2 V applied potential did not yield satisfactory results and there was no voltage increase observed during step II. For the cycles carried out at 0.6 V and 0.9 V applied voltage, we observed an increase in voltage during the step II when water was flushed through the cell. Thus it can be deduced that a voltage range of 0.6-0.9 V is suitable for the operation of blue energy cycle. Neutron imaging was employed to visualize the transient behavior of ions during the different steps of the blue energy cycle. The transmission profiles across the electrodes as a function of time further provide

information on the direction and magnitude of ions transport. In depth knowledge on the ion transport mechanisms during the different steps of the blue energy cycle can help in devising strategies on how to maximize the energy produced per cycle.

CHAPTER 8

CONCLUSIONS AND RECOMMENDATIONS

8.1 Conclusions

The work combines experimental and modeling studies to investigate the electrosorption mechanism of ions in the pores of mesoporous carbon materials. The main contribution of this research is examining the effect of operational parameters such as applied potential, temperature of solution, ionic concentration, and valence of ions on the electrosorption behavior of mesoporous carbon materials. Laboratory scale CDI experiments have been conducted to investigate the influence of operational parameters on sorption by mesoporous electrodes and their regeneration on removal of external potential. Furthermore, the ion transport mechanisms at the electrode-electrolyte interface have been studied at nanoscale by neutron imaging. The fundamental aspects of this research have significance in several applications such as desalination of water by capacitive deionization (CDI) and harvesting salinity gradient energy based on the principle of capacitive double layer expansion (CDLE).

Based on the experimental and modeling results presented in the thesis, the following specific conclusions can be stated:

- Temperature of the solution is an important system parameter to be considered especially with regards to desalination of produced water which is released from oil/gas operations, and reaches the surface at higher temperatures. Higher rates of sorption and regeneration are observed in CDI experiments with solutions at higher temperature of around 40°C. At higher temperature, a comparison of the

results from CDI experiments with sodium chloride and Instant Ocean solution revealed competition between ions of various sizes and valence. The cumulative salt mass predicted by the transport model was matched with the experimental data for both sodium chloride and Instant Ocean solution.

- Neutron imaging experiments aid in understanding at nanoscale the ion transport phenomena occurring at the electrode-electrolyte interface during electrosorption. Neutron imaging of gadolinium ions was conducted to obtain information on the direction and magnitude of ion transport during the sorption and regeneration phases of the capacitive deionization process. From the ion concentration profiles, the effective diffusion coefficient of gadolinium ions was estimated at various conditions of applied potential (0 V, 1.2 V, 1.2 V DC+AC). The value of effective diffusion coefficient of gadolinium ions through mesoporous carbon was estimated to be 25 times smaller than the bulk diffusion coefficient. When a DC potential of 1.2 V was applied between the electrodes, the effective diffusivity of gadolinium ions increased by approximately 7 times. The value of effective diffusion coefficient of ions under various values of applied potential can provide valuable insights into the transport properties of ions and aid in synthesis of electrode materials with better sorption properties. The value of effective diffusivity of ions is also required in theoretical modeling of CDI process and thus the results obtained can aid in the validation of transport models of ions in porous carbon materials.
- Neutron imaging experiments with lithium chloride (^{6}LiCl) salt solution were conducted to observe the behavior of the CDI process at high concentrations of

electrolyte. The neutron imaging experiments revealed that during the regeneration phase the electrodes became saturated with salt due to precipitation. This occurred due to the migration of counterions into the electrodes to neutralize the surface charge. Thus, neutron imaging gives an insight into why the CDI process does not work well at high ionic concentrations. It is proposed that placing an ion-exchange membrane next to the carbon electrodes can solve the issue by preventing the migration of counterions and thus avoid the saturation of electrode pores.

- The effective diffusion coefficient of lithium ions was estimated at 0 V and 1.2 V by employing Fick's second law. The effective diffusivity of lithium ions increased by about 6 times when 1.2 V DC potential was applied across the electrodes.
- A high frequency, low amplitude alternating current (AC) signal when superimposed on a direct current (DC) signal results in the enhancement of sorption rates. The CDI experiments showed an increase in the sorption and regeneration rates when AC potential was superimposed on the DC potential. It was found that the amplitude and frequency of the AC signal also had an effect on the sorption and regeneration rates. Furthermore, neutron imaging was employed to observe the effect of application of AC signal with the DC signal. The effective diffusivity of gadolinium ions increased by 35% when an AC potential was superimposed on DC potential than in the case when only a DC potential was applied. Therefore, the desalination efficiency in the electrosorption process can be increased by optimizing the applied potential.

- Blue energy experiments were conducted to assess the feasibility of generating energy based on the principle of capacitive double layer expansion. Neutron imaging experiments were conducted to investigate the ion transport behavior during the various steps of the blue energy cycle. It was deduced that a voltage range of 0.6-0.9 V is optimal for the operation of blue energy cycle. Transmission profiles across the electrodes as a function of time provide valuable information on the direction and magnitude of ion transport during all the steps of the blue energy cycle. Information on ion transport mechanisms at the electrode-electrolyte interface can further aid in the optimization of the blue energy recovery cycle.

In summary, the experimental results obtained from CDI experiments and transport modeling results help in identifying the ion transport mechanisms inside the nanopores of carbon materials. The electrosorption process using nanostructured mesoporous carbon electrodes has been proved to be a promising technique for the removal of ionic species from aqueous solutions and as a potential method for energy storage. The CDI experiments provide an insight into how the operational parameters affect the electrosorption capacitance of the carbon electrodes. At nanoscale, the neutron imaging experiments provide more in depth information on the ion transport phenomena during electrosorption. A combination of these experimental studies can aid in devising strategies for efficient desalination of seawater. Improved desalination systems will enable increased supply of fresh water for industrial and domestic applications. Thus, the present work has implications in efforts towards solving the current scarcity of water resources and the energy demand.

8.2 Recommendations

The results presented in the thesis, provide valuable information on how to improve the electrosorption efficiency in the CDI process. Further work needs to be done to study the effect of various operational parameters on the efficiency of the CDI process. Since a major application of CDI is for desalination of seawater or fracking water, which consists of a mixture of salts, more studies need to be conducted with Instant Ocean solution. It is recommended to conduct more CDI experiments with Instant Ocean solution under various values of applied potential and solution temperature to study the competition between ions of various valence and radii. The results can be validated by neutron imaging experiments conducted under similar operating conditions.

Since neutron imaging experiments provide a valuable tool to study the ion transport mechanisms at a microscopic level, it is suggested that further experiments be conducted to study the competition between ions of various radii and valence. These experiments can provide valuable information on sorption and regeneration characteristics during desalination of seawater. For neutron imaging experiments conducted with lithium ions, solution of Nernst-Planck model should be adopted for estimating the effective diffusivity of lithium ions taking into account the influence of electric potential and concentration gradient. Neutron imaging experiments with boron should be conducted to study the sorption characteristics with boron, since it is an important element found in seawater. Boron is one of the elements that have a high neutron attenuation coefficient; hence imaging experiments with boron can provide a high contrast for visualizing the transport of ions.

Since electrosorption involves the formation of an electrical double layer (EDL) in the nanopores of porous carbon materials, valuable information can be obtained by studying the formation of EDL at nanoscale. Neutron Reflectometry is a powerful tool which provides structural information near the interface, in the direction normal to the surface. It is recommended that neutron reflectometry experiments should be conducted with salts such as ^{6}LiCl at various ionic concentrations and applied potential to study the structure of EDL under various system conditions. Information on the thickness and structure of EDL under different system conditions can provide insight into the electrosorption mechanisms.

Further work needs to be done with blue energy experiments to estimate the energy produced per cycle and varying the experimental conditions to maximize the energy produced. Neutron imaging experiments can complement laboratory scale CDI experiments to visualize the transport of ions and obtain valuable information on the direction and magnitude of ion transport.

A better understanding of EDL formation and the electrosorption mechanisms at nanoscale can lead to improved system designs in desalination technologies, and in energy storage systems. Information on the effective diffusivities of various ions in porous carbon materials under various system conditions can provide insight into the design of better electrode materials for electrosorption applications.

REFERENCES

Aaron, D.S., Borole, A.P., Hussey, D.S., Jacobson, D.L., Yiacoumi, S., Tsouris, C. (2011) Quantifying the water content in the cathode of enzyme fuel cells via neutron imaging. Journal of Power Sources 196, 1769-1775.

Achilli, A., Cath, T.Y., Childress, A.E. (2009) Power generation with pressure retarded osmosis: An experimental and theoretical investigation. Journal of Membrane Science 343, 42-52

Adani, N., Fallone, B.G., (2000) Neutron imaging using medical linacs, Engineering in Medicine and Biology Society, 2000. Proceedings of the 22nd Annual International Conference of the IEEE, pp. 2457-2460 vol.2454.

Anderson, M.A., Cudero, A.L., Palma, J. (2010) Capacitive deionization as an electrochemical means of saving energy and delivering clean water. Comparison to present desalination practices: Will it compete? Electrochimica Acta 55, 3845-3856.

Ayranci, E., Conway, B.E. (2001a) Adsorption and electrosorption at high-area carbon-felt electrodes for waste-water purification: Systems evaluation with inorganic, S-containing anions. Journal of Applied Electrochemistry 31, 257-266.

Ayranci, E., Conway, B.E. (2001b) Removal of phenol, phenoxide and chlorophenols from waste-waters by adsorption and electrosorption at high-area carbon felt electrodes. Journal of Electroanalytical Chemistry 513, 100-110.

Ban, A., Schafer, A., Wendt, H. (1998) Fundamentals of electrosorption on activated carbon for wastewater treatment of industrial effluents. Journal of Applied Electrochemistry 28, 227-236.

Barragán, V.M., Ruíz Bauzá, C., Imaña, J.L. (2002) Effect of an AC perturbation on a desalination electrodialysis process. Desalination 142, 235-244.

Barrett, E.P., Joyner, L.G., Halenda, P.P. (1951) The determination of pore volume and area distributions in porous substances. I. Computations from nitrogen isotherms. J. Am. Chem. Soc. 73, 373-380.

Bellows, R.J., Lin, M.Y., Arif, M., Thompson, A.K., Jacobson, D. (1999) Neutron Imaging Technique for In Situ Measurement of Water Transport Gradients within Nafion in Polymer Electrolyte Fuel Cells. Journal of The Electrochemical Society 146, 1099-1103.

Bevington, P.R. (1969) Data Reduction and Error Analysis for the Physical Sciences. McGraw-Hill Book Company.

Biesheuvel, P., Fu, Y., Bazant, M. (2012) Electrochemistry and capacitive charging of porous electrodes in asymmetric multicomponent electrolytes. Russian Journal of Electrochemistry 48, 580-592.

Biesheuvel, P.M. (2009) Thermodynamic cycle analysis for capacitive deionization. Journal of Colloid and Interface Science 332, 258-264.

Biesheuvel, P.M., Bazant, M.Z. (2010) Nonlinear dynamics of capacitive charging and desalination by porous electrodes. Physical Review E 81, 031502.

Biesheuvel, P.M., van der Wal, A. (2010) Membrane capacitive deionization. Journal of Membrane Science 346, 256-262.

Biesheuvel, P.M., Zhao, R., Porada, S., van der Wal, A. (2011) Theory of membrane capacitive deionization including the effect of the electrode pore space. Journal of Colloid and Interface Science 360, 239-248.

Bilheux, H., Crawford, K., Walker, L., Voisin, S., Kang, M., Harvey, M., Bailey, B., Phillips, M., Bilheux, J.-C., Berry, K., Ankner, J., Warren, J., Nanda, J., Pannala, S., Lance, M., (2013) Neutron imaging at the Oak Ridge National Laboratory: present and future capabilities, 7th International Topical Meeting on Neutron Radiography, Physics Procedia.

Bispo-Fonseca, I., Aggar, J., Sarrazin, C., Simon, P., Fauvarque, J.F. (1999) Possible improvements in making carbon electrodes for organic supercapacitors. Journal of Power Sources 79, 238-241.

Boillat, P., Kramer, D., Seyfang, B.C., Frei, G., Lehmann, E., Scherer, G.G., Wokaun, A., Ichikawa, Y., Tasaki, Y., Shinohara, K. (2008) In situ observation of the water distribution across a PEFC using high resolution neutron radiography. Electrochemistry Communications 10, 546-550.

Boon, N., van Roij, R. (2011) 'Blue energy' from ion adsorption and electrode charging in sea and river water. Molecular Physics 109, 1229-1241.

Brogioli, D. (2009) Extracting Renewable Energy from a Salinity Difference Using a Capacitor. Physical Review Letters 103, 058501.

Brogioli, D., Zhao, R., Biesheuvel, P.M. (2011) A prototype cell for extracting energy from a water salinity difference by means of double layer expansion in nanoporous carbon electrodes. Energy & Environmental Science 4, 772-777.

Brogioli, D., Ziano, R., Rica, R.A., Salerno, D., Kozynchenko, O., Hamelers, H.V.M., Mantegazza, F. (2012) Exploiting the spontaneous potential of the electrodes used in the capacitive mixing technique for the extraction of energy from salinity difference. Energy & Environmental Science 5, 9870-9880.

Brogioli, D., Ziano, R., Rica, R.A., Salerno, D., Mantegazza, F. (2013) Capacitive mixing for the extraction of energy from salinity differences: Survey of experimental results and electrochemical models. Journal of Colloid and Interface Science 407, 457-466.

Carey, E.F., Jr., Anuj, J.K., Janelle, E.B., Amy, C.S., Jessie, Q.X., Brian, P.H., Georgia, D.T., Joseph, Y.L., Alexander, S.C., Mathew, R.K., Calvin, R.H. (2008) Neutron-stimulated emission computed tomography of a multi-element phantom. Physics in Medicine and Biology 53, 2313.

Carey, E.F., Jr., Janelle, E.B., Amy, C.S., Anuj, K., Jessie, X., Brian, H., Georgia, D.T., Joseph, Y.L., Alexander, C., Calvin, H. (2006) Introduction to neutron stimulated emission computed tomography. Physics in Medicine and Biology 51, 3375.

Chen, W., Fan, Z., Gu, L., Bao, X., Wang, C. (2010) Enhanced capacitance of manganese oxide via confinement inside carbon nanotubes. Chemical Communications 46, 3905-3907.

Conway, B. (1999) Electrochemical supercapacitors: scientific fundamentals and technological applications (POD). Kluwer Academic/plenum. New York.

Conway, B.E., Birss, V., Wojtowicz, J. (1997) The role and utilization of pseudocapacitance for energy storage by supercapacitors. Journal of Power Sources 66, 1-14.

Crank, J. (1979) The Mathematics of Diffusion. Clarendon Press.

Deschler-Erb, E., Lehmann, E.H., Pernet, L., Vontobel, P., Hartmann, S. (2004) The complementary use of neutrons and X-Rays for the non-destructive investigation of archaeological objects from Swiss collections. Archaeometry 46, 647-661.

Długołęcki, P., Gambier, A., Nijmeijer, K., Wessling, M. (2009) Practical Potential of Reverse Electrodialysis As Process for Sustainable Energy Generation. Environmental Science & Technology 43, 6888-6894.

Długołęcki, P., Nymeijer, K., Metz, S., Wessling, M. (2008) Current status of ion exchange membranes for power generation from salinity gradients. Journal of Membrane Science 319, 214-222.

Farmer, J.C., Bahowick, S.M., Harrar, J.E., Fix, D.V., Martinelli, R.E., Vu, A.K., Carroll, K.L. (1997) Electrosorption of Chromium Ions on Carbon Aerogel Electrodes as a Means of Remediating Ground Water. Energy & Fuels 11, 337-347.

Farmer, J.C., Fix, D.V., Mack, G.V., Pekala, R.W., Poco, J.F. (1996) Capacitive Deionization of NaCl and $NaNO_3$ Solutions with Carbon Aerogel Electrodes. Journal of The Electrochemical Society 143, 159-169.

Feng, G., Qiao, R., Huang, J., Dai, S., Sumpter, B.G., Meunier, V. (2011) The importance of ion size and electrode curvature on electrical double layers in ionic liquids. Physical Chemistry Chemical Physics 13, 1152-1161.

Frackowiak, E., Béguin, F. (2001) Carbon materials for the electrochemical storage of energy in capacitors. Carbon 39, 937-950.

Gabelich, C.J., Tran, T.D., Suffet, I.H.M. (2002) Electrosorption of Inorganic Salts from Aqueous Solution Using Carbon Aerogels. Environmental Science & Technology 36, 3010-3019.

Gao, Y., Pan, L., Li, H., Zhang, Y., Zhang, Z., Chen, Y., Sun, Z. (2009) Electrosorption behavior of cations with carbon nanotubes and carbon nanofibres composite film electrodes. Thin Solid Films 517, 1616-1619.

Gao, Y., Pan, L., Zhang, Y., Chen, Y., Sun, Z. (2007) Electrosorption of FeCl3 solutions with carbon nanotubes and nanofibers film electrodes grown on graphite substrates. Surface Review and Letters 14, 1033-1037.

Goers, D., Holzapfel, M., Scheifele, W., Lehmann, E., Vontobel, P., Novák, P. (2004) In situ neutron radiography of lithium-ion batteries: the gas evolution on graphite electrodes during the charging. Journal of Power Sources 130, 221-226.

Golovnev, A., Trimper, S. (2009) Exact solution of the Poisson--Nernst--Planck equations in the linear regime. Journal of Chemical Physics 131, 114903-114906.

Hou, C.-H., Liang, C., Yiacoumi, S., Dai, S., Tsouris, C. (2006) Electrosorption capacitance of nanostructured carbon-based materials. Journal of Colloid and Interface Science 302, 54-61.

Hrubesh, L.W. (1998) Aerogel applications. Journal of Non-Crystalline Solids 225, 335-342.

Huang, J., Sumpter, B.G., Meunier, V. (2008a) Theoretical Model for Nanoporous Carbon Supercapacitors. Angewandte Chemie International Edition 47, 520-524.

Huang, J., Sumpter, B.G., Meunier, V. (2008b) A Universal Model for Nanoporous Carbon Supercapacitors Applicable to Diverse Pore Regimes, Carbon Materials, and Electrolytes. Chemistry – A European Journal 14, 6614-6626.

Jacobson, L., de Beer, F.C., Nshimirimana, R. (2011) Tomography imaging of South African archaeological and heritage stone and pottery objects. Nuclear Instruments and Methods in Physical Research Section A 651, 240-243.

Johnson, A.M., Newman, J. (1971) Journal of The Electrochemical Society 118, 510-517.

Johnson, A.M., Venolia, A.W., Wilbourne, R.G., Newman, J., (1970) The Electrosorb Process for Desalting Water.

Jung, H.-H., Hwang, S.-W., Hyun, S.-H., Lee, K.-H., Kim, G.-T. (2007) Capacitive deionization characteristics of nanostructured carbon aerogel electrodes synthesized via ambient drying. Desalination 216, 377-385.

Kamali Moghaddam, K., Taheri, T., Ayubian, M. (2008) Bone structure investigation using X-ray and neutron radiography techniques. Applied Radiation and Isotopes 66, 39-43.

Kamata, M., Esaka, T., Fujine, S., Yoneda, K., Kanda, K. (1997) Lithium batteries: Application of neutron radiography. Journal of Power Sources 68, 459-462.

Kapadia, A.J., Tourassi, G.D., Sharma, A.C., Crowell, A.S., Kiser, M.R., Howell, C.R. (2008) Experimental detection of iron overload in liver through neutron stimulated emission spectroscopy. Physics in Medicine and Biology 53, 2633.

Kinoshita, K. (1988) Carbon: electrochemical and physicochemical properties. John Wiley & Sons Inc, New York.

Kruk, M., Jaroniec, M. (2001) Gas adsorption characterization of ordered organic-inorganic nanocomposite materials. Chemistry of Materials 13, 3169-3183.

La Mantia, F., Pasta, M., Deshazer, H.D., Logan, B.E., Cui, Y. (2011) Batteries for Efficient Energy Extraction from a Water Salinity Difference. Nano Letters 11, 1810-1813.

Lanz, M., Lehmann, E., Imhof, R., Exnar, I., Novák, P. (2001) In situ neutron radiography of lithium-ion batteries during charge/discharge cycling. Journal of Power Sources 101, 177-181.

Latrous, H., Oliver, J. (1992) Self-diffusion coefficients and structure of the trivalent transplutonium ion curium and gadolinium in aqueous solution. Journal of Radioanalytical and Nuclear Chemistry 156, 291-296.

Lee, J.-B., Park, K.-K., Eum, H.-M., Lee, C.-W. (2006) Desalination of a thermal power plant wastewater by membrane capacitive deionization. Desalination 196, 125-134.

Levenspiel, O., Godfrey, J.H. (1974) A gradientless contactor for experimental study of interphase mass transfer with/without reaction. Chemical Engineering Science 29, 1723-1730.

Li, H., Pan, L., Lu, T., Zhan, Y., Nie, C., Sun, Z. (2011) A comparative study on electrosorptive behavior of carbon nanotubes and graphene for capacitive deionization. Journal of Electroanalytical Chemistry 653, 40-44.

Li, H., Zou, L., Pan, L., Sun, Z. (2010a) Novel Graphene-Like Electrodes for Capacitive Deionization. Environmental Science & Technology 44, 8692-8697.

Li, H., Zou, L., Pan, L., Sun, Z. (2010b) Using graphene nano-flakes as electrodes to remove ferric ions by capacitive deionization. Separation and Purification Technology 75, 8-14.

Li, L., Zou, L., Song, H., Morris, G. (2009) Ordered mesoporous carbons synthesized by a modified sol-gel process for electrosorptive removal of sodium chloride. Carbon 47, 775-781.

Liang, C., Dai, S. (2006) Synthesis of Mesoporous Carbon Materials via Enhanced Hydrogen-Bonding Interaction. Journal of the American Chemical Society 128, 5316-5317.

Liang, C., Li, Z., Dai, S. (2008) Mesoporous Carbon Materials: Synthesis and Modification. Angewandte Chemie International Edition 47, 3696-3717.

Lin, C., Ritter, J.A., Popov, B.N. (1999) Correlation of Double-Layer Capacitance with the Pore Structure of Sol-Gel Derived Carbon Xerogels. Journal of The Electrochemical Society 146, 3639-3643.

Liu, F., Schaetzle, O., Sales, B.B., Saakes, M., Buisman, C.J.N., Hamelers, H.V.M. (2012) Effect of additional charging and current density on the performance of Capacitive energy extraction based on Donnan Potential. Energy & Environmental Science 5, 8642-8650.

Loeb, S. (1976) Production of energy from concentrated brines by pressure-retarded osmosis : I. Preliminary technical and economic correlations. Journal of Membrane Science 1, 49-63.

Loeb, S., Van Hessen, F., Shahaf, D. (1976) Production of energy from concentrated brines by pressure-retarded osmosis : II. Experimental results and projected energy costs. Journal of Membrane Science 1, 249-269.

Matlab Users Guide, The Math Works, Inc., Natick, MA (1998).

Mayes, R.T., Tsouris, C., Kiggans Jr, J.O., Mahurin, S.M., DePaoli, D.W., Dai, S. (2010) Hierarchical ordered mesoporous carbon from phloroglucinol-glyoxal and its application

in capacitive deionization of brackish water. Journal of Materials Chemistry 20, 8674-8678.

Menon, M., Robinson, B., Oswald, S.E., Kaestner, A., Abbaspour, K.C., Lehmann, E., Schulin, R. (2007) Visualization of root growth in heterogeneously contaminated soil using neutron radiography. European Journal of Soil Science 58, 802-810.

Miller, J.M., Dunn, B. (1999) Morphology and Electrochemistry of Ruthenium/Carbon Aerogel Nanostructures. Langmuir 15, 799-806.

Morita, M., Nishimura, N., Matsuda, Y. (1993) Charge/discharge cycling behavior of pitch-based carbon fiber in organic electrolyte solutions. Electrochimica Acta 38, 1721-1726.

Mukundan, R., Borup, R.L. (2009) Visualising Liquid Water in PEM Fuel Cells Using Neutron Imaging. Fuel Cells 9, 499-505.

Nanda, J., Bilheux, H., Voisin, S., Veith, G.M., Archibald, R., Walker, L., Allu, S., Dudney, N.J., Pannala, S. (2012) Anomalous Discharge Product Distribution in Lithium-Air Cathodes. The Journal of Physical Chemistry C 116, 8401-8408.

Newman, J., Thomas-Alyea, K.E. (2004a) Electrochemical Systems, 3rd ed. ed. Wiley, New York.

Newman, J., Tiedemann, W. (1975) Porous-electrode theory with battery applications. AIChE Journal 21, 25-41.

Newman, J.S., Thomas-Alyea, K.E. (2004b) Electrochemical systems. Wiley-Interscience, Hoboken, N.J.

Norman, R.S. (1974) Water salination: a source of energy. Science (New York, N.Y.) 186, 350-352.

Oh, H.-J., Lee, J.-H., Ahn, H.-J., Jeong, Y., Kim, Y.-J., Chi, C.-S. (2006) Nanoporous activated carbon cloth for capacitive deionization of aqueous solution. Thin Solid Films 515, 220-225.

Oren, Y. (2008) Capacitive deionization (CDI) for desalination and water treatment — past, present and future (a review). Desalination 228, 10-29.

Oswald, S.E., Menon, M., Carminati, A., Vontobel, P., Lehmann, E., Schulin, R. (2008) Quantitative Imaging of Infiltration, Root Growth, and Root Water Uptake via Neutron Radiography. Vadose Zone J. 7, 1035-1047.

Otowa, T., (1996) Planar, flow-through, electric, double-layer capacitor and a method of treating liquids with the capacitor, in: USPTO (Ed.). Marc D. Andelman, United States.

Pan, L., Wang, X., Gao, Y., Zhang, Y., Chen, Y., Sun, Z. (2009) Electrosorption of anions with carbon nanotube and nanofibre composite film electrodes. Desalination 244, 139-143.

Park, B.-H., Choi, J.-H. (2010) Improvement in the capacitance of a carbon electrode prepared using water-soluble polymer binder for a capacitive deionization application. Electrochimica Acta 55, 2888-2893.

Park, J., Li, X., Tran, D., Abdel-Baset, T., Hussey, D.S., Jacobson, D.L., Arif, M. (2008) Neutron imaging investigation of liquid water distribution in and the performance of a PEM fuel cell. International Journal of Hydrogen Energy 33, 3373-3384.

Pattle, R.E. (1954) Production of Electric Power by mixing Fresh and Salt Water in the Hydroelectric Pile. Nature 174, 660-660.

Pekala, R.W., Farmer, J.C., Alviso, C.T., Tran, T.D., Mayer, S.T., Miller, J.M., Dunn, B. (1998) Carbon aerogels for electrochemical applications. Journal of Non-Crystalline Solids 225, 74-80.

Pekula, N., Heller, K., Chuang, P.A., Turhan, A., Mench, M.M., Brenizer, J.S., Ünlü, K. (2005) Study of water distribution and transport in a polymer electrolyte fuel cell using neutron imaging. Nuclear Instruments and Methods in Physical Research Section A 542, 134-141.

Porada, S., Weinstein, L., Dash, R., van der Wal, A., Bryjak, M., Gogotsi, Y., Biesheuvel, P.M. (2012) Water Desalination Using Capacitive Deionization with Microporous Carbon Electrodes. ACS Applied Materials & Interfaces 4, 1194-1199.

Porada, S., Zhao, R., van der Wal, A., Presser, V., Biesheuvel, P.M. (2013) Review on the science and technology of water desalination by capacitive deionization. Progress in Materials Science 58, 1388-1442.

Post, J.W., Hamelers, H.V.M., Buisman, C.J.N. (2008) Energy Recovery from Controlled Mixing Salt and Fresh Water with a Reverse Electrodialysis System. Environmental Science & Technology 42, 5785-5790.

Rafik, B., Noureddine, O., Abderabbou, A., Habib, L. (2010) Self-diffusion coefficients of the trivalent f-element ion series in dilute and moderately dilute aqueous solutions: A comparative study between europium, gadolinium, terbium and berkelium. IOP Conference Series: Materials Science and Engineering 9, 012079.

Rasband, W.S., ImageJ, U. S. National Institutes of Health, Bethesda, M., USA, http://imagej.nih.gov/ij/ (1997-2011).

Ray, J.P., Engelhardt, F.R. (1993) Produced Water: Technological/Environmental Issues and Solutions, 1 ed. Springer.

Ryan, D., Carbonell, R.G., Whitaker, S. (1981) A theory of diffusion and reaction in porous media. Aiche symposium series 77, 46-62.

Ryoo, M.-W., Kim, J.-H., Seo, G. (2003) Role of titania incorporated on activated carbon cloth for capacitive deionization of NaCl solution. Journal of Colloid and Interface Science 264, 414-419.

Sales, B.B., Burheim, O.S., Liu, F., Schaetzle, O., Buisman, C.J.N., Hamelers, H.V.M. (2012a) Impact of Wire Geometry in Energy Extraction from Salinity Differences Using Capacitive Technology. Environmental Science & Technology 46, 12203-12208.

Sales, B.B., Liu, F., Schaetzle, O., Buisman, C.J.N., Hamelers, H.V.M. (2012b) Electrochemical characterization of a supercapacitor flow cell for power production from salinity gradients. Electrochimica Acta 86, 298-304.

Sales, B.B., Saakes, M., Post, J.W., Buisman, C.J.N., Biesheuvel, P.M., Hamelers, H.V.M. (2010) Direct Power Production from a Water Salinity Difference in a Membrane-Modified Supercapacitor Flow Cell. Environmental Science & Technology 44, 5661-5665.

Satija, R., Jacobson, D.L., Arif, M., Werner, S.A. (2004) In situ neutron imaging technique for evaluation of water management systems in operating PEM fuel cells. Journal of Power Sources 129, 238-245.

Sears, V.F. (1992) Neutron scattering lengths and cross sections. Neutron News 3, 26-37.

Shannon, M.A., Bohn, P.W., Elimelech, M., Georgiadis, J.G., Marinas, B.J., Mayes, A.M. (2008) Science and technology for water purification in the coming decades. Nature 452, 301-310.

Sharma, A.C., Harrawood, B.P., Bender, J.E., Tourassi, G.D., Kapadia, A.J. (2007) Neutron stimulated emission computed tomography: a Monte Carlo simulation approach. Physics in Medicine and Biology 52, 6117.

Sharma, K., Bilheux, H.Z., Walker, L.M.H., Voisin, S., Mayes, R.T., Kiggans Jr, J.O., Yiacoumi, S., DePaoli, D.W., Dai, S., Tsouris, C. (2013a) Neutron imaging of ion transport in mesoporous carbon materials. Physical Chemistry Chemical Physics 15, 11740-11747.

Sharma, K., Mayes, R.T., Kiggans Jr, J.O., Yiacoumi, S., Gabitto, J., DePaoli, D.W., Dai, S., Tsouris, C. (2013b) Influence of temperature on the electrosorption of ions from aqueous solutions using mesoporous carbon materials. Separation and Purification Technology 116, 206-213.

Siegel, J.B., Lin, X., Stefanopoulou, A.G., Hussey, D.S., Jacobson, D.L., Gorsich, D. (2011a) Neutron Imaging of Lithium Concentration in LFP Pouch Cell Battery. Journal of The Electrochemical Society 158, A523-A529.

Siegel, J.B., Xinfan, L., Stefanopoulou, A.G., Gorsich, D., (2011b) Neutron imaging of lithium concentration in battery pouch cells, American Control Conference (ACC), Pages 376-381, pp. 376-381.

Simon, P., Gogotsi, Y. (2008) Materials for electrochemical capacitors. Nature Materials 7, 845 - 854.

Takami, N., Satoh, A., Hara, M., Ohsaki, T. (1995) Structural and Kinetic Characterization of Lithium Intercalation into Carbon Anodes for Secondary Lithium Batteries. Journal of The Electrochemical Society 142, 371-379.

Tang, H.-Y., Santamaria, A., Kurniawan, J., Park, J.W., Yang, T.-H., Sohn, Y.-J. (2010) Developing a 3D neutron tomography method for proton exchange membrane fuel cells. Journal of Power Sources 195, 6774-6781.

Thorsen, T., Holt, T. (2009) The potential for power production from salinity gradients by pressure retarded osmosis. Journal of Membrane Science 335, 103-110.

Tsouris, C., Mayes, R., Kiggans, J., Sharma, K., Yiacoumi, S., DePaoli, D., Dai, S. (2011) Mesoporous Carbon for Capacitive Deionization of Saline Water. Environmental Science and Technology 45, 10243-10249.

Turhan, A., Heller, K., Brenizer, J.S., Mench, M.M. (2006) Quantification of liquid water accumulation and distribution in a polymer electrolyte fuel cell using neutron imaging. Journal of Power Sources 160, 1195-1203.

Van Langh, R., Lehmann, E., Hartmann, S., Kaestner, A., Scholten, F. (2009) The study of bronze statuettes with the help of neutron-imaging techniques. Analytical and Bioanalytical Chemistry 395, 1949-1959.

Veerman, J., Saakes, M., Metz, S.J., Harmsen, G.J. (2009) Reverse electrodialysis: Performance of a stack with 50 cells on the mixing of sea and river water. Journal of Membrane Science 327, 136-144.

Wang, J., Angnes, L., Tobias, H., Roesner, R.A., Hong, K.C., Glass, R.S., Kong, F.M., Pekala, R.W. (1993) Carbon aerogel composite electrodes. Anal. Chem. 65.

Wang, M., Huang, Z.-H., Wang, L., Wang, M.-X., Kang, F., Hou, H. (2010a) Electrospun ultrafine carbon fiber webs for electrochemical capacitive desalination. New Journal of Chemistry 34, 1843-1845.

Wang, X.Q., Lee, J.S., Tsouris, C., DePaoli, D.W., Dai, S. (2010b) Preparation of activated mesoporous carbons for electrosorption of ions from aqueous solutions. Journal of Materials Chemistry 20, 4602-4608.

Wang, X.Q., Liang, C.D., Dai, S. (2008) Facile synthesis of ordered mesoporous carbons with high thermal stability by self-assembly of resorcinol-formaldehyde and block copolymers under highly acidic conditions. Langmuir 24, 7500-7505.

Wang, X.Z., Li, M.G., Chen, Y.W., Cheng, R.M., Huang, S.M., Pan, L.K., Sun, Z. (2006) Electrosorption of NaCl Solutions with Carbon Nanotubes and Nanofibers Composite Film Electrodes. Electrochemical and Solid-State Letters 9, E23-E26.

Weinstein, J.N., Leitz, F.B. (1976) Electric Power from Differences in Salinity: The Dialytic Battery. Science 191, 557-559.

Wick, G.L. (1978) Power from salinity gradients. Energy 3, 95-100.

Wick, G.L., Schmitt, W.R. (1977) Prospects for renewable energy from the sea. Marine Technology Society Journal 11.

Xu, P., Drewes, J.E., Heil, D., Wang, G. (2008) Treatment of brackish produced water using carbon aerogel-based capacitive deionization technology. Water Research 42, 2605-2617.

Yang, K.-L., Yiacoumi, S., Tsouris, C. (2003) Electrosorption capacitance of nanostructured carbon aerogel obtained by cyclic voltammetry. Journal of Electroanalytical Chemistry 540, 159-167.

Yang, K.-L., Ying, T.-Y., Yiacoumi, S., Tsouris, C., Vittoratos, E.S. (2001) Electrosorption of Ions from Aqueous Solutions by Carbon Aerogel: An Electrical Double-Layer Model. Langmuir 17, 1961-1969.

Ying, T.-Y., Yang, K.-L., Yiacoumi, S., Tsouris, C. (2002) Electrosorption of Ions from Aqueous Solutions by Nanostructured Carbon Aerogel. Journal of Colloid and Interface Science 250, 18-27.

Yoon, S., Lee, J., Hyeon, T., Oh, S.M. (2000) Electric Double-Layer Capacitor Performance of a New Mesoporous Carbon. Journal of The Electrochemical Society 147, 2507-2512.

Yu, P., Popov, B.N., Ritter, J.A., White, R.E. (1999) Determination of the Lithium Ion Diffusion Coefficient in Graphite. Journal of The Electrochemical Society 146, 8-14.

Zhang, D., Shi, L., Fang, J., Dai, K. (2007) Influence of diameter of carbon nanotubes mounted in flow-through capacitors on removal of NaCl from salt water. Journal of Materials Science 42, 2471-2475.

Zhang, S.Q., Wang, J., Shen, J., Deng, Z.S., Lai, Z.Q., Zhou, B., Attia, S.M., Chen, L.Y. (1999) The investigation of the adsorption character of carbon aerogels. Nonstruct. Mater. 11, 375.

Zou, L., Li, L., Song, H., Morris, G. (2008a) Using mesoporous carbon electrodes for brackish water desalination. Water Research 42, 2340-2348.

Zou, L., Morris, G., Qi, D. (2008b) Using activated carbon electrode in electrosorptive deionisation of brackish water. Desalination 225, 329-340.